Switching and Generation of Ultrashort Pulses Using All-Fibre Devices

David Allister Pattison

Doctor of Philosophy

The University of Aston in Birmingham

December 1995

THE UNIVERSITY OF ASTON IN BIRMINGHAM

Switching and Generation of Ultrashort Pulses Using All-Fibre Devices

David Allister Pattison

Doctor of Philosophy

1995

Abstract

Serial and parallel interconnection of photonic devices is integral to the construction of any all-optical data processing system. This thesis presents results from a series of experiments centering on the use of the nonlinear-optical loop mirror (NOLM) switch in architectures for the manipulation and generation of ultrashort pulses.

Detailed analysis of soliton switching in a single NOLM and cascade of two NOLM's is performed, centering on primary limitations to device operation, effect of cascading on amplitude response, and impact of switching on the characteristics of incident pulses. By using relatively long input pulses, device failure due to stimulated Raman generation is postponed to demonstrate multiple-peaked switching for the first time. It is found that while cascading leads to a sharpening of the overall switching characteristic, pulse spectral and temporal integrity is not significantly degraded, and emerging pulses retain their essential soliton character. In addition, by including an asymmetrically placed in-fibre Bragg reflector as a wavelength selective loss element in the basic NOLM configuration, both soliton self-switching and dual-wavelength control-pulse switching are spectrally quantised.

Results are presented from a novel dual-wavelength laser configuration generating pulse trains with an ultra-low rms inter-pulse-stream timing jitter level of 630fs enabling application in ultrafast switching environments at data rates as high as 130GBits/s. In addition, the fibre NOLM is included in architectures for all-optical memory, demonstrating storage and logical inversion of a 0.5kByte random data sequence; and ultrafast phase-locking of a gain-switched distributed feedback laser at 1.062GHz, the fourteenth harmonic of the system baseband frequency. The stringent requirements for environmental robustness of these architectures highlight the primary weaknesses of the NOLM in its fibre form and recommendations to overcome its inherent drawbacks are presented.

Key Words – Nonlinear Fibre Optics, Nonlinear Fibre Switching.

Acknowledgments

I wish, firstly, to thank my supervisor, Professor Ian Bennion, for his continuous encouragement, support, open door and invaluable advice on how to write and speak. He was always there for a chat and seemed to know exactly what to say.

Insufficient thanks go to Dr. Peter Kean, my main source of information, ideas, and experimental advice, who taught me by example and word how to approach things properly. This is also true of Dr. Wladek Forysiak: without his help in the form of a transparently-named file system and ready-made code, the number of numerical results present herein would be somewhat lower. Thanks must go, also, to Kate Sugden and Lin Zhang for helpful and efficient grating supply.

For the moral support, encouragement and help which he has given me for all of the four years which he has known me, I thank Professor Mike Cardwell, who seemed to believe in me more than I did.

I wish to thank, especially, Bert Biggs for many and varied excellent chats about topics too diverse to summarise, but also everybody: Kate, Finlay, etc. etc. It seems to me that Photonics at Aston is a good place to be.

Finally, I wish to thank the Department of Education Northern Ireland for personal funding throughout the three years and the UK Engineering and Physical Sciences Research Group for financial support.

Contents

List of Figures

"...anticlericalism and American bustle would soon free them from belief in miracles and holy likenesses. But where, I ask myself, will mercy and divine compassion come from then? Or are such things necessary to people who are well fed and know the wonders that lie concealed in an atom? I don't regret economic and educational advancement; I just wonder how much we shall have to pay for it, and in what coin."

from *"Fifth Business"*,
by Robertson Davies.

Chapter 1

Introduction

The current rise in demand for untethered personal communications and comprehensive telecommunications products which can provide not only "traditional" services such as telephony and FAX, but broadband multi-media services as well, necessitates the development of networks capable of carrying and processing data at rates of tens or hundreds of gigabits per second. Meeting the diverse requirements of these disparate services requires the unification of a set of widely differing network concepts into a single transport and switching methodology such as the Broadband Integrated Services Digital Network (B-ISDN) concept, which is based on the, now universally accepted, Synchronous Digital Hierarchy (SDH) and Asynchronous Transfer Mode (ATM) standards [1]. Such developments are primary drivers in the further exploitation of the high capacity of optical fibre networks through photonic processing technologies [2].

It has become apparent that the complex processing of electrical signals required by SDH optical networks will become prohibitively difficult above 10GBit/s [3] due to the accompanying increases in complexity of software, and switching and signal processing systems. By designing the network to optimally combine the advantages of existing technologies with the potential of photonic processing, greater throughput may be achieved. In such a network, a photonic switching layer above the electronic network will perform simple ultrafast routing, switching and processing functions on time-division- [4, 5] and wavelength-division-multiplexed [6] SDH channels, leaving more complex, but less latency-sensitive processing, to the electronic network below.

It is not enough, however, merely to address the impact of increased traffic on switching technology. As optical-time-division-multiplexing (OTDM) hierarchies grow to interleave ever-increasing numbers of data streams, consequences also ensue from accompanying reductions in the temporal width of each data bit, pushing data, necessarily, into the picosecond regime.

As a picosecond regime data bit, which inherently balances the effects of fibre chromatic dispersion and nonlinearity, effects detrimental to non-return-to-zero (NRZ) systems [7, 8], the soliton has two important advantages. Firstly, it is resistant to temporal broadening, being stable over long propagation spans, a property which lies at the root of the current high level of interest in soliton systems for future long- [9, 10, 11, 12] and medium-haul [13, 14, 15] transmission. Secondly, the phase of a soliton is constant across its temporal envelope [16], a property which may be used to ensure minimal temporal distortion in photonic switching devices [17, 18].

Within this context, *i.e.* that of photonic processing of ultrashort pulses, the purpose of this thesis is to present experimental results from a series of studies of nonlinear switching using optical fibre. As all-optical processing elements, fibre devices have the advantages of simplicity of construction, a near-instantaneous nonlinear response on the order of only a few optical cycles, and inherently low loss, allowing long interaction lengths which compensate for the relatively weak nonlinear coefficient of fibre. In addition, as an environment in which soliton formation may be achieved with comparative ease through the use of picosecond mode-locked sources, fibre also provides an ideal medium for evaluating the merits of this type of carrier in all-optical processing.

A fundamental aspect of any high level data processing system is the principle of concatenation through which sets of primitive components are combined to perform functions of higher complexity. Since the same is true of photonic architectures, it is also vital to ascertain the cascadability of any device which is posited as a candidate for all-optical processing. One such device is the nonlinear-optical loop mirror (NOLM) [19], a fibre-based device which has been used in experimental demonstrations across a wide spectrum of applications such as all-optical demultiplexing [20], clock recovery [21], phase detection [22], and wavelength and pulse width conversion [23]. This thesis presents an experimental study, the principal aim of which is, to establish the suitability of the NOLM for integration both with itself and with other devices in photonic processing architectures. Indissolubly linked with this aim, is the necessity of evaluating the effect of the device on the data it manipulates. Thus, the foundation experiments analyse not only the amplitude response of the device but also its effects on the spectral and temporal integrity of soliton data passing through it. As the simplest implementation of

the NOLM, and one in which soliton formation is inevitable under the correct conditions, the all-fibre NOLM is a device well suited to such a study.

Before entering into a detailed experimental discussion, succeeding sections in this chapter introduce some basic fibre characteristics and fundamental concepts which underpin the process of nonlinear switching and soliton formation in optical fibre. A comparative study of a representative selection of the most important all-fibre devices demonstrated to date is then presented, identifying a number of key weaknesses which present obstacles to future use.

1.1 Linear and Nonlinear Fibre Characteristics

1.1.1 Fibre Loss

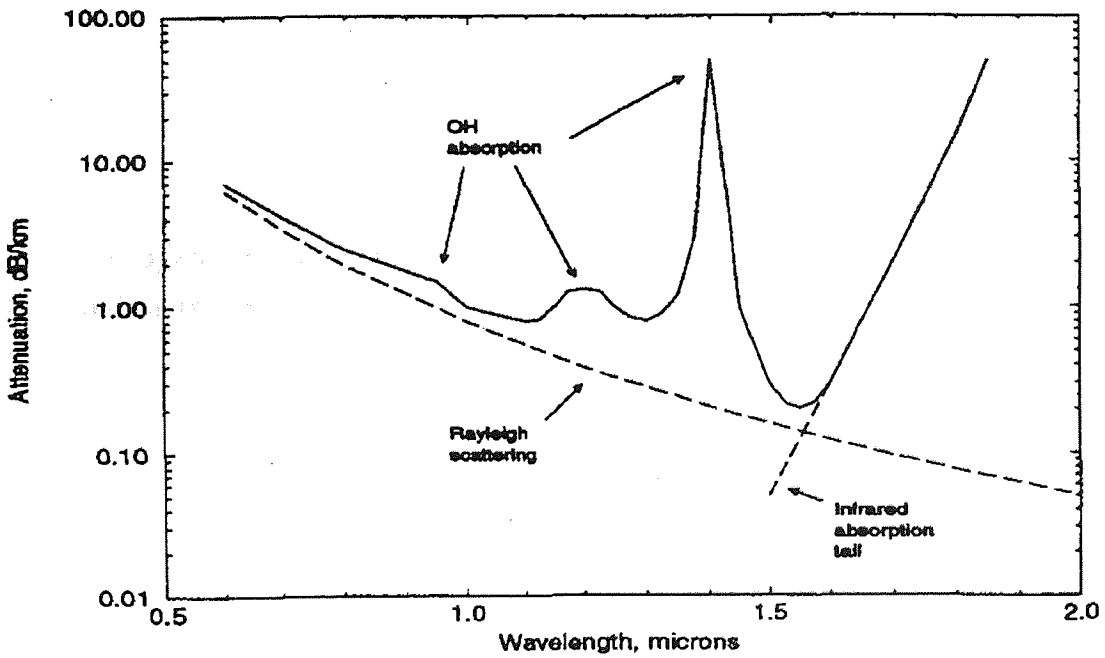

Figure 1.1: Typical loss profile for silica optical fibre as a function of wavelength.

Inherently low loss is an attribute of optical fibre which makes it an extremely attractive medium for both data transmission and nonlinear switching systems, facilitating transmission over extremely long distances without repeaters on the one hand and compensating for the relatively low nonlinearity of fibre on the other by allowing long nonlinear interaction lengths.

Figure 1.1 shows a summary of the major loss contributions for silica fibre plotted as a function of incident wavelength. Fibre loss arises from a combination of both extrinsic and intrinsic absorption mechanisms coupled with Rayleigh scattering. The major extrinsic absorption is due to the presence of impurity hydroxyl ions (OH^-) in the glass and is the cause of the prominent peaks at 1400nm, 950nm and 725nm, the first, second and third harmonics of the fundamental OH^- absorption peak at 2.7μm . Intrinsic absorption in the constituents of the glass, which exists even in an impurity- and defect-free material, is dominated by the transfer of optical energy to silica-germania bonds and gives rise to the strong absorption edge beyond 1.6μm .

The final major source of loss is from Rayleigh scattering due to localised refractive index variations on a length scale which is smaller than the wavelength of the incident optical signal. These arise from compositional and structural inhomogeneities in the material due to the amorphous nature of the glass and lead to wavelength-dependent scattering out of the material. Below 1μm Rayleigh scattering is the dominant loss mechanism in fibre, however, the λ^{-4} dependence causes its influence to weaken dramatically with increasing wavelength. Thus, overall fibre loss falls significantly with increasing wavelength to a minimum value of ~0.19dB/km around 1550nm, a region known as the third transmission window, and increases strongly beyond 1.6μm as infrared absorption becomes more important. The extremely low loss in this third window is the principal reason for the thrust to develop transmission systems at 1550nm [24] and is the region chosen for the experimental investigations detailed in this thesis.

1.1.2 Chromatic Dispersion in Fibre

Chromatic dispersion is a result of the frequency-dependent response of bound electrons in a dielectric to a propagating optical wave, an effect which manifests itself, in turn, as a frequency-dependent refractive index. The effect of chromatic dispersion on an optical wave in such a medium may be evaluated using a Taylor expansion of the propagation constant,

$$\beta = \frac{2\pi}{\lambda} n(\omega) \tag{1.1}$$

giving,

$$\beta = \beta_0 + \beta_1(\omega) + \frac{1}{2}\beta_2(\omega - \omega_0)^2 + \frac{1}{6}\beta_3(\omega - \omega_0)^3 + \ldots \tag{1.2}$$

where,

$$\beta_m = \frac{d^m\beta}{d\omega^m} \quad \text{, for m = 0,1,2,...} \tag{1.3}$$

The group velocity, given by $v_g = d\omega/d\beta$, is then

$$v_g = \frac{1}{\beta_1} \tag{1.4}$$

and the group velocity dispersion (GVD) parameter, β_2, is given by,

$$\beta_2 = \frac{d}{d\omega}\frac{1}{v_g} = -\frac{1}{v_g^2}\frac{dv_g}{d\omega}.\text{ps}^2/\text{km}. \tag{1.5}$$

GVD is more commonly expressed in terms of a wavelength derivative to give a group delay per nanometer per unit length, or group delay dispersion (GDD),

$$D = \beta_2\frac{d\omega}{d\lambda} = -\frac{2\pi c\beta_2}{\lambda^2}.\text{ps}/(\text{nm.km}) \tag{1.6}$$

where c is the speed of light in vacuum.

Thus, transmission delay is seen to be wavelength-dependent, giving rise to temporal broadening and the formation of a frequency chirp due to a redistribution of the spectral content of a finite-bandwidth optical pulse. Figure 1.2 shows a plot of the variation of group delay dispersion, D, with wavelength for a typical, standard single-mode fibre.

The crucial aspect of this dispersion profile is its zero-crossing, pointing to the existence of two distinct dispersion regimes, each with its own implications for an initially unchirped pulse. For wavelengths in the normal dispersion regime, *i.e.* below the zero-dispersion wavelength, λ_0, in this case at 1312nm, shorter wavelengths travel more slowly than longer wavelength components causing the pulse to become up-chirped, *i.e.* blue-shifted towards the trailing edge. In the anomalous dispersion regime, *i.e.* for wavelengths above 1312nm, propagation leads to the emergence of a down-chirp with longer wavelengths towards the trailing edge.

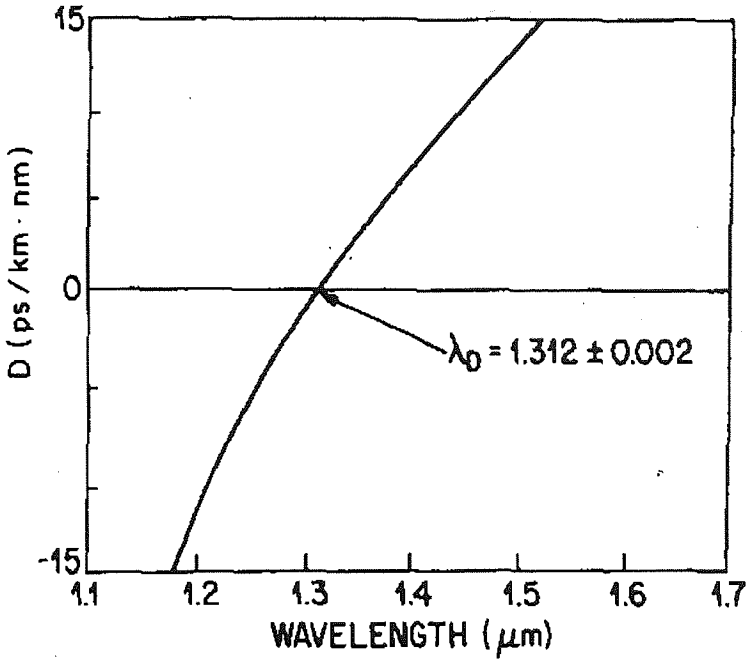

Figure 1.2: Variation of group delay dispersion, D(ps/nm.km), with wavelength for a typical standard, single-mode fibre.

In practice, the position of λ_0 is determined by the precise physical parameters of a fibre since the total group-delay dispersion is the sum of contributions from waveguide dispersion, which is a function of the core refractive index profile, and chromatic dispersion. By appropriate fibre design, therefore, the value of λ_0 can be tailored, enabling the fabrication of dispersion-shifted fibres [25] with zero-dispersion wavelengths within the minimum loss window at 1550nm. Such fibres are important tools in the control-pulse-switched version of the NOLM, a configuration which is discussed in section 5.2 of chapter 5. Results from dispersion characterisations of the fibres used in subsequent experimental studies are presented in section 2.4.1 of chapter 2.

1.1.3 Fibre Nonlinearity

When propagating through a medium, an optical field induces a polarisation on the atomic level due to distortion of bound-electron charge clouds. For small applied fields, the induced polarisation, P, is linear with intensity and is given by $P=\epsilon_0\chi_1 E$ where E is the magnitude of the field, χ_1 is the linear susceptibility of

the material and ϵ_0 is the permittivity of free space. With increasing intensity, however, the presence of anharmonic resonance terms becomes important and the medium response may no longer be considered to be linear, *i.e.* obedient to the principle of superposition. Under these circumstances, a more general expression for induced polarisation which includes anharmonic (nonlinear) terms must be used. A fuller polarisation description is then,

$$P = \epsilon_0 \chi_1 E + \chi_2 E^2 + \chi_3 E^3 + \ldots \tag{1.7}$$

For optical fibre the second order susceptibility, χ_2, which is responsible for second-harmonic generation, vanishes due to the inversion symmetry of molecular silica. Thus the lowest order nonlinear effects in fibre arise from the χ_3 term, the major contribution of which is that of nonlinear refraction *i.e.* the intensity dependence of refractive index giving a total material index,

$$n(\omega, |E|^2) = n(\omega) + n_2 |E|^2 \tag{1.8}$$

where n(ω) is the linear refractive index contribution, $|E|^2$ is the intensity of the optical field inside the fibre, and n_2 is the nonlinear refractive index coefficient, which has a value of $+2.6\text{x}10^{-20}$ m^2W^{-1} in silica fibre [26].

This intensity dependence has clear implications for high-intensity ultrashort pulses. Since the central regions of a pulse will "see" a higher refractive index than the low-intensity wings, the propagating pulse will become increasingly phase modulated with distance, developing an instantaneous nonlinear phase,

$$\Delta\Phi_{NL}(t) = -\frac{2\pi n_2 L}{\lambda} I(t) \tag{1.9}$$

where L is propagation distance and I(t) is the pulse temporal intensity profile. This effect is known as self-phase modulation (SPM). Since instantaneous phase becomes time-dependent, the pulse develops a frequency chirp with a magnitude which is proportional to the time-derivative of the intensity profile, as illustrated in fig. 1.3, from which it can be seen that the pulse becomes spectrally broadened and develops a net up-chirp. It is also clear that, since the frequency deviation is dependent on the maximum temporal rate of change of phase, the extent of

spectral broadening increases with power. This is verified by the experimental progression in fig. 1.4 (i) to (iv). The series shows spectra recorded at the output of a 500m length of dispersion shifted fibre (λ_0=1556nm) into which were launched, at gradually increasing power levels, 7ps sech^2 pulses with a spectral width of 0.38nm in the normal dispersion regime. A detailed dispersion profile for this fibre, subsequently referred to as DSF2, may be found in section 2.4.1 of chapter 2.

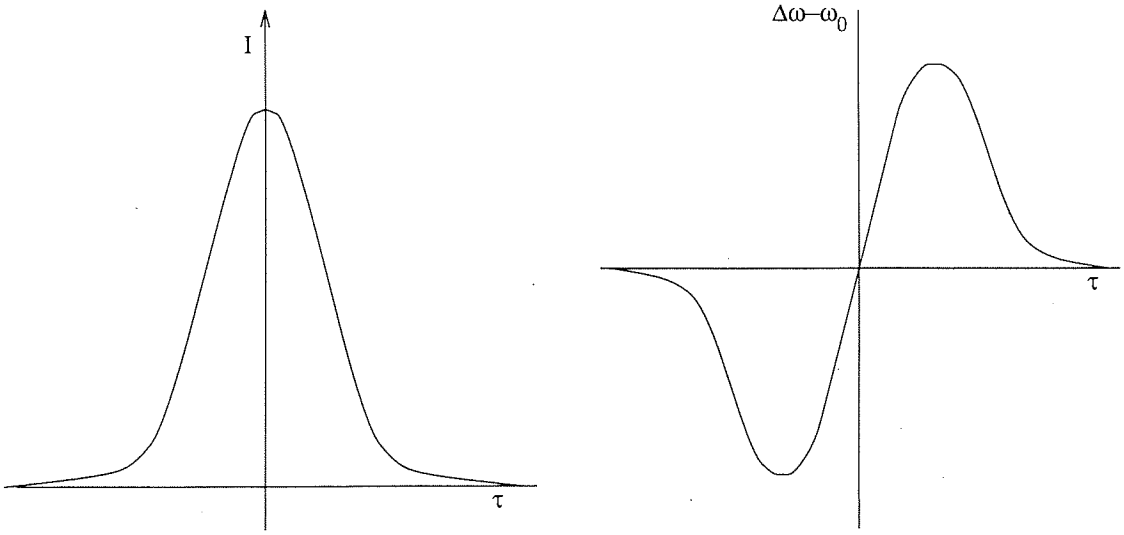

Figure 1.3: Frequency chirp of a high intensity pulse due to self-phase-modulation (SPM). Pulse up-chirped, *i.e.* red-shifted towards the leading edge.

The oscillatory structure of each spectral measurement may be explained by reference to fig. 1.3 from which it can be seen that a given frequency chirp is generated at two temporal positions within the pulse envelope. The two waves produced are, thus, generated with a net phase differential. The measured intensity of a given frequency component, as the vector sum of two such waves, is, therefore, determined by this differential phase. The spectral asymmetry is ascribable to depletion of the leading edge of the pulse due to stimulated Raman generation, a nonlinear effect which will be introduced in a later section.

The most important aspect of SPM from the point of view of this thesis, is its relationship to GVD. It has been shown that SPM leads to the generation of a net up-chirp across a propagating pulse. In the normal regime, in which GVD also leads to an up-chirp, it is clear that SPM will produce an enhancement of dispersion-induced temporal broadening. However, in the anomalous regime

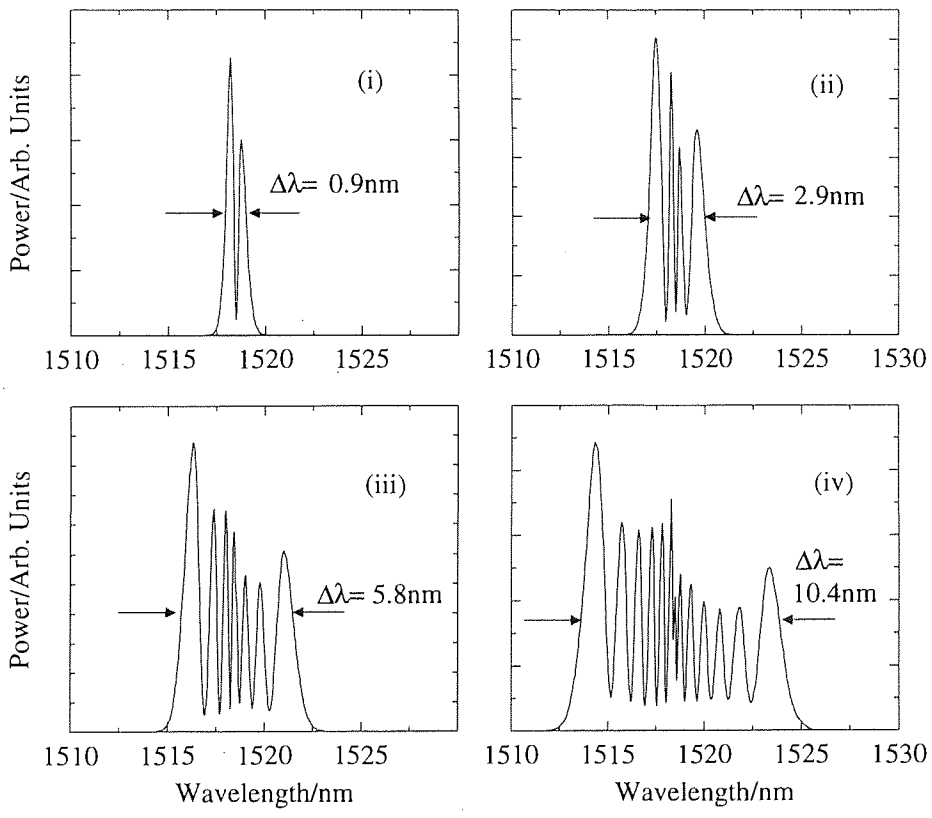

Figure 1.4: Spectra showing spectral broadening, due to SPM, of pulses emerging from a 500m length of dispersion-shifted fibre with increasing input power. Input pulses: $\Delta\tau$ =7ps, $\Delta\lambda$ =0.38nm.

the down-chirping effect of GVD acts in opposition to the effect of SPM. It is conceivable, then, that a specific combination of pulse temporal profile and power exists in which a net equilibrium between these two phenomena will be sustained, with a resultant elimination of temporal broadening. The soliton is such a pulse, and is the subject of the next section.

1.1.4 Optical Fibre Solitons

Pulse propagation in optical fibres with loss may be modelled using the dimensionless nonlinear Schrödinger equation (NLSE) [27, 28],

$$j\frac{\partial u}{\partial z} + j\Gamma u + \frac{1}{2}\frac{\partial^2 u}{\partial t^2} + |u|^2 u = 0 \tag{1.10}$$

where u is the normalised temporal envelope, z is propagation distance, t represents temporal position within the pulse envelope and Γ is fibre loss. For a launched pulse, u(z=0,t), of the form Nsech(t), evolution as a pure soliton occurs within the fibre for integer N. Analytic solutions of the lossless NLSE ($\Gamma = 0$) exist for N=1,2 and are given by,

$$u(z,t) = e^{jz/2} sech(t) \tag{1.11}$$

$$u(z,t) = \frac{4e^{-jz/2}[cosh(3t) + 3e^{-4jz}cosh(t)]}{cosh(4t) + 4cosh(2t) + 3cos(4z)} \tag{1.12}$$

respectively. The most notable aspect of the fundamental (N=1) soliton solution, is that the pulse temporal profile is independent of distance. It is this ability to propagate for long distances without distortion which lies at the root of the considerable interest which has arisen in soliton communication systems. As is clear from eqn. 1.12 the same is not true for higher order (N>1) solitons, a factor which limits their usefulness in transmission systems and in nonlinear switching using the NOLM, as will be discussed in chapter 2.

Another critical aspect is the time-independence of the instantaneous nonlinear phase, a property which is of particular significance for nonlinear interferometric switching, resulting in the maintenance of pulse temporal profile and width on combination of two solitons with the same initial characteristics. Phase

evolution is characterised by the soliton period, z_0 , which defines the propagation distance required for the accumulation of a nonlinear phase of $\pi/4$.

These two fundamental soliton descriptors, *i.e.* soliton order, N, and soliton period, z_0 , are related by the equation,

$$N^2 = \frac{4n_2 z_0 P_0}{\lambda A_{eff}} \tag{1.13}$$

where n_2 is the nonlinear refractive index coefficient for fibre, P_0 is the pulse peak power, A_{eff} is the effective fibre core area and z_0 is given by,

$$z_0 = \frac{0.322\pi^2\tau^2 c}{D\lambda^2} \tag{1.14}$$

where τ is the full-width-half-maximum pulse width and D is the fibre group-delay-dispersion at the pulse centre wavelength, λ . Using typical experimental parameters, the peak power, P_0, for an N=1 soliton in standard single-mode fibre with D=17ps/(nm.km), λ =1550nm, A_{eff} =88μm^2 , τ=7ps, is 1.2W.

In a real system, in which it may not be possible to launch a pulse with the exact required power level, a modified soliton evolution will, nevertheless, still occur. For a generalised launched pulse of the form Asech(t) it has been shown [27] that the propagating pulse asymptotically splits into soliton and noise components. For A=N+α where $|\alpha| < 1/2$, the soliton part corresponds to a pulse of the form

$$(N + 2\alpha)sech\frac{(N + 2\alpha)t}{N} \tag{1.15}$$

Thus, even an approximate soliton exhibits the characteristic behaviour of a soliton.

In the "real-world", however, fibre is not lossless, and for $\Gamma \neq 0$ no analytic solutions of the NLSE exist. In this case, as the pulse propagates, fibre loss results in an exponential decrease in pulse energy as $e^{-2\Gamma z}$ which leads to a corresponding increase in soliton period as $e^{4\Gamma z}$ and an increase in pulse width as $e^{2\Gamma z}$. This adjustment may be understood qualitatively if loss is taken as an adiabatic perturbation. As already discussed, a defining mark of a soliton is the dynamic equilibrium which it maintains between nonlinear chirp due to SPM and dispersive chirp due to fibre chromatic dispersion so that, on average, the instantaneous

frequency across the pulse envelope is constant. As loss causes the pulse energy to decrease, the rate of SPM also falls resulting in an excess of dispersive chirp and necessitating compensation to maintain equilibrium. This is accomplished by a narrowing of the pulse spectral content with a corresponding pulse width increase which scales as $e^{2\Gamma z}$ [27] as described.

Thus, the soliton has a number of attractive properties. It is a pulse which forms a dynamic balance between two potentially detrimental fibre properties, *i.e.* nonlinear and dispersive chirp, with two features which impact positively on its suitability as a data carrier in nonlinear fibre switching systems, namely uniform phase across the whole pulse envelope, and robustness under adiabatic perturbation due to fibre loss. These two features receive more quantitative analysis in the experiments of chapters 2 and 3.

1.1.5 Stimulated Raman Generation

Another nonlinear effect which features strongly in the experimental discussion of this thesis is stimulated Raman generation, an inelastic scattering phenomenon which occurs when a fraction of the energy in the optical wave propagating in a fibre is converted to molecular vibrational modes (page 219*ff* [29]) with a resulting net downshift in the frequency of the wave. The incident optical wave then acts as a pump which feeds the down-shifted field known as the Stokes wave, the initial growth of which is given by the relation,

$$\frac{dI_s}{dz} = g_R I_p I_s \tag{1.16}$$

where I_p is the power in the incident optical field, I_s is the power in the Stokes wave, g_R is the Raman gain coefficient and z is propagation distance. Thus, the rate of growth of the wave is initially proportional to the product of the input optical power and the power in the Stokes wave. The spectrum of the Raman gain coefficient, g_R, which is a measure of the efficiency of transfer of energy to the Stokes wave with frequency, for a pump wavelength, λ_p, of 1μm is shown in fig. 1.5. For other pump wavelengths the shape of the curve remains the same and the absolute frequency shift, which is dependent on the frequency of the incident optical wave, can be found from the inverse relation between g_R and λ_p. It can be seen that the gain spectrum extends continuously over a broad

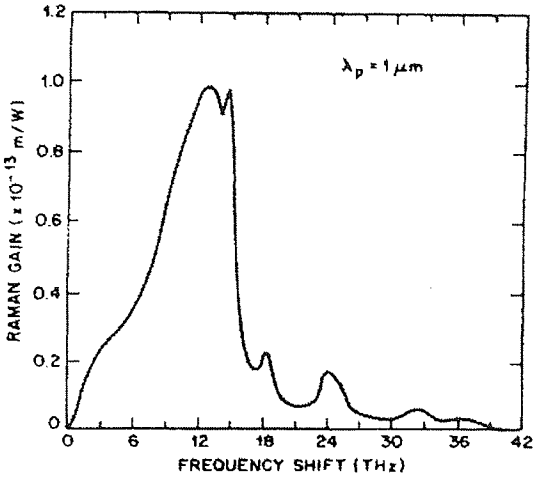

Figure 1.5: Raman gain spectrum with a $1\mu m$ pump.

frequency range of around 40THz with a prominent peak situated, in silica fibre, at a frequency offset of 13.2THz.

By modification of the nonlinear term in the basic NLSE (eqn. 1.10) to include a delayed response, the effect of Raman generation may be modelled [30, 31, 28]. The fuller NLSE is then,

$$j\frac{\partial u}{\partial z} + j\Gamma u + \frac{1}{2}\frac{\partial^2 u}{\partial t^2} + |u|^2 u = au\frac{\partial |u|^2}{\partial t} \tag{1.17}$$

where a is a constant related to the nonlinear susceptibility of the glass.

In soliton systems, stimulated Raman generation is found to cause the optical frequency of a soliton to shift as it propagates [32], a phenomenon known as soliton self-frequency shift (SSFS). This is due to a self-pumping (intrapulse) effect in which energy is transferred from the higher to the lower frequency parts of the spectrum, at a rate which increases in strength as τ^{-4} where τ is the soliton pulse width. This dependence is due to a combination of the τ^{-2} dependence of soliton peak power and the τ^{-1} dependence of the pulse spectral width. The effect, therefore, becomes more pronounced as pulse width decreases since the corresponding increase in pulse peak power results in a higher rate of growth of the Stokes wave while the increase in spectral width results in a higher degree of overlap of the pulse spectrum with the Raman gain curve with a consequent

increase in efficiency of energy transfer. In addition, it has been shown that this intrapulse Raman shift ultimately causes the break-up (decay) of higher order solitons into their single soliton components [33, 34].

1.1.6 Cross-Phase-Modulation

A further nonlinear effect which is of great importance in nonlinear switching is cross-phase-modulation (XPM) which, like SPM, is a manifestation of third-order nonlinearity. XPM is the induced nonlinear phase shift on an optical field due to a co-propagating field at a different wavelength or polarisation. The accumulated nonlinear phase for a field E_1 must be modified to include this effect so that the total becomes the sum of contributions from both SPM and XPM given by,

$$\Phi_{tot} = \frac{2\pi n_2 L}{\lambda}(|E_1|^2 + 2|E_2|^2). \tag{1.18}$$

where E_2 is the magnitude of the co-propagating field. The interdependence of optical fields due to XPM has obvious implications for ultrafast control of optical data. XPM may be used in the development of systems with functionality which is based on the correlation between independent data streams such as logic and routing. In the nonlinear domain, the exploitation of this effect is a primary concern in all-fibre switching.

1.2 Nonlinear Fibre Switching

With the need to manage and process ever-increasing volumes of data, there has also arisen a great deal of interest in all-optical switching [35, 36, 37, 18]. The current section introduces a number of all-fibre devices which have attracted particular attention providing for each, a brief outline of operating principles and most important features.

1.2.1 Nonlinear Directional Coupler

The nonlinear directional coupler (NLDC) [38] is an intensity dependent routing switch which operates by nonlinear detuning of the mode-coupling between two waveguides in close proximity. A schematic of this device is shown in fig. 1.6. For

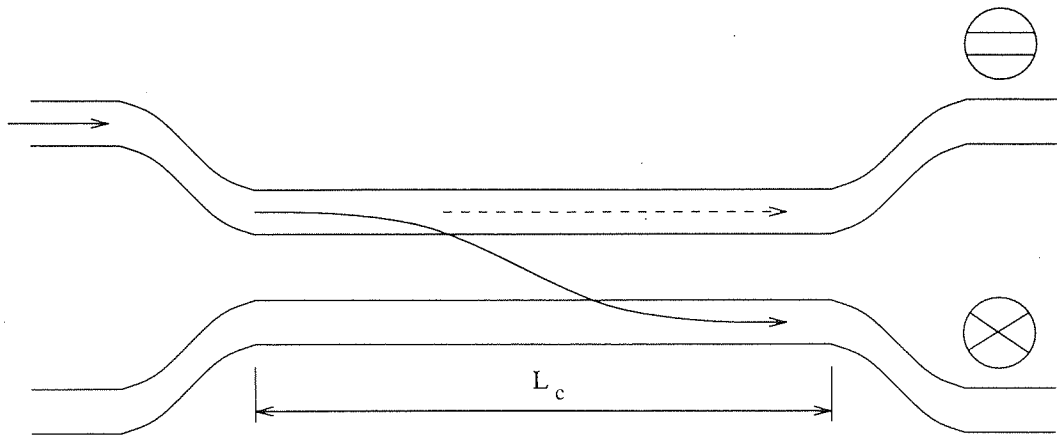

Figure 1.6: Schematic of a nonlinear directional coupler switch. Solid line indicates linear operation of device; dotted line indicates nonlinear operation.

a low power input signal, mode-coupling due to evanescent field overlap causes a periodic exchange of energy between the waveguides, the period of which is defined by the coupling length, L_c, the distance required for complete transfer of energy from the input arm into the other guide. A coupler of physical length, $L=L_c$, is ordinarily in its cross state, as shown by the solid line in the diagram.

As the input power is increased, L_c gradually increases due to SPM until a critical power is reached at which it approaches infinity. For a NLDC of length L_c, an input above the critical power will switch the device into the bar state as illustrated by the dotted line in fig. 1.6

In practice, the critical power has been found to be prohibitively high with switching powers in the region of several nJ [39]. In addition, although the NLDC has the sharpest CW switching characteristic of any device proposed to date, demonstrations so far have shown only very poor switching contrast ratios, a direct result of the inability to support solitons of devices investigated. It has already been shown that the phase of the soliton is constant across the envelope leading to what has been termed "particle-like" or "atomic" behaviour, descriptions which lead on from its persistence as a solitary wave. Consequently, modification of the NLDC to support solitons has been shown to be capable of effecting whole pulse switching [40]. However, even for pulses as short as 100fs, required device lengths are well in excess of 1m, posing significant manufacturing diffi-

culties and rendering the device highly sensitive to environmental disturbances. Thus, the NLDC has significant drawbacks in its all-fibre form.

1.2.2 Soliton Trapping and Dragging

Alternative switches based on soliton trapping and dragging, in which the nonlinear coupling between a control and signal pulse at orthogonal polarisations causes "switching" by temporal displacement [41], have been used in implementations of a number of primitive logic functions [42, 43, 44, 45, 46]. Switching power levels in these devices are significantly lower than for the NLDC with required pulse energies of ~40pJ and 6pJ for trapping and dragging gates respectively.

The principle advantages of these are, therefore, their low switching thresholds, and, in the case of soliton dragging gates, inherent gain. However, outweighing these considerations are the requirements of tight relative polarisation control and need for extremely long fibre lengths of around $30z_0$ for sufficient time displacement due to dragging.

1.2.3 Switching by Kerr-Induced Polarisation Rotation and XPM-Induced Spectral Shift

Two further devices, with outputs which are modulated in amplitude rather than temporal position, are those relying on Kerr-induced polarisation rotation and XPM-induced spectral shifting. An outline schematic of a typical Kerr gate is shown in fig. 1.7. These switches are classified together due to their similarity of rationale, each using a nonlinearly induced change due to a strong control pulse on a weak signal pulse in combination with an appropriate discriminating element. In the first case, the nonlinear refractive index change induced by a control signal is used to effect a change in the polarisation state of the signal. Discrimination is then performed using a polarising beam splitter [47, 48, 49]. Measured switching energies for this device are ~50pJ. In the spectral switch, XPM-induced spectral shift of the low power input signal is converted into an amplitude response by passive filtering at the output of the device [49, 50].

Although both configurations are inherently simple, neither is cascadable with itself: the polarisation switch requiring not only careful control of input polarisation, but also leaving the emerging signal altered in polarisation state; and the

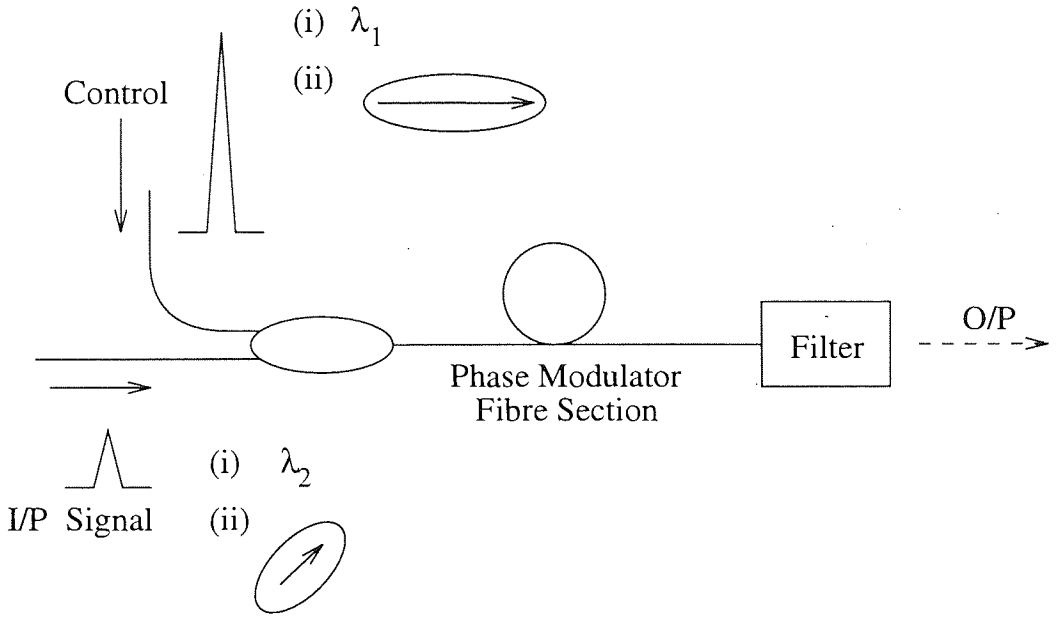

Figure 1.7: Outline schematic of a nonlinear Kerr gate.

spectral-shifting configuration leaving the output altered in wavelength.

1.2.4 Nonlinear Mach-Zehnder Switch

A final all-fibre switch, and one similar in operation to the NOLM, is the nonlinear Mach-Zehnder interferometer. This device exhibits a periodic nonlinear transmission characteristic due to differential self- [51, 17] or cross-phase modulation [52] each of which causes a net imbalance in transmission distance between its arms as shown in fig. 1.8. The nonlinear Mach-Zehnder switch is a low switching-threshold device and, as one which is compatible with soliton formation, is inherently capable of whole-pulse switching due to the constant-phase property of this form of input. However, in practice, it is highly sensitive to environmental disturbances requiring dynamic control to maintain interferometric balance [53].

Thus it is clear that a number of all-fibre optical switching methodologies exist. It is also apparent that each of these options has significant drawbacks. The work contained in the rest of this thesis is centred on an alternative fibre device, the nonlinear-optical loop mirror (NOLM) [19]. The NOLM is an inherently bal-

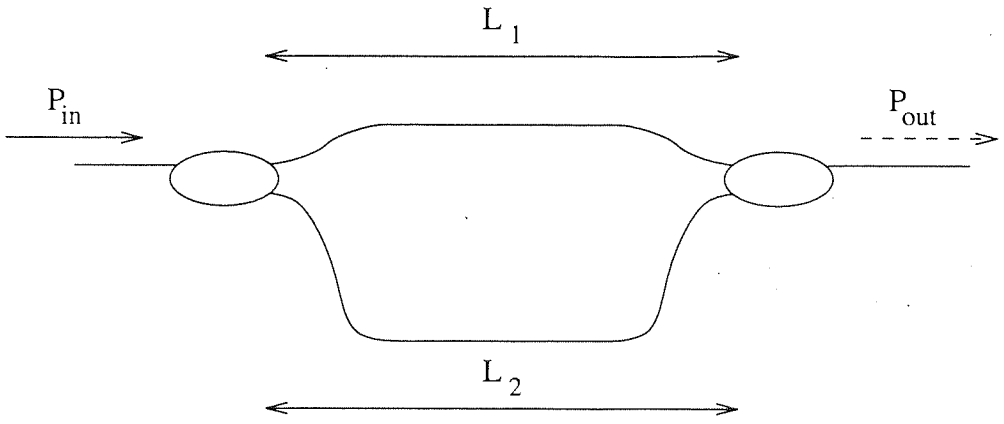

Figure 1.8: Schematic of a nonlinear Mach-Zehnder switch.

anced interferometric device which is cascadable as will become clear from the experimental studies carried out, more environmentally robust than its counterpart, the nonlinear Mach-Zehnder switch, and has low switching thresholds on the order of a few tens of pJ. Additionally, as a device which, in its all-fibre form, may be configured to support soliton propagation, whole-pulse switching may be achieved over eminently practical fibre lengths.

1.3 Overview of Thesis

This thesis aims to provide a detailed experimental analysis of the suitability of the NOLM as a processing element in all-optical switching architectures. As processing systems are inherently composed of combinations of functional units, it is essential to evaluate the ability of any device to be cascaded both with itself and other devices. Thus, preliminary experiments are directed at establishing the cascadability of the NOLM in terms of the impact of cascading on the overall amplitude response of the device as well as on data integrity after transmission through a series of devices.

Chapter 2 presents results from foundation experiments to characterise a single NOLM, a natural starting point for an extended study of multi-device configurations. Soliton regime self-switching is investigated using input pulses with

durations an order-of-magnitude greater than in previous experimental investigations [41, 54]. The primary restriction on the extent of the NOLM switching characteristic is self-Raman generation which leads to imperfect interference due to soliton self-frequency shift [30] (SSFS) and higher-order soliton decay [33, 34]. By choosing relatively long pulses with narrower spectral content, this failure is postponed due to accompanying reductions in soliton power and spectral overlap with the Raman gain spectrum. A systematic numerical study of this phenomenon is presented which charts the gradual degradation of the switching characteristic with decreasing input pulse width, and hence, increasing self-Raman generation. The results show that, over the first two switching peaks, no appreciable increase in switching efficiency is obtained by a further increase in pulse width.

It is not enough, however, to restrict analysis to the amplitude response of the device. It is also essential to quantify the effect of switching on the temporal and spectral integrity of pulses switched. By comparing the characteristics of pulses emerging from the device with those at the input, it is found that transmission through the NOLM does not significantly degrade the essential soliton characteristics of incident pulses, providing further evidence for the robustness of the soliton as a data carrier, and showing that data passing through the device is rendered capable of further processing.

This hypothesis is tested in chapter 3 by analysing the response of a cascade of two devices to a train of input solitons with the same duration as those in the study of chapter 2. A simple model is developed which enables the designer to construct an optimal two-device cascade so that the characteristics of each are matched to compensate for fibre loss. The amplitude response of such an optimal cascade is shown to be significantly enhanced, with steeper switching edges, and flattened peaks giving a configuration with increased amplitude discrimination and immunity to input amplitude noise. In line with the findings of chapter 2 it is found that pulses emerging, even from a two-device cascade, still retain their essential soliton character, verifying, not only that pulses emerging from a single device may be processed further, but that the soliton has significant advantages in nonlinear processing.

In addition to addressing the tailoring of amplitude response, the chapter goes on to present a technique for quantisation of the spectral response of the NOLM, enabling application in wavelength-division-multiplexed (WDM) systems

where wavelength selectivity is of prime importance. By reconfiguring the NOLM to include an asymmetrically arranged in-fibre Bragg reflector as a wavelength-selective loss element, both soliton self-switching and dual-wavelength control-pulse switching are spectrally confined with operation being restricted only to wavelengths lying inside the reflection band of each grating.

The next two chapters present results from NOLM-based configurations for ultrashort pulse generation and control. Chapter 4 introduces a novel all-fibre dual-wavelength laser configuration which uses the NOLM as an amplitude modulator to simultaneously mode-lock two cavities incorporating chirped fibre Bragg gratings as end-mirrors. The use of a dual-cavity configuration with spectrally selective end-mirrors enables arbitrary and accurate wavelength definition across the entire erbium gain band, an inherent requirement of WDM systems. As the dominant source of intracavity dispersion, Bragg gratings are shown to provide a convenient means of tailoring the overall dispersion and consequently, also, the pulse characteristics of each cavity. The laser generates synchronised, independently dispersion-tunable pulse trains with an ultra-low rms inter-pulse-stream timing jitter level of 630fs. Timing jitter is a critical parameter for the error-rate performance of an optical switch. The value measured enables successful *i.e.* producing error-rates of below 10^{-9}, application of this laser configuration to NOLM-based switching environments at speeds in excess of 130GBits/s.

Chapter 5 presents results from two further NOLM-based configurations for memory and phase-locking. The first configuration is a novel all-optical memory based on a sequential combination of two NOLM's with feedback which is shown to perform storage and inversion of a 0.5kByte random data sequence. In the second, the NOLM is used as an all-optical phase-detector in a phase-locked-loop (PLL) configuration. The use of the NOLM enables phase-locking not only to the system baseband frequency, but also to harmonics and sub-multiples. Results are presented showing phase-locking of a gain-switched distributed feedback (DFB) laser to the seventh and fourteenth harmonics of a 76MHz reference.

Chapter 2

Characterisation of a Nonlinear-Optical Loop Mirror

2.1 Introduction

The previous chapter introduced a number of nonlinear fibre devices which have been investigated both experimentally and theoretically as potential candidates for inclusion in all-optical data processing systems, and identified a number of drawbacks inherent in each. The current chapter presents an introduction to an alternative device, the nonlinear-optical loop mirror (NOLM) which combines a number of features which make it a more attractive primitive switching element for use in more complex systems. Before going on, in subsequent chapters, to provide experimental results demonstrating the use of this device in higher level configurations, the current discussion provides an introduction to the fundamental concepts of operation of this device.

The first section presents a graphical description of the fibre loop mirror, from which the NOLM is largely derived, and shows that by the introduction of a differential phase shift of π in the counter-propagating fields of the device, a switch from its normal operation of 100% reflection to 100% transmission may be achieved. After outlining the principles governing nonlinear switching in the NOLM, results from an experimental investigation of ultrafast self-switching using the device are presented. The effects of transmission through a NOLM on the spectral and temporal characteristics of an incident soliton data stream are evaluated and it is found that emerging pulses largely retain their soliton characteristics. The results demonstrate that the input data stream is not significantly degraded by propagation through the device and, consequently, that the output data is capable of further manipulation. This fact also illustrates that the NOLM is cascadeable, a property which is a primary requirement for any device within a data processing architecture and, additionally, confirms the robustness of the soliton, further recommending its use as a data carrier in ultrafast all-optical processing environments.

The results also provide a first-time demonstration of multiple-peaked switching in this device [55]. By using relatively long pulses (~7ps), the effect of intrapulse Raman generation, an effect whose strength is critically dependent on pulse width and which leads to both soliton-self-frequency shift (SSFS) [30] and break-up of higher order solitons [56, 57, 58], is postponed, thereby extending device operation beyond the limits previously reported. The influence of this effect is treated in detail in section 2.5, where results from a series of numerical simulations are presented which summarise the impact of this phenomenon on the device by systematically charting the degradation of a NOLM switching characteristic with decreasing incident pulse width.

2.2 Fibre Loop Mirror

As stated in the introduction, this section presents a graphical description of the principle of operation of the fibre loop mirror, the primitive form of the NOLM. It is shown that the reflectivity of the device can be varied from zero to 100% by appropriate adjustment of the internal loop birefringence. This "switching" of the light from the input to the output port is achieved by the introduction of a differential phase shift of π between the counter-propagating components in each arm.

A schematic of a fibre loop mirror is shown in fig.2.1. The device consists of a 50/50 fused-fibre coupler with ports three and four joined by a loop of fibre [59]. Operation of the device is summarised simply as follows. Light input at port 1 is split equally into two counter-propagating components, E_3 and E_4. In cross-coupling, the counter-clockwise component, E_4, receives a phase lag of $\pi/2$ with respect to the straight-through component. On returning to the coupler, the transmitted intensity at port 2 is the sum of two signals of equal intensity: a counter-clockwise signal with phase $\phi - \pi$ due to twice cross-coupling; and a clockwise component of phase ϕ, where ϕ is the phase accumulated by both components due to propagation over the loop length, L. The relative phase differential of π results in zero transmitted intensity at port 2 and 100% reflection back through port 1 due to conservation of energy (illustrated by the dotted vector). Although this description outlines the basic aspects of operation of the loop mirror, it does not address the issue of internal fibre birefringence. The following

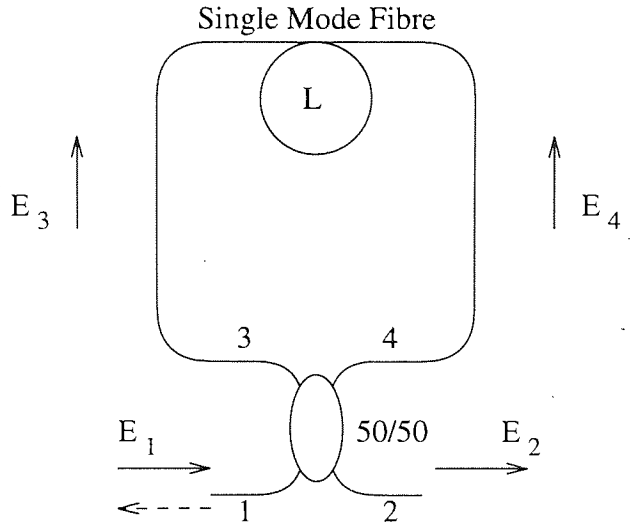

Figure 2.1: Schematic of a fibre loop mirror.

discussion provides a fuller description which includes this parameter.

Figure 2.2 summarises the principle of operation of the device for the case of light incident at port 1 and no loop birefringence. For simplicity, the loop mirror is assumed to lie in the horizontal xz plane and the incident signal is assumed to be linearly polarised in the orthogonal xy plane with arbitrary polarisation, θ, to the y axis. On reaching the coupler, 50% of the input light is cross-coupled to port 4 and receives a $\pi/2$ phase lag with respect to the straight-through component as already described. The polarisation orientations of the components E_3 and E_4 as they leave the coupler are shown on axes (a) and (b) respectively, of the lower diagram of fig.2.2. The components meet at the loop midpoint and return to the coupler with polarisation angles of $-\theta$ as shown on axes (c) and (d). Since the path length for each is the same, the $\pi/2$ phase discrepancy between the components is preserved with the result that the combined signal exits at port 1 with a polarisation of $-\theta$ to the y axis, as illustrated by the dotted vector of fig.2.2.

By varying the internal loop birefringence, which results in a polarisation dependent phase change in the counter-propagating components, the loop mirror may be configured for transmission rather than reflection, as illustrated in fig. 2.3. In this case, the loop includes an asymmetrically placed half-wave plate which is located close to port 4 of the coupler with its fast axis oriented at 45^o to the plane of the loop. For a half wave plate, light incident along the fast axis receives a π

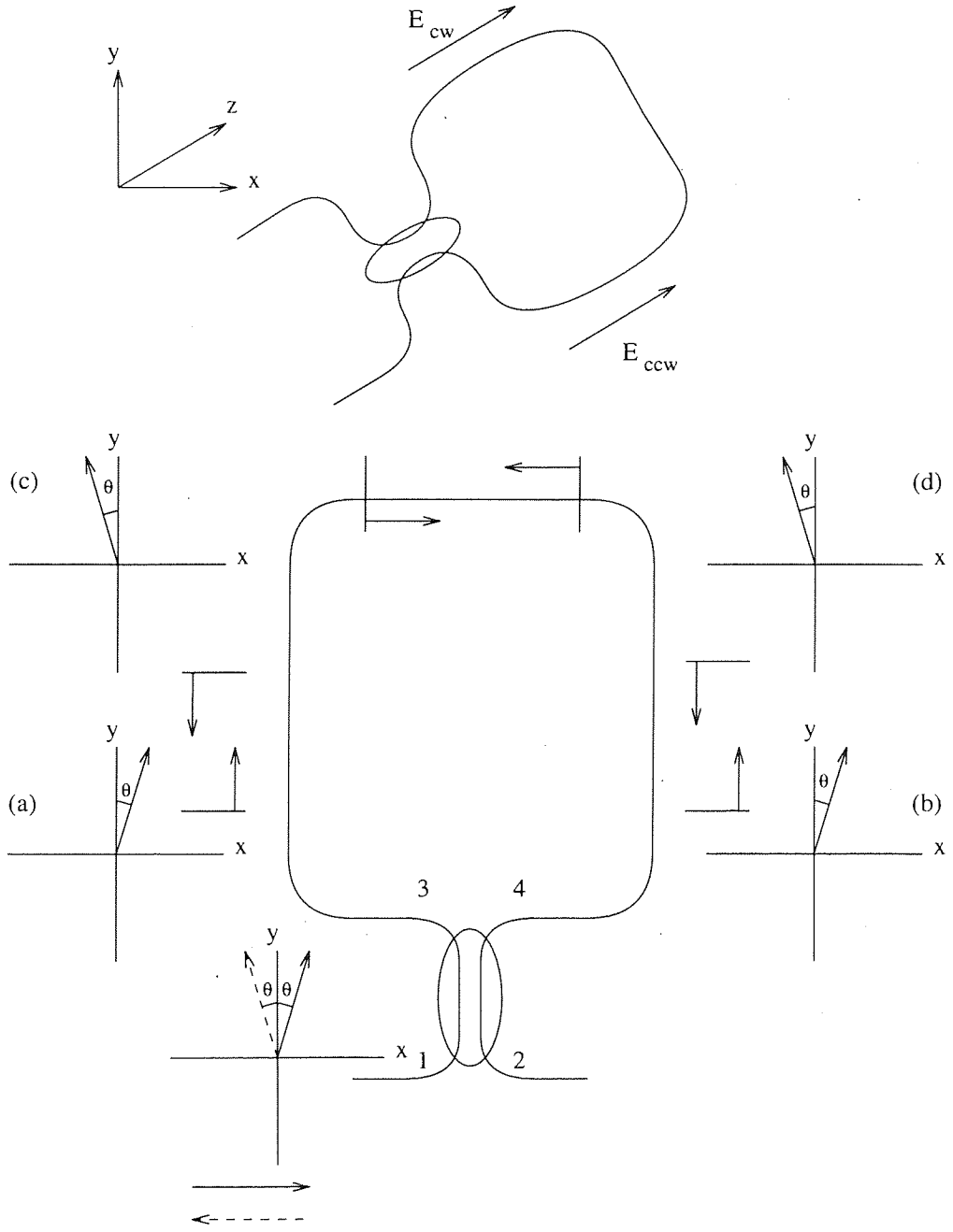

Figure 2.2: Graphical summary of operation of a fibre loop mirror with no internal birefringence.

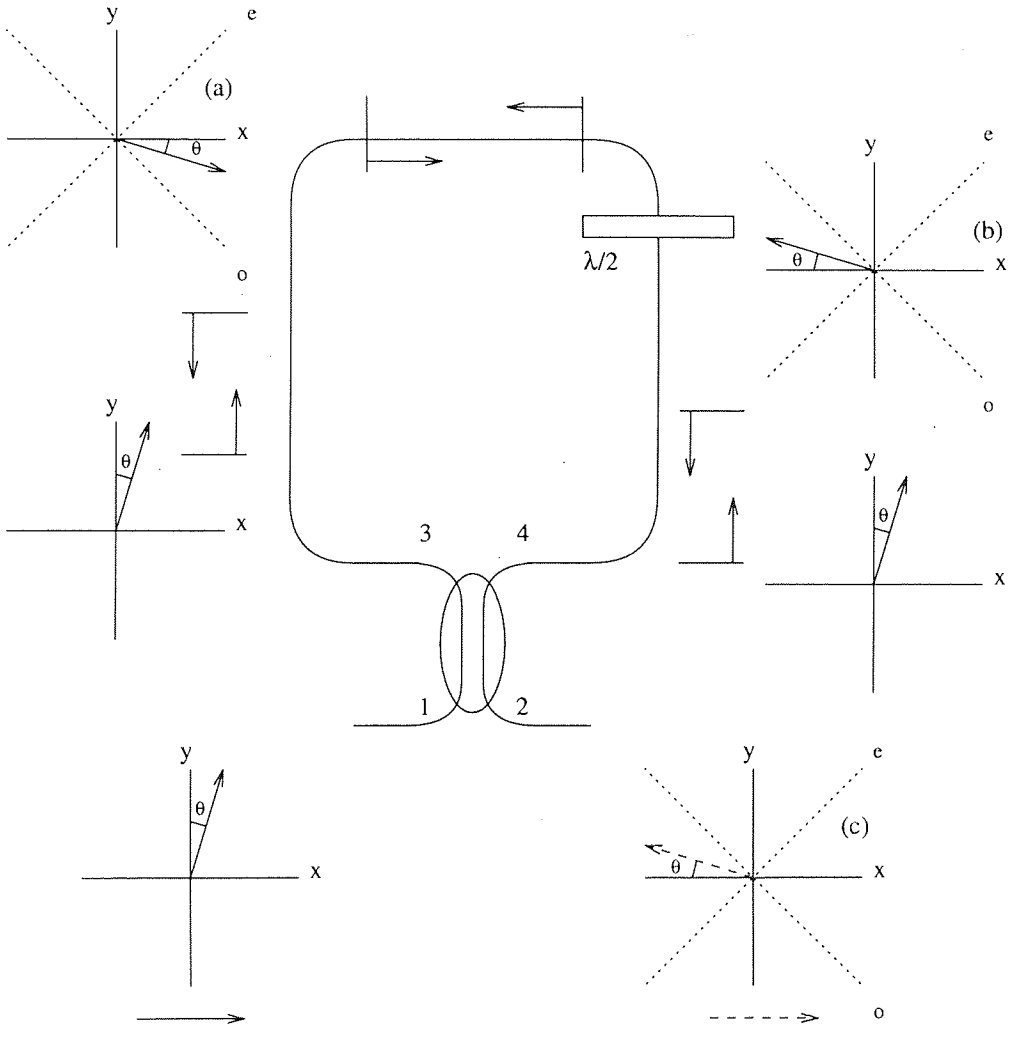

Figure 2.3: Graphical summary of operation of a fibre loop mirror with additional loop birefringence.

phase advance with respect to light incident along the slow axis. In terms of its effect on polarisation angle; for a field incident at an angle γ to one of the axes, this gives rise to a rotation of 2γ. Analysing the counter-propagating field vectors in turn: the components E_3 and E_4 arrive at the wave-plate with polarisations $+\theta$ and $-\theta$ respectively. On passing through it, the two are rotated in the the same direction and exit at angles of $-90-\theta$ and $-90+\theta$. As a result, on returning to the coupler, the polarisation axes are again parallel (see fig.2.3 (a) and (b)), but of opposite sense, a situation which is equivalent to the accumulation of an additional phase differential of π. This accumulated phase differential causes constructive interference at port 2 due to the additional cross-over, and light is transmitted at an angle of $-90+\theta$ (c).

It is, therefore, clear that the introduction of a differential π phase shift between the counter-propagating components provides a technique by which light is transmitted rather than reflected, enabling the device to perform the function of a switch. It is by exploitation of fibre nonlinearity that this action is achieved in the nonlinear-optical loop mirror switch, and this is the subject which is addressed in the next section.

2.3 Nonlinear-Optical Loop Mirror

As already stated, the NOLM is a derivative of the fibre loop mirror. Although the overall construction is the same, consisting of a fused-fibre coupler with its ends joined by a length of fibre, the crucial difference lies in the asymmetric splitting ratio *i.e.* $\alpha \neq 50\%$ [19]. It is, therefore, a fibre implementation of the nonlinear antiresonant ring interferometer [60]. The effect of this imbalance on the operation of the device as a linear reflector, *i.e.* for signals of low intensity in which nonlinear effects can be considered negligible, is to degrade the maximum achievable reflectivity to a value of less than 100% [59]. Owing to self-phase modulation (SPM), *i.e.* the intensity dependence of the refractive index, counter-propagating fields with intensities high enough for nonlinear effects to become significant no longer travel through the same path length. In this way, the interference conditions at the coupler become intensity dependent so that when a differential phase accumulation of π occurs, switching is achieved.

The equations governing the operation of a fibre coupler on an optical field

are given by,

$$E_3 = E_1\sqrt{\alpha} + jE_2\sqrt{1-\alpha} \tag{2.1}$$

$$E_4 = jE_1\sqrt{1-\alpha} + E_2\sqrt{\alpha} \tag{2.2}$$

Taking the case already discussed for the basic fibre loop mirror of light input at port 1: after application of the coupler equations 2.1 and 2.2 followed by transmission through a fibre loop of length L, the nonlinear phase accumulated by each field, on return to the coupler, is given by,

$$E_3 = \alpha^{1/2}E_1 exp(j\alpha\frac{2\pi n_2|E_1|^2L}{\lambda}) \tag{2.3}$$

$$E_4 = j(1-\alpha)^{1/2}E_1 exp(j(1-\alpha)\frac{2\pi n_2|E_1|^2L}{\lambda}) \tag{2.4}$$

where λ is the optical wavelength, and n_2 is the third order nonlinear coefficient in the glass. The term $|E_1|^2$ is the intensity of the optical field in the fibre and is given by P_{in}/A_{eff}, where P_{in} is the incident optical power at port 1 and A_{eff} is the fibre effective core area. Combining these fields gives the transmitted intensity function,

$$|E_2|^2 = |E_1|^2(1 - 2\alpha(1-\alpha)\{1 + \cos[(1-2\alpha)\frac{2\pi n_2|E_1|^2L}{\lambda}]\}) \tag{2.5}$$

It is clear from this expression that 100% transmission occurs when

$$\cos(1-2\alpha)\frac{2\pi n_2|E_1|^2L}{\lambda} = -1 \tag{2.6}$$

i.e.

$$\frac{2\pi n_2|E_1|^2L}{\lambda} = m\frac{\pi}{1-2\alpha} \tag{2.7}$$

where m is an odd integer, and minimum transmission occurs for even m with

$$|E_2|^2 = |E_1|^2(1 - 4\alpha(1-\alpha)). \tag{2.8}$$

Thus, for a splitting ratio, α, of 0.4, the output swings from 4% of P_{in} to 100% of P_{in}, neglecting fibre loss. Figure 2.4 shows the transfer function computed

for two values of α of 0.1 and 0.4 with $n_2 = 2.6 \times 10^{-20} m^2 W^{-1}$, $\lambda = 1550nm$, $A_{eff} = 50\mu m^2$ and loop length, L=1km. The sinusoidal nature of this switching

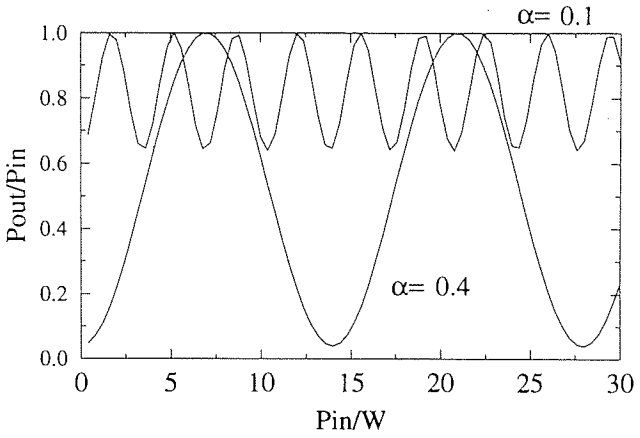

Figure 2.4: Output intensity against input intensity for a 1km NOLM.

characteristic, calculated for a series of single-valued input intensity levels, has implications for a pulsed input signal. It is clear that the higher intensity central regions of a pulse will be preferentially transmitted resulting in significant pulse shaping. This saturable absorption property has been put to positive use in passively modelocked fibre lasers [61], and enables the "cleaning-up" and reshaping of distorted non-soliton pulse trains [62, 63]. It might appear that whole-pulse switching may only be achieved with a square-pulse transmission format such as NRZ. However, the properties of the soliton outlined in Chapter 1 mean that this is not the case. Firstly, since the phase of a soliton is constant across the whole pulse [16] and since the shape of an exact single soliton does not change with propagation distance, the interference of two pulses of the same width will result in the preservation of the pulse temporal profile. Secondly, since the overall nonlinear phase shift, which is proportional to distance [27], is dependent on the pulse peak amplitude [19], the potential for differential nonlinear phase accumulation is evident. The combination of these factors makes whole-pulse switching using the NOLM a reality in both soliton switching and transmission systems, where its potential use as a noise suppressor in short-pulse soliton transmission has been investigated [64, 65]. Thus, it is to an experimental investigation of soliton switching in a NOLM that the rest of the chapter is addressed.

2.4 Experimental Characterisation of Soliton Switching in a NOLM

Having detailed the operating principles of the device, the current section deals with an experimental investigation of soliton switching in a NOLM with an unbalanced coupler, the operation of which is outlined above. After presenting a detailed analysis of the effects of application of the device to a train of picosecond regime solitons, results from a series of numerical simulations are presented which systematically characterise the effect of self-Raman generation on the device's switching characteristic.

2.4.1 Fibre Characterisation

Before experimental parameters can be calculated, information on both fibre dispersion and nonlinearity must be evaluated. The current section, therefore, provides a description of the experimental technique used to measure the dispersion characteristics of the range of three fibres used throughout this thesis. Two fibre types appear: standard, single-mode telecommunications fibre (STF); and dispersion shifted fibre (DSF). An estimation of the value for the effective core area of the standard telecommunications fibre used is also presented. Values for these two fibre characteristics must be calculated to enable definition of the fibre lengths required to obtain 100% transmission for a given input power level.

Figure 2.5 shows a schematic of the experimental configuration used to measure fibre dispersion. 7ps pulses at a repetition rate of 76MHz from a tunable, modelocked F-centre laser, synchronously pumped using 100ps pulses from a Nd:YAG laser, were launched into a 50/50 coupler as shown. One portion of the split signal was then detected using a 45GHz photodetector and used to trigger a HP54124T sampling oscilloscope. The other portion of the split signal was launched into the sample fibre and the output viewed on the sampling oscilloscope after detection by an identical photodiode. While viewing the received pulse train, the power launched into the fibre was adjusted so that pulse breakup due to self-Raman generation [56] did not occur, and "clean" pulses were seen. As the laser wavelength is tuned, the pulse arrival time, with respect to the trigger, of a pulse N pulse intervals later, after transmission through the sample fibre, will

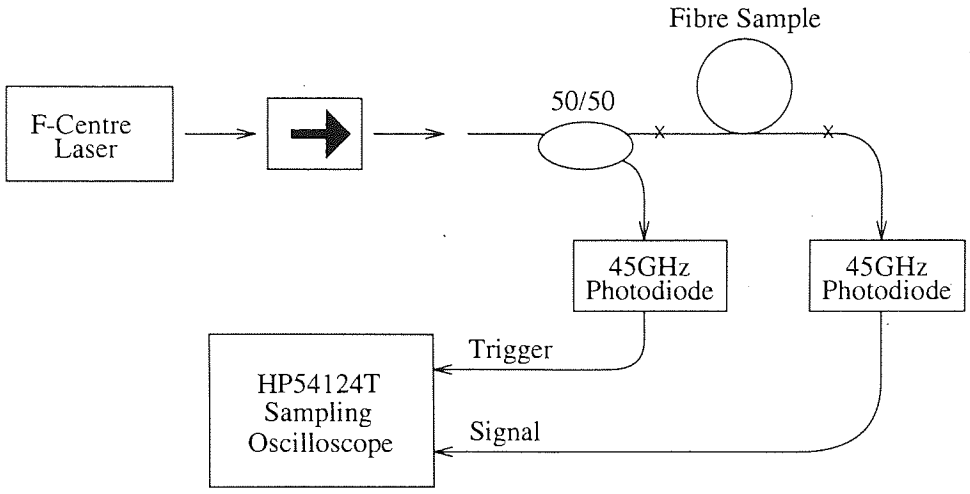

Figure 2.5: Schematic of experimental configuration for measurement of fibre dispersion.

also vary due to the fibre's chromatic dispersion. Thus, by recording this change in arrival time with wavelength, a curve of group-delay against wavelength may be plotted. The fibre dispersion can then be calculated by simply differentiating the best-fit curve to this data. Figure 2.6 summarises the dispersion characteristics for the three fibre samples. Figure 2.6 (i) shows the curve for standard fibre and figures 2.6 (ii) and (iii) the curves for two types of dispersion-shifted fibre, hereafter known as DSF1 and DSF2. Table 2.4.1 provides a summary of the specified fibre dispersion parameters for each fibre type along with the corresponding measured values. Columns 2 and 3 present the values of group delay dispersion specified by the manufacturer, $D_2(spec.)$, at 1550nm and those measured, *i.e.* $D_2(meas.)$. Since a figure at 1550nm is not available for standard fibre, only λ_0 is given.

Fibre Type	$D_2(spec.)$, ps/(nm.km)	$D_2(meas.)$, ps/(nm.km)
Corning, STF SM1399/P2511-R	λ_0=1310nm	17ps/nm.km
Corning, DSF1 SMF/DS(TM)	$\leq$2.7	-0.03 ($\lambda_0 = 1551nm$)
Corning, DSF2 SMF/DS(TM)	$\leq$2.7	-0.5 ($\lambda_0 = 1556nm$)

When the group-delay against wavelength curves were plotted it was found,

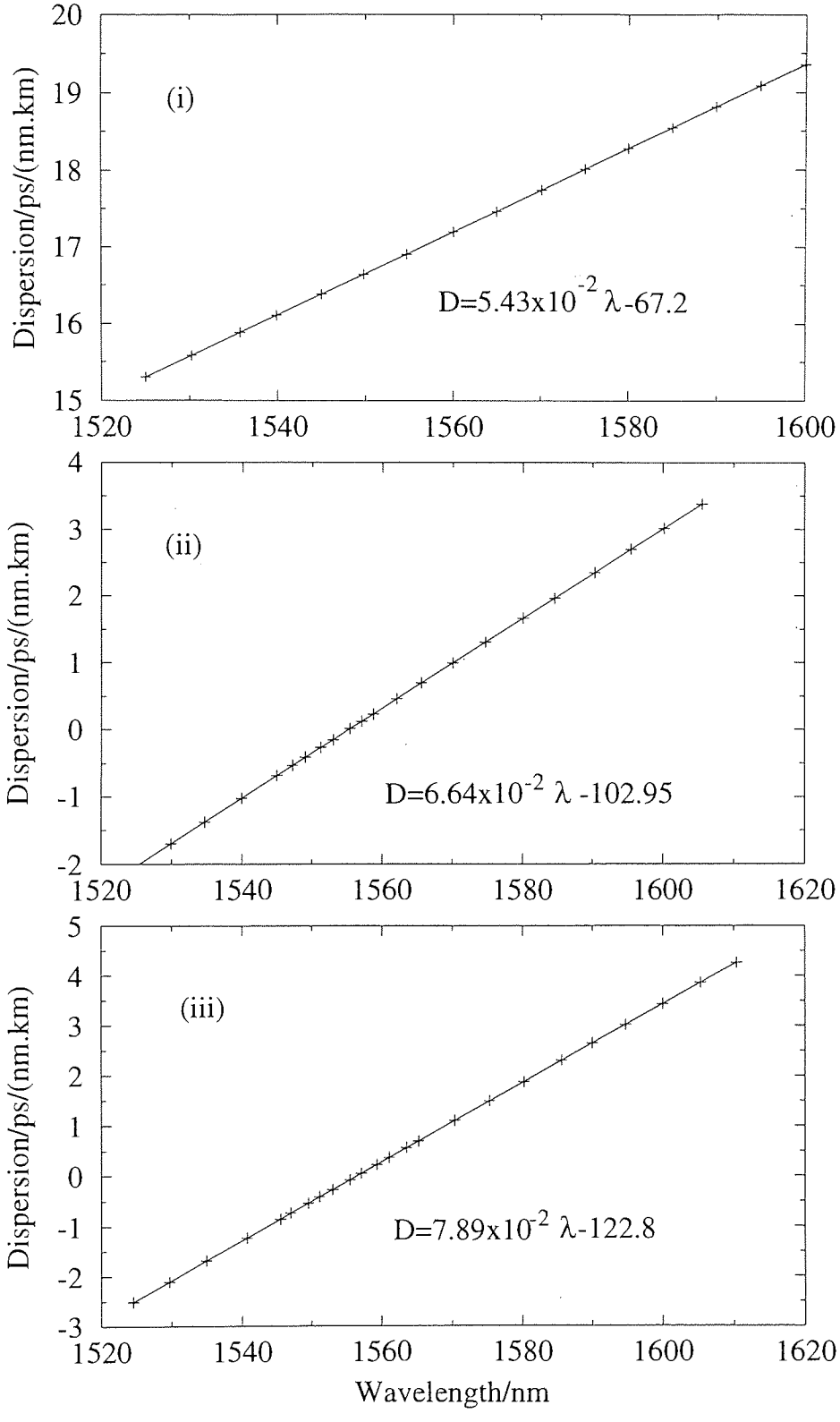

Figure 2.6: Experimentally determined fibre dispersion characteristic and best-fit curves for (i) standard telecommunications fibre (STF), (ii) dispersion shifted fibre. λ_0=1551nm (DSF1), and (iii) dispersion shifted fibre. λ_0=1556nm (DSF2).

in all cases, that the best-fit curves were quadratic with the result that, when differentiated, the dispersion against wavelength relationships were linear. The equations for each are shown on the corresponding characteristic. Using these relationships, the dispersion for standard fibre was found to be +17ps/(nm.km) at 1550nm, and the zero dispersion wavelengths for the two dispersion shifted fibre samples were found to be λ_0=1551nm for DSF1 and λ_0=1556nm for DSF2.

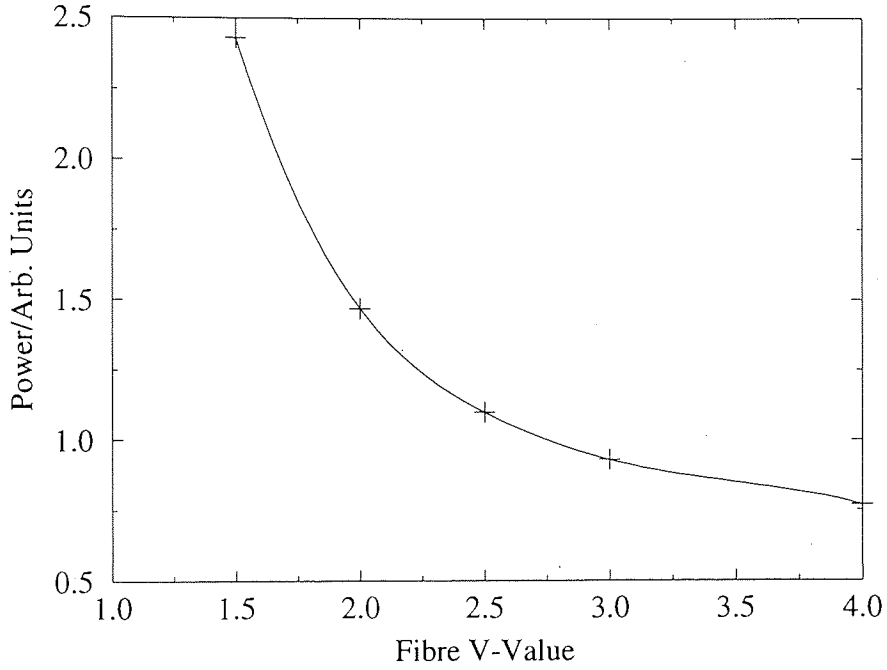

Figure 2.7: Plot of variation of A_{eff} with fibre V-number.

Since a fraction of the guided energy in a fibre propagates in the cladding, the magnitude of the SPM is not simply related to the absolute fibre core diameter, but to the effective area which depends on the optical field distribution within the fibre (page 40, [29]). The variation of effective area, A_{eff}, with fibre V-number is shown graphically in fig. 2.7. The V-number is a dimensionless number which determines the number of modes supported by a fibre and is given by the standard equation $V = \sqrt{(2\pi a/\lambda)^2(n_1^2 - n_2^2)}$ (page 44, [24]) where a is the core radius, and n_1 and n_2 are the core and cladding refractive indices respectively. Knowing the cut-off wavelength for this fibre i.e. the V-number above which the fibre ceases to be single-mode, and the value of A_{eff} at 1310nm, the fibre's core area could be calculated and was found to be $58\mu m^2$. The V value at 1550nm was then calculated and was found to be 1.99 giving a ratio from the graph of

A_{eff}/A_{core}~1.5. Thus, the final value for A_{eff} is taken to be $88\mu m^2$. The value for A_{eff} for Corning dispersion shifted fibre is well known and is taken as $50\mu m^2$ [66].

2.4.2 Experiment

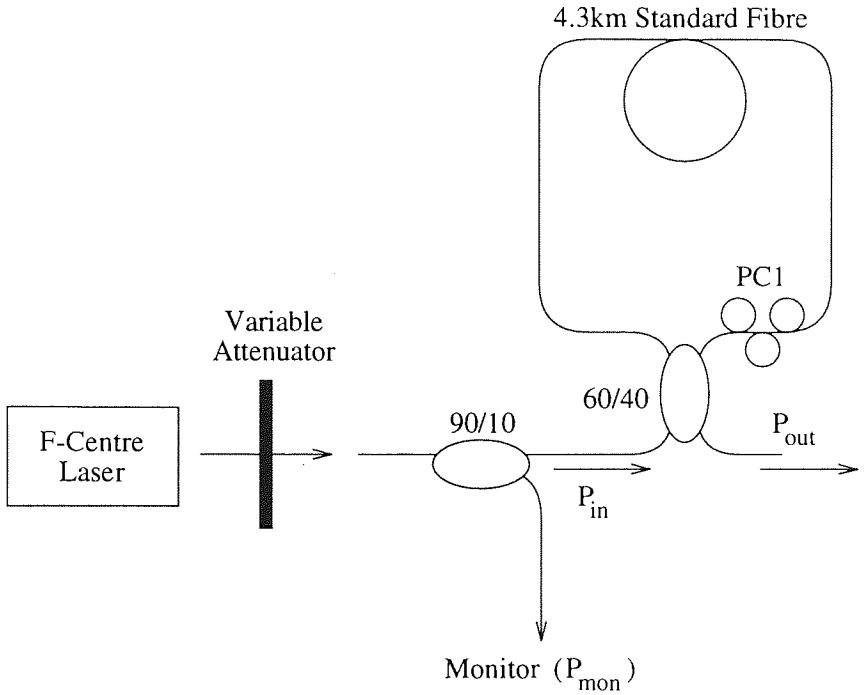

Figure 2.8: Schematic of experimental configuration for characterisation of an asymmetric-coupler NOLM.

A schematic of the experimental configuration used to characterise the NOLM is shown in fig. 2.8. 7ps (full-width-half-maximum) pulses at 1549.2nm from the same F-centre laser were launched into the NOLM via a 90/10 coupler. The 10% port of the coupler was then used as a monitor of the input pulse spectrum and average power (P_{mon}). Input power control (variable attenuator) was obtained using a chopper. The NOLM was constructed using a 60/40 ($\alpha = 0.4$) fused-fibre coupler with its ends joined by a 4.3km length of standard fibre (Dispersion=17ps/(nm.km) at 1550nm). The quoted fibre loss was 0.19dB/km. Doran and Wood [19] have shown that pulses with shapes and energies close to the values required to form a soliton in a length of fibre display the essential characteristics of these pulses when allowed to evolve over a sufficient fibre length. For this evolution to occur in a NOLM, the loop length must be a few soliton periods long.

The soliton period, z_0, *i.e.* the distance which a pulse must travel to accumulate a nonlinear phase of $\pi/4$ is given by the equation,

$$z_0 = 0.322\frac{c\pi^2\tau^2}{\lambda^2|D|} \tag{2.9}$$

where c is the speed of light in vacuum, τ is the full-width-half-maximum pulse width, λ is the optical wavelength and $|D|$ is the magnitude of the fibre dispersion. For the experimental parameters quoted, the calculated soliton period is $z_0 =$ 1.1km. Thus, the chosen loop length of 4.3km corresponds to a length of $4z_0$. The soliton power for a given soliton order is given by,

$$P_0 = \frac{N^2\lambda A_{eff}}{4n_2 z_0} \tag{2.10}$$

where N is the soliton order. The peak power for an N=1 soliton in this configuration is 1.2W which is equivalent to an average power, at a repetition rate of 76MHz with 7ps pulses, of 0.6mW. The polarisation controller, PC1, was included to provide a means of biasing the NOLM into reflection as described in section 2.2. The insertion loss of the device, a value which consists of contributions from fibre loss and coupler insertion loss, was measured with the NOLM biased into linear transmission and the input power reduced to a level at which nonlinear effects were negligible and was found to be 0.9dB.

Figure 2.9 (i) shows an autocorrelation and sech^2 fit of the F-centre laser pulses launched into the NOLM, and 2.9 (ii) the corresponding spectrum. The time-bandwidth product of 0.36, compared with a value for an exact soliton of 0.315, suggests that these pulses are slightly chirped. However, the difficulty in distinguishing the autocorrelation from its sech^2 fit shows that they are close to perfect soliton pulses and may, therefore, be expected to closely follow soliton behaviour in the fibre.

With the NOLM biased into reflection and the chopper on, the transmission characteristic of the device was recorded using two medium area photodetectors: one recording P_{mon} and, hence, giving a measure of the input power; and the other recording P_{out}. The outputs from these detectors were then viewed on a Gould 1600 digitizing oscilloscope which was triggered at the chopper frequency. Using this technique, the input and output traces could be recorded for a single

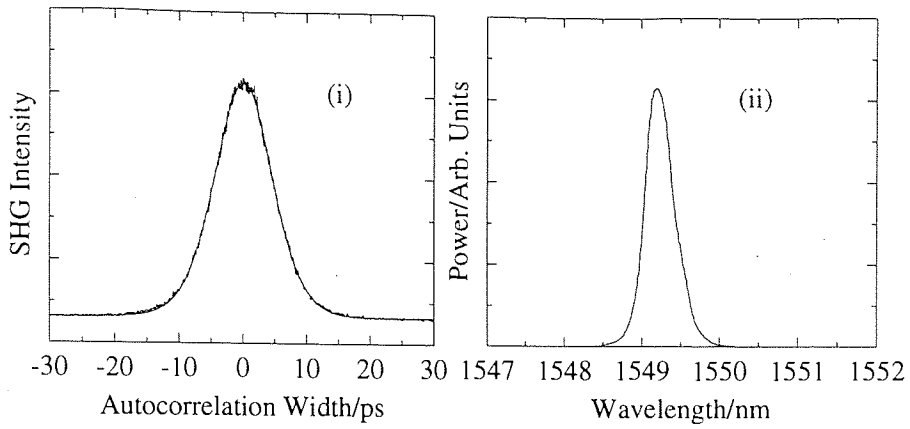

Figure 2.9: F-centre laser input pulses. (i) Autocorrelation and sech^2 fit. $\Delta\tau$ =7ps. (ii) Spectrum. $\Delta\lambda$ =0.41nm, $\Delta\nu\Delta\tau$ =0.36.

triggered sweep, providing a means of analysing the time-averaged transmission characteristic of the device. An additional benefit of the technique is that it also enables real-time optimisation of the switching response. Figure 2.10 (i) shows a typical transmission characteristic for this NOLM. The first and second peaks occur at average input powers (soliton order) of 2.2mW (N=1.95) and 5.1 mW (N=2.96) respectively, with corresponding peak transmissions of 66% and 63%. The first and second minima occur at input powers (soliton number) of 3.1mW (N=2.31) and 4.8mW (N=3.16) with extinction ratios of 9.7dB at the first minimum and 6.5dB at the second minimum. Figure 2.10 (ii) shows the switching response predicted by numerical simulation using the experimental parameters. The NOLM is modelled by separately solving the NLSE for each of the counter-propagating components using the well-known split-step fourier technique [31]. Predicted first and second peak input powers (soliton order) are 1.7mW (N=1.71) and 3.7mW (N=2.52) with peak transmissions of 81% and 78% respectively. The predicted first and second minima occur at input powers (soliton order) of 2.5mW (N=2.07) and 4.1mW (N=2.66) with respective extinction ratios of 13.6dB and 6.4dB. It is clear from qualitative examination that there is good agreement between the experimental and numerical respsonse profiles, but that there exists a consistent discrepancy between the switching powers at each of the features listed above. This is most likely due to an experimental coupling ratio, α, of greater than 0.4; the measured switching power at the first peak being consistent with a splitting ratio of 0.43.

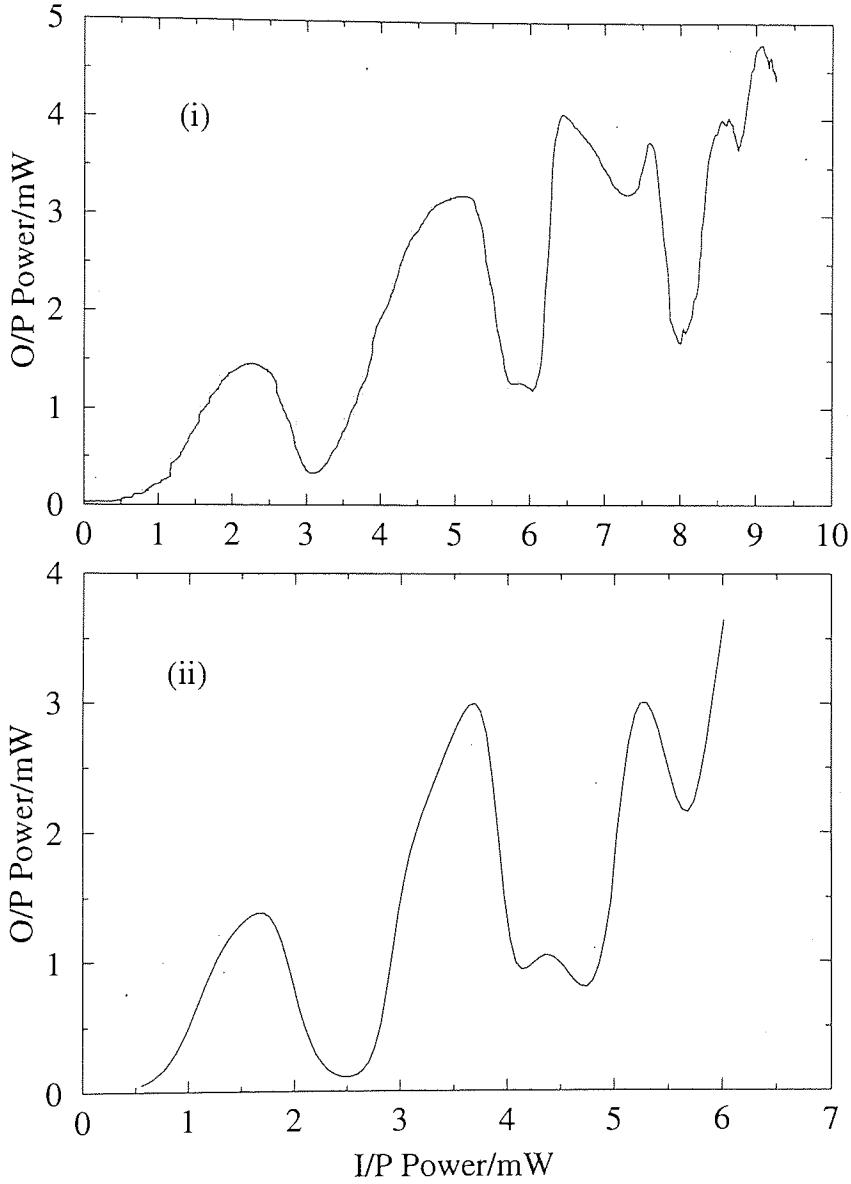

Figure 2.10: (i) Experimental time-averaged transmission characteristic for 4.3km standard fibre NOLM. (ii) Time averaged response predicted by numerical simulation.

As already mentioned, maintenance of the spectral and temporal integrity of pulses is a prime requirement for any device. Figures 2.11 and 2.12 summarise experimental measurements of output pulse autocorrelations and spectra respectively at various points along the NOLM switching characteristic. Also shown are the results predicted by the numerical model for the same points.

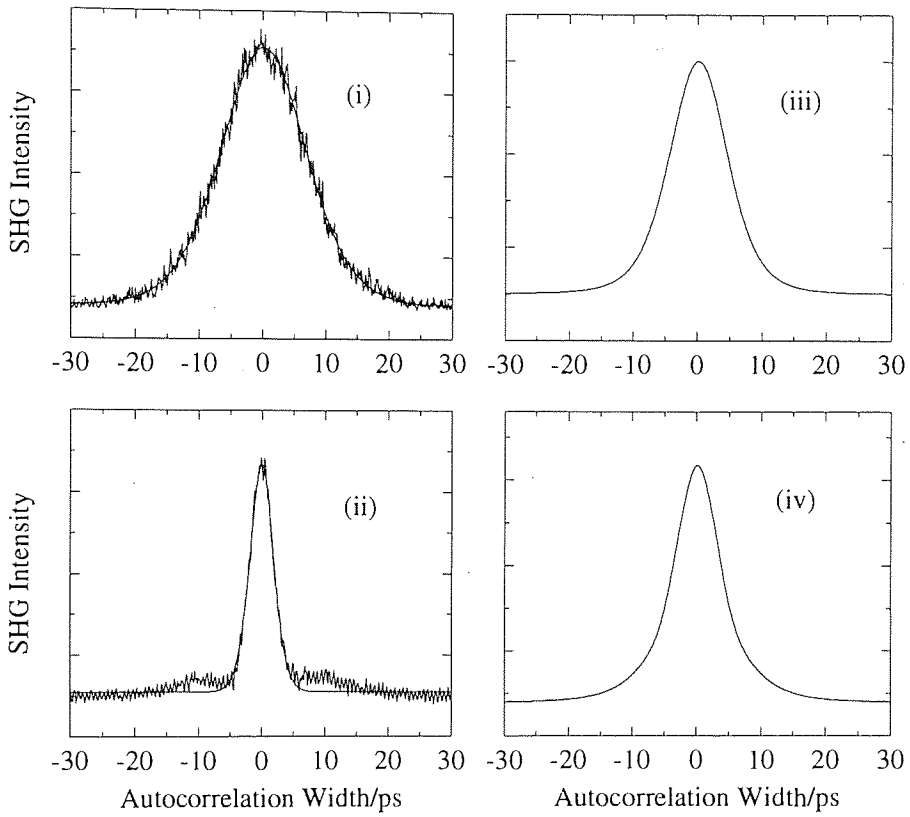

Figure 2.11: Experimental autocorrelation and sech^2 fit for emerging pulse at (i) first peak. $\Delta\tau$ =10.3ps, P_{in} = 2.2mW. (ii) second peak. $\Delta\tau$ =2.8ps, P_{in} = 4.8mW. Predicted autocorrelation at (iii) first peak. $\Delta\tau$ =7ps, P_{in} = 1.7mW. (iv) second peak. $\Delta\tau$ =3.9ps, P_{in} = 3.7mW.

Taking the results at the first switching peak, it can be seen that the output pulse width has increased by a factor of almost 50% to 10.3ps compared with an input pulse width of 7ps (fig 2.11 (i)), and that the time-bandwidth product has risen from 0.36 to 0.37. This increase is probably due a combination of fibre loss, which leads to an increase in pulse width as $e^{-2\Gamma z}$ as discussed in chapter 1, and soliton self-adjustment to intial chirp. It has been shown [27] that a pulse of the intial form Asech(t) where A is not an integer, separates into soliton and noise components which evolve as the phase of the underlying soliton towards

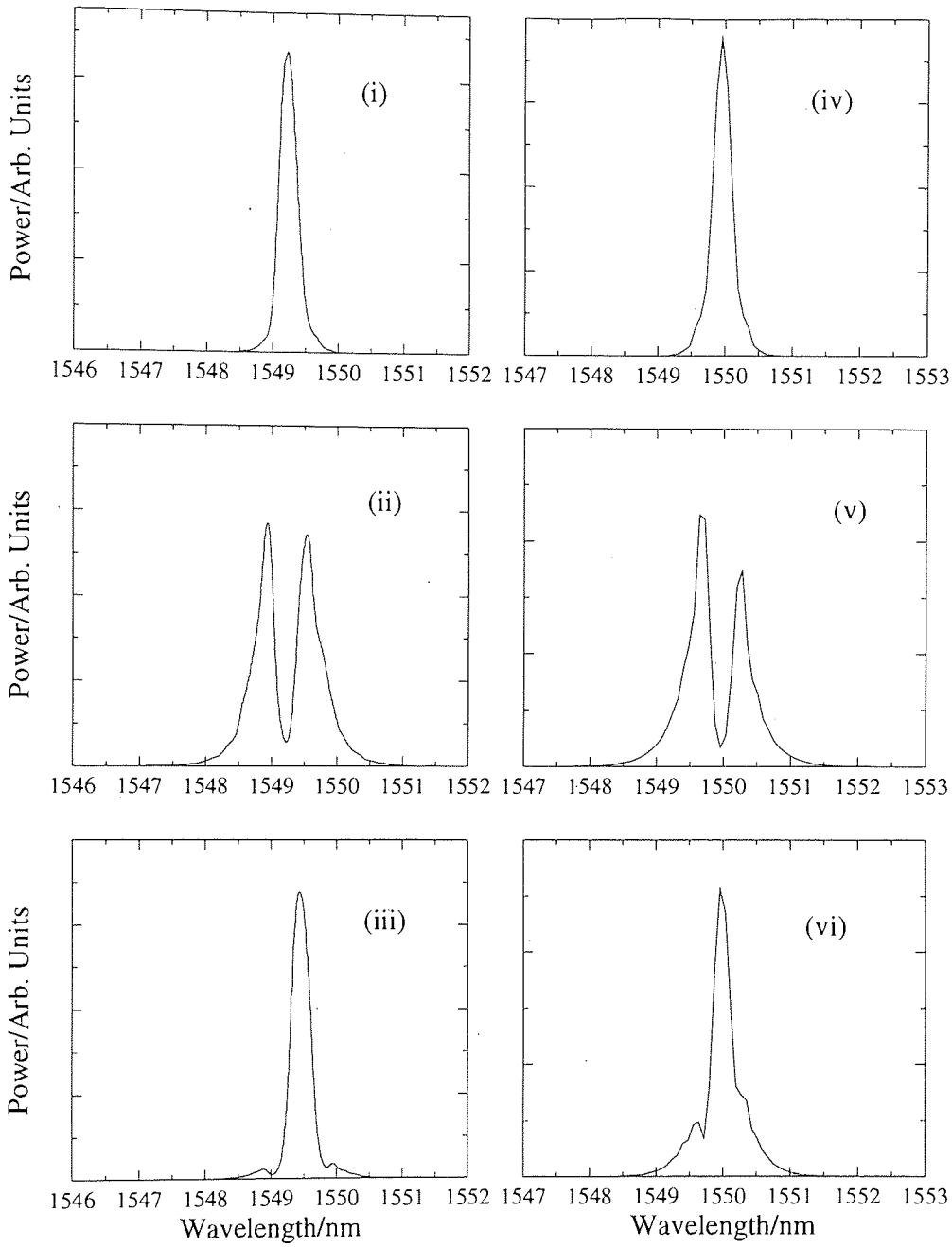

Figure 2.12: Experimental output pulse spectrum (i) at first peak. $\Delta\lambda$ =0.29nm, $\Delta\nu\Delta\tau$ =0.37, P_{in} = 2.2mW. (ii) just beyond first minimum. P_{in} = 3mW. (iii) at second peak. $\Delta\lambda$ =0.31nm, $\Delta\nu\Delta\tau$ =0.11, P_{in} = 4.8mW. Predicted output pulse spectrum at (iv) first peak. $\Delta\lambda$ =0.35nm, $\Delta\nu\Delta\tau$ =0.31, P_{in} = 1.7mW. (v) just beyond first minimum. P_{in} = 2.8mW. (vi) at second peak. $\Delta\lambda$ =0.25nm, $\Delta\nu\Delta\tau$ =0.12, P_{in} = 3.7mW.

a final pulse width which is dependent on the initial pulse amplitude. In an analagous manner, an initially chirped pulse splits into a soliton component and a dispersive tail [67] giving a final pulse width which is always greater than the initial value. Thus, since the NOLM is inherently lossy, and launched pulses are slightly chirped ($\Delta\nu\Delta\tau$ =0.36), the increase in pulse width may not be entirely surprising. It should be noted that, although the pulse is not an exact temporal replica of the input, nevertheless, the essential soliton character of the input pulse train is not significantly degraded as evidenced by the only marginal increase in time-bandwidth product.

The imperfect nature of the experimental pulse train probably also accounts for the discrepancy between the measured pulse width at the first peak and that predicted by the numerical model (fig. 2.11 (iii)) of 7ps. The simulation is based on an input train of perfect transform-limited solitons and demonstrates that such pulses pass through the device without degradation. The predicted time-bandwidth product in this case, using fig 2.12 (iv), is 0.31. Thus, it is clear that pulses emerging on the first peak of the NOLM switching response retain their soliton characteristics receiving, at best, no degradation in the case of a perfect soliton train, and minimal degradation in the chirped pulse case. Thus, the device leaves pulses suitable for further processing.

Figure 2.11 (ii) shows an autocorrelation and $sech^2$ fit for pulses emerging on the second peak of the NOLM switching characteristic and 2.12 (iii) shows the corresponding spectrum. The measured pulse width in this case was 2.8ps with a time-bandwidth product, $\Delta\nu\Delta\tau$, of 0.12. The corresponding numerical results are shown in figures 2.11 (iv) and 2.12 (vi). The predicted pulse width is 3.9ps with a time-bandwidth product of 0.11. As before, the discrepancy between the predicted and measured pulse widths and time-bandwidth products is probably due to the small degree of chirp present on the input pulse train. It can be seen from the side-lobes present on the measured autocorrelation and from the 60% reduction in pulse width that the characteristics of emerging pulses at this point are significantly degraded. Since the pulses propagating in each arm of the device have soliton orders of 1.95 and 1.59 at this input power, this reshaping is most likely due to higher-order pulse evolution. The accompanying degradation in pulse quality, therefore, limits the usefulness of this portion of the characteristic.

Also shown in fig. 2.12 (ii) and (v) are the measured and predicted spectra

at an input power of 3mW. The corresponding autocorrelation is not shown due to the lower output power from the NOLM at this point. When the progressions of measured and predicted spectra in fig. 2.12 and autocorrelations in fig. 2.11 are examined qualitatively as a whole, it is clear that there is extremely close correspondence between the experimental and numerical results even though the experimental pulse parameters are non-exact solitons. Thus, another advantage of soliton switching systems is highlighted, namely the ease and accuracy with which they can be modelled.

2.5 Analysis of the Influence of Intrapulse Raman Generation on Device Switching Response

As mentioned in the introduction to this chapter, the switching response shown in fig. 2.10 is a first-time demonstration of multiple-peaked switching in a NOLM, and is a consequence of the relatively long pulse width chosen to perform the characterisation [55], which results in postponement of the onset intrapulse Raman generation. This section provides a study of the influence of intrapulse Raman generation on operation of the NOLM, presenting results from a series of numerical simulations which chart the gradual degradation of the switching characteristic with incident pulse width.

2.5.1 Raman Generation and Device Failure

As discussed in chapter 1, Raman generation is a nonlinear process by which energy from a propagating wave is transferred into the frequency down-shifted Stokes wave. In soliton systems, self-Raman generation, in which optical energy is fed from short to long wavelength components of the pulse spectrum, leads to soliton self-frequeny shift and higher order soliton decay. Both of these phenomena have implications for the NOLM. Firstly, since the rate of growth of the Stokes wave increases with the pump signal power, it follows that counter-propagating pulses of unequal amplitude will frequency-shift by different amounts while propagating through the fibre loop. When combined with fibre dispersion, this frequency shift gives rise to a mismatch in arrival time and leads eventually to imperfect or no interference at the coupler, break-down which also occurs with

soliton decay. The first demonstration of NOLM switching by Blow *et. al.* [54] used pulse widths of 417fs and characterised operation of the device only as far as the first switching minimum. However, the demonstration of Islam *et. al.* [41] with 310fs pulses, showed that, for pulses this short, no more peaks could be obtained beyond this minimum anyway due the impact of the inherently strong Raman-induced interference degradation detailed above. By choosing relatively long pulse widths of 7ps with a much narrower spectral content these effects have been reduced, and, as a consequence, the operating region of the device has clearly been extended. It was noted that the increased loop length resulting from the choice of these longer pulses was not found to significantly impair the environmental stability of the NOLM over the region shown in fig. 2.10, and polarisation bias was maintained for periods of a few hours.

Features observed beyond the range shown were found to be extremely unstable. Analysis of spectra and autocorrelations of the NOLM output for higher power showed that this instability is due to Raman generation. Figure 2.13 (i) shows the output pulse spectrum obtained for an input power of 7mW (N=3.5). The long-wavelength tail present on the spectrum indicates the onset of SSFS.

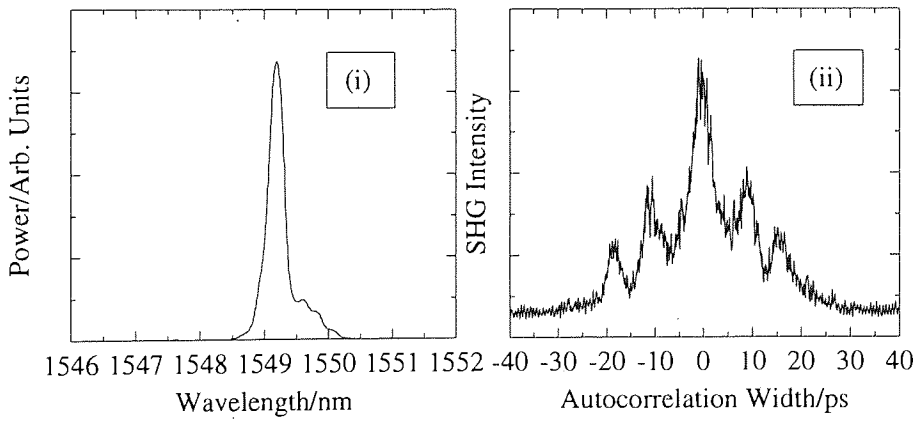

Figure 2.13: (i) Spectrum of output pulses for an input power of 7mW. (ii) Autocorrelation of output pulses for an input power of 12mW.

Figure 2.13 (ii) shows an autocorrelation of the output pulse train at an input power of 12mW (N=4.54). The five peaked autocorrelation indicates that the output consists of three separate pulses. Since the counter-propagating pulses correspond initially to third order solitons (N=3.5 and N=2.9), it is likely that this autocorrelation is indicative of the decay of each into its constituent sin-

gle solitons. Thus, it is clear that the intrapulse Raman effects which occur much earlier in the switching characteristic for sub-picosecond pulse widths are postponed. The presence of these effects also accounts for the instability of the switching mentioned above and it can be concluded that it is, therefore, a product of source amplitude fluctuations coupled with the high sensitivity of higher order pulses to variations in launched power.

2.5.2 Variation of Extent of Switching With Incident Pulse Width

From the foregoing discussion, it is apparent that intrapulse Raman generation places a fundamental constraint on the extent of the NOLM operating region. The current section presents results from a series of numerical simulations which plot the predicted switching characteristic over a range of input pulse widths and, thus, varying strengths of Raman generation. Figure 2.14 shows the results for a selection of the input pulse widths used *i.e.* τ=6ps, τ=4ps, τ=2ps, τ=1.5ps, τ=1ps and τ=0.5ps. The simulations were carried out using the experimental parameters: λ =1550nm, fibre dispersion=17ps/(nm.km), A_{eff} =88μm^2 , α =0.4 and L= $4z_0$.

It can be seen, in agreement with the findings of this study and those of previous experiments [54, 41], that the shape of the first switching peak is relatively insensitive to pulse width. Thus, even at pulse widths as low as 500fs, the effects of intrapulse Raman generation are not sufficient to degrade interference at the coupler in this region of the switching characteristic. However, the progression shows that features beyond the second switching peak become increasingly affected by this limitation as pulse width is reduced, and from the work of Islam [41], it is apparent that further reduction in incident pulse width results in the second peak itself being "washed out". Figure 2.15 shows a plot of the depth of the second switching minimum predicted by these numerical simulations against input pulse width . The curve provided is an empirically calculated fifth order polynomial fit to provide a guide to the eye. It is apparent that, for pulse widths in excess of 4ps, the curve approaches an asymptotic extinction ratio as pulse width is increased. It is probable then that, with the use of even longer pulses, device operation may be extended further. However, higher order soliton shaping within the device as well as decreased environmental instability due to the long loop lengths required are likely to make the device of limited use. This

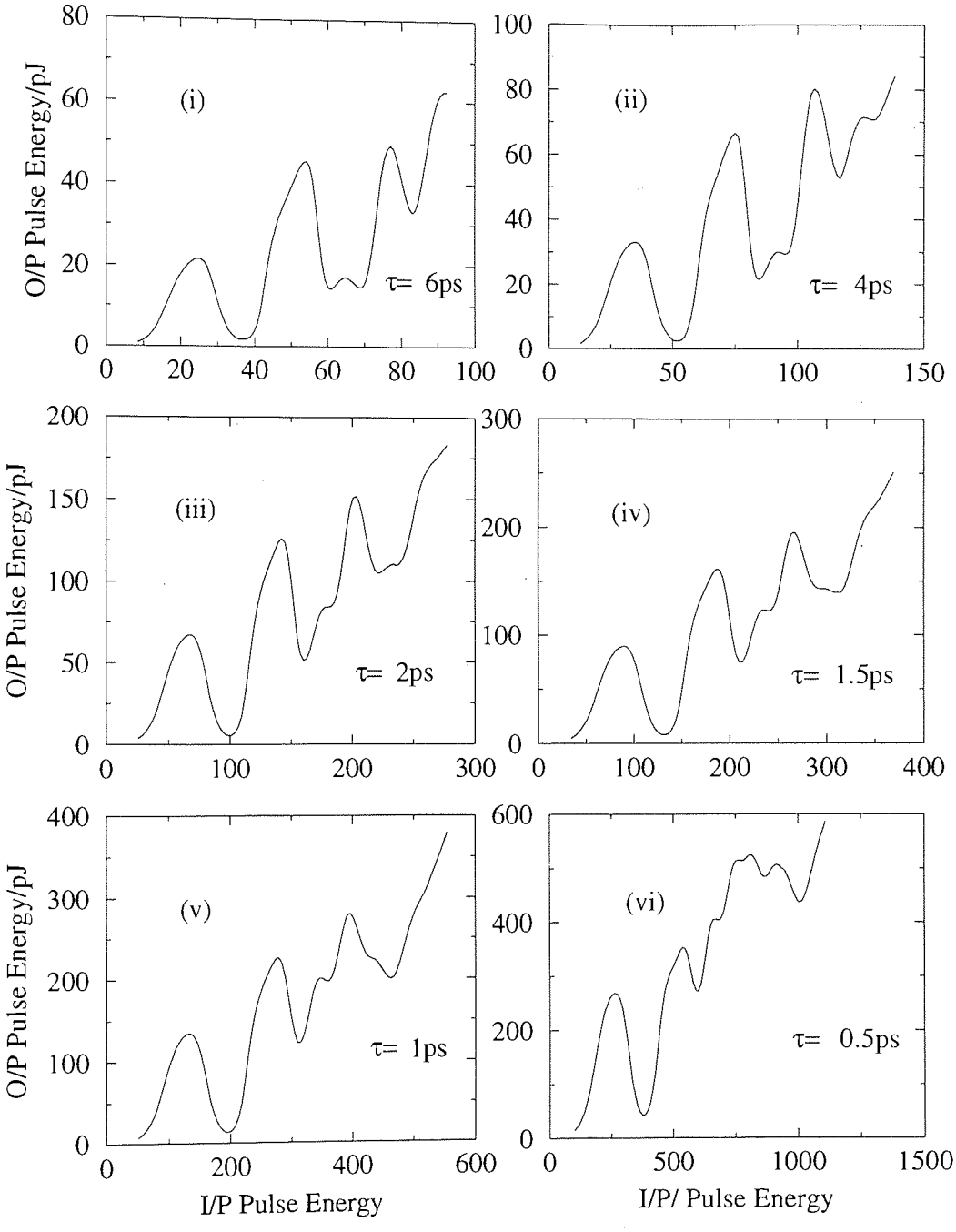

Figure 2.14: Predicted switching curve for transform-limited solitons of pulse width (i) 6ps, (ii) 4ps, (iii) 2ps, (iv) 1.5ps, (v) 1ps and (vi) 0.5ps.

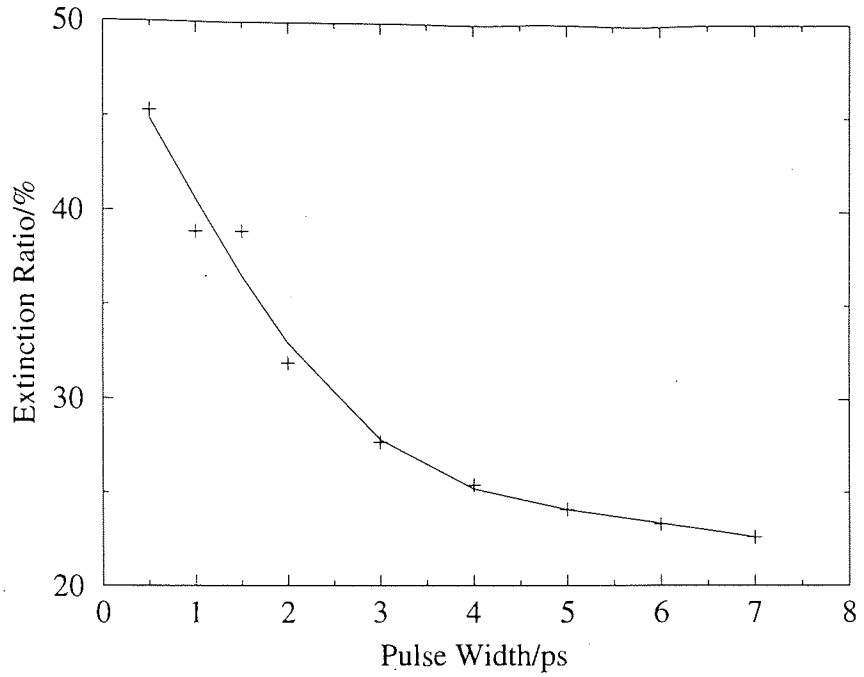

Figure 2.15: Plot of extinction ratio at the second minimum against input pulse width for a $4z_0$ NOLM.

asymptotic relationship suggests that the shape of the switching profile at this point is probably unlikely to be significantly altered for pulse widths greater than 7ps.

2.6 Conclusion

In conclusion, this chapter has introduced the concepts governing the operation of an alternative device to those presented in Chapter 1, namely the nonlinear-optical loop mirror (NOLM). The fibre loop mirror, the device from which the NOLM is largely derived, was described and it was shown that by the introduction of a differential phase shift of π between the counter-propagating optical fields, the input signal could be switched between 100% reflection and 100% transmission.

It has been shown that by exploiting the nonlinear dependence of refractive index in glass this switching condition can be met by fabricating the device using an unbalanced fused-fibre coupler. In this form the propagating fields, having different optical powers, acquire a differential phase shift with the result that the transmission behaviour of the mirror becomes intensity dependent.

The benefits of the use of the soliton as a data carrier were then outlined. The soliton combines a number of properties which make it ideal as the subject of nonlinear fibre switching. Firstly, since the phase of the pulse is constant across its intensity envelope, interference of two pulses of equal width results in no change in the temporal profile. Secondly, since the phase accumulated by a pulse is dependent on its peak power, the potential for differential nonlinear phase accumulation is evident. Thirdly, if the temporal and spectral integrity of the input pulse is corrupt so that a non-exact "soliton-like" pulse is introduced into the arms of the device, the underlying soliton character will evolve out in the course of propagation, and the switching characteristic is not degraded.

Results from an experimental investigation of soliton switching using 7ps sech^2 pulses were then presented. It was seen that pulses emerging from the device largely retained their soliton characteristics with only minimal change to the pulse temporal and spectral profile. The reshaping encountered (the pulse width at the output increased by a factor of 50% to 10.3ps) is due to self-adjustment of pulses launched into the device for initial chirp.

Results were then presented demonstrating, for the first time, a multiple-peaked switching response in a NOLM. This extension of the characteristic was shown to be due to the reduction of intrapulse Raman generation as a result of the narrower spectral content and reduced peak powers inherent in the use of relatively long pulses. Numerical results were then presented tracing the effect of pulse width on the extent of switching. It was found that for pulse widths as low as 500fs, switching at the first peak is not significantly degraded, while the second switching peak, and features beyond, became gradually less distinct and were eventually destroyed completely. By plotting the extinction ratio at the second minimum against pulse width, an asymptotic relationship was revealed for increasing pulse width, suggesting that no significant change in the quality of the response at the second peak of the profile would occur for pulse widths greater that those used in the experiment.

Finally the advantages of the NOLM over the devices presented in chapter 1 were presented. The simplicity of construction, insensitivity to input polarisation, low switching threshold, increased environmental stability, a result of its inherently balanced interferometer configuration, give the NOLM significant advantages as a primitive component in nonlinear switching architectures. Specif-

ically, since device operation is independent of input polarisation and emerging pulses retain their temporal and spectral soliton characteristics, the device is eminently cascadeable, a primary requirement for any primitive data processing element. It is this property which is the subject of the next chapter.

Chapter 3

Enhancement of Amplitude and Spectral Response By Device Concatenation

3.1 Introduction

Since serial and parallel device concatenation is central to the construction of switching systems with levels of functionality above their constituent components, the need to demonstrate device cascadability has long been recognised [18, 43]. As the output of an architecture is essentially a functional combination of a number of primitive processing operations, the underlying design consists of a network of modules which alter information from, and pass it on to, the neighbours to which they are connected. A primary requirement for every primitive processing element within such an architecture, therefore, is that it maintain the spectral and temporal integrity of the incoming data leaving it uncorrupted and suitable for further manipulation. Application of this fundamental concept has led to experimental demonstrations of a number of multi-device all-optical systems from simple logic functions [68, 45] through to systems performing operations as complex as all-optical signal regeneration, [69], all-optical channel demultiplexing [70] and memory [71].

This chapter presents results from experiments which apply this basic concept to enhance two particular aspects of NOLM performance: amplitude response and wavelength response.

3.2 Enhancement of Amplitude Response by Device Cascading

3.2.1 Introduction

The benefits to be gained from device concatenation for the CW amplitude response of all-optical switching devices are already established [60, 51, 63, 72].

Concatenation leads to a sharpening of the overall switching characteristic resulting in steeper switching edges, flatter switching peaks and enhanced inter-peak extinction ratios. The primary impact of this "squaring-off" of the characteristic for digital processing is that it enhances the amplitude discrimination of a configuration between, and at the edges of the switching maxima, while decreasing the sensitivity of the output power to small-scale fluctuations in input power at the central regions of the peaks giving rise to an increase in immunity to noise.

The CW response of a cascade of two, self-switched, asymmetric coupler NOLM's has been investigated both numerically and experimentally [63, 72] by analysing the transmission of pulses in the normal dispersion regime from a mode-locked Nd:YAG laser. In this switching regime, sharpening of the device response has been shown to lead to an enhancement of the pulse reshaping inherent in single NOLM switching, a property which was identified in chapter 2. Consequently, pulses emerging from this cascade were shown to have square temporal profiles [72], a phenomenon which, if also found to occur in the soliton regime, would severely limit application of the NOLM in higher level systems. For solitons, therefore, it is not sufficient to restrict evaluation of the impact of concatenation to just the time-averaged response; its effect on the temporal and spectral characteristics of the input soliton pulse train must also be addressed. It is this fuller characterisation which is the subject of the current chapter. An incidental benefit of such an analysis is that it provides a test of the thesis, proposed in the previous chapter, that soliton pulses emerging from a NOLM may be subjected to further manipulation, since their essential temporal and spectral characteristics are retained.

Results from two experimental investigations are presented. Since the output characteristics beyond the first peaks become strongly influenced by self Raman generation and higher order pulse shaping, both sets of experiments are largely centred on analysis of the first peaks of the resulting output characteristics. The first uses a single-NOLM setup and is largely based on the configuration used for the CW investigation of ref. [72] in which concatenation is achieved by feedback of the nonlinearly transmitted signal. From this analysis, it is found that the primary design consideration for optimal concatenated switching is loss; the combination of fibre loss, coupler insertion loss and feedback-path return loss in this configuration is found to severely degrade the time-averaged response due

to power mismatch between the return signal and the first switching peak of the NOLM. As a result, a model is developed for a true cascade of two NOLM's which predicts the fibre lengths required to optimise the cascade switching profile.

The experimental parameters required to accurately match the input power at the first switching peak of the second NOLM to the output power of the first are calculated by taking the output of the first NOLM as a starting point for the model. The first experimental configuration is then modified to consist of a true two-NOLM cascade with these predicted "optimal" parameters. Results from experimental investigation of this optimal cascade lead to three main conclusions. Firstly, the enhancement of the switching response as a consequence of cascading, already known to occur in the CW case, also occurs in the soliton regime. Secondly, and crucially, the sharpening of the switching profile is not accompanied by a significant degradation in the temporal profile of the emerging pulses, which largely retain their underlying soliton characteristics. Finally, the pulses emerging from a single NOLM are, indeed, rendered capable of further processing vindicating the conclusions of the previous chapter. Thus, the results of chapter 2 may be extended to apply to a sequence of NOLM's providing further support, firstly, for the conclusion that the NOLM has marked advantages as a building block in soliton switching systems and secondly, that the robustness of the soliton makes it a data carrier which is well-suited to nonlinear fibre switching.

3.2.2 Single NOLM With Feedback

A schematic of the experimental configuration is shown in fig. 3.1. The setup consists of a double-pass configuration in which the first-pass nonlinearly transmitted signal is fed back through the NOLM after reflection from the mirror M1 against which a cleaved end is butted. 7ps pulses at a repetition rate of 76MHz from the same tunable, modelocked F-centre laser used in the single NOLM characterisation of chapter 2 were launched into the NOLM via a 52/48 coupler as shown. The NOLM was again constructed using a 60/40 (α=0.4) fused-fibre coupler and 4.3km of standard telecommunications fibre (STF), corresponding to a length of $4z_0$ for the input pulses.

The first part of the experimental procedure involves orientation of the relative polarisations of the signal reflected by the NOLM on the first pass through the device, and the twice nonlinearly-transmitted (double-pass) signal so that they

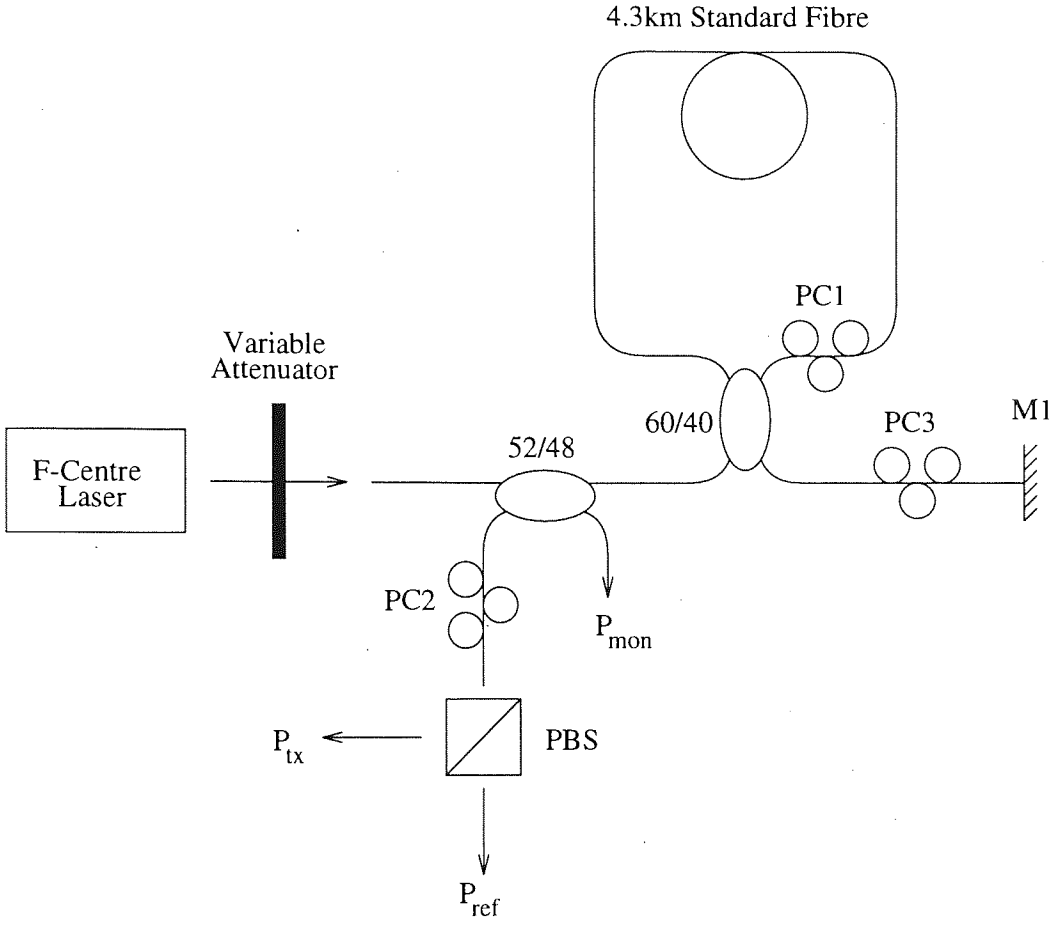

Figure 3.1: Schematic of double-pass configuration for investigation of NOLM concatenation. PBS, polarising beam splitter.

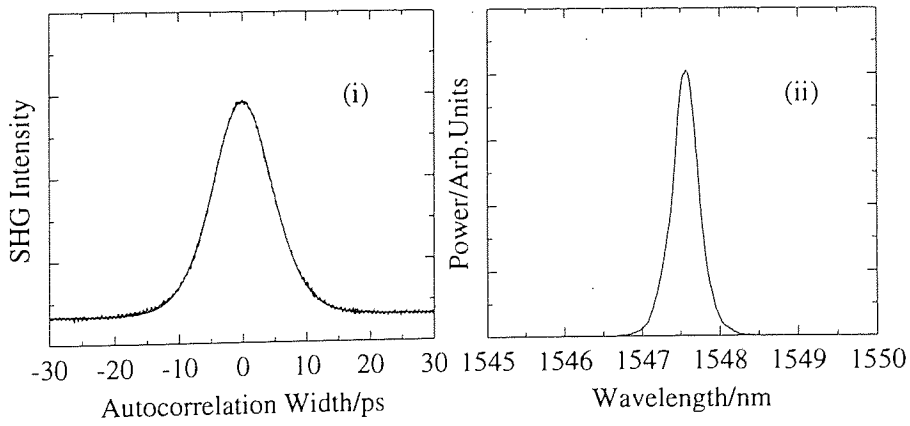

Figure 3.2: F-centre laser input pulses. (i) Autocorrelation and sech^2 fit. $\Delta\tau$ =7.1ps. (ii) Spectrum. λ = 1547.5nm, $\Delta\lambda$ =0.37nm, $\Delta\nu\Delta\tau$ =0.33.

may be separated using the polarising beam splitter (PBS). The procedure is as follows. While monitoring P_{ref} with a power meter, and with the input power reduced to a level at which nonlinear effects were negligible, the NOLM was biased into linear reflection using PC1. The polarisation of the reflected signal was then oriented by adjustment of PC2 to maximise P_{ref}. Next, the input power was increased to produce nonlinear transmission and P_{tx} was maximised using PC3. At the point at which P_{tx} is a maximum, the double-pass nonlinearly transmitted signal is linearly polarised in the plane orthogonal to the first-pass reflected signal. The insertion loss of the configuration, which was measured to be 3.1dB, was obtained by biasing the NOLM into linear transmission and recording P_{ref} at a low input signal power.

Figure 3.2 (i) shows an autocorrelation and sech^2 fit of the incident pulses from the F-centre laser, and fig. 3.2 (ii) the corresponding spectrum. The pulses were centred at a wavelength of 1547.5nm with a full-width-half-maximum width, in this case, of 7.1ps and a time-bandwidth product, $\Delta\nu\Delta\tau$, of 0.33. Thus, as before, the launched pulses were slightly chirped, and again could be expected to broaden marginally due to self-adjustment and adiabiatic broadening due to loss.

The double-pass nonlinear transmission characteristic was viewed using the Gould digitizing oscilloscope by simultaneously monitoring P_{mon} (input power) and P_{tx}, again, using a trigger derived from the chopper. A summary of the time-averaged results is shown in fig. 3.3.

Figure 3.3 (i) shows the nonlinearly transmitted signal on the first pass, and fig. 3.3 (ii) the double-pass characteristic. The first and second peaks of the double-pass response occur at input powers (soliton order) of 2.1mW (N=1.9) and 4.6mW (N=2.81) with corresponding peak transmissions of 14% and 26% respectively. Figure 3.3 (iii) shows the the double-pass characteristic predicted by numerical simulation. The first and second major peaks occur at input powers (soliton order) of 1.8mW (N=1.76) and 4mW (N=2.62) with peak transmissions of 60% and 44%. Unlike the single NOLM analysis, there is significant disagreement between the predicted and measured responses. It is clear that the profiles differ markedly in shape and that the total measured transmitted power at each peak is significantly lower than predicted, indicating that the discrepancies are probably loss-induced.

Characterising the primary sources of loss, there is, firstly, 0.8dB of fibre loss

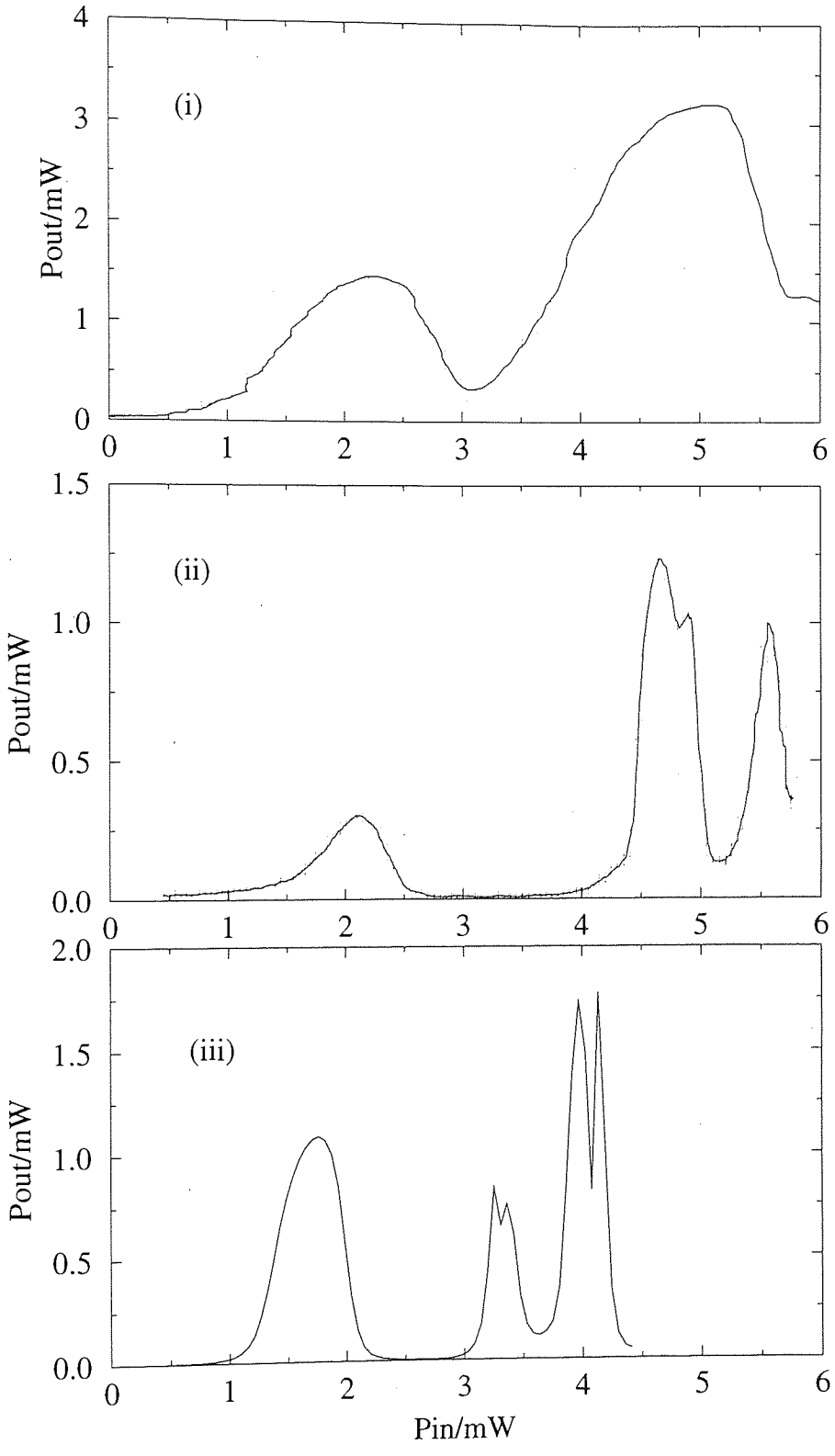

Figure 3.3: Experimentally determined time-averaged response for (i) single pass through NOLM. (ii) double pass through NOLM. (iii) Time-averaged response predicted by numerical simulation.

due to the 4.3km of STF which constitutes the loop, and a further effective loss of 0.8dB due to the peak transmission level of 82%. Secondly, there is the impact of loss in the feedback arm. Knowing the insertion loss of the NOLM, *i.e.* loss due simply to fibre loss and coupler insertion loss, which was measured to be ~0.8dB, this contribution can be evaluated by biasing the NOLM into linear transmission and measuring the twice-transmitted power with a low level input signal. This gave an excess loss due to feedback of 0.7dB. A rough estimate of the output from the NOLM when this excess loss is taken into account may be obtained by calculating the power now launched back into the device. After application of this feedback loss to the output power of the device at the first peak, measured from fig. 3.3 (i), of 1.4mW the signal power launched into the NOLM on the second pass is found to be 1.2mW. This is only 55% of the switching power level of the device and leads to a significantly reduced output power on the second pass, again using the transmission characteristic of fig. 3.3 (i), of around 0.5mW. Thus, even from this approximate evaluation of the effect of loss on the switching profile, it can be seen that if optimal operation of a device sequence is to be achieved, the input switching power level of the second device must match the output power of the first.

Figure 3.4 provides a summary of a more systematic numerical study of the effect of excess loss, obtained by modeling loss sources other than that of fibre loss as a single lumped loss element between the devices. Values of excess loss chosen were 0.4dB, 0.8dB, 1dB, 1.2dB, 1.6dB and 2dB as shown. It is clear that the curves for excess loss levels of 1dB and 1.2dB closely resemble the experimental characteristic both in profile and transmitted power, which is reasonably consistent with the measured feedback arm loss.

The results of this demonstration show that loss must be taken into consideration if correct operation of a device cascade is to be achieved. It is clear that the second NOLM must be designed to anticipate a reduced launched power level due to both fibre loss and insertion loss of other devices. In the next section a variation of the numerical loss analysis summarised in fig. 3.4 is presented. A simplified analysis is developed which enables accurate prediction of the experimental parameters of an optimally designed true two-NOLM sequence.

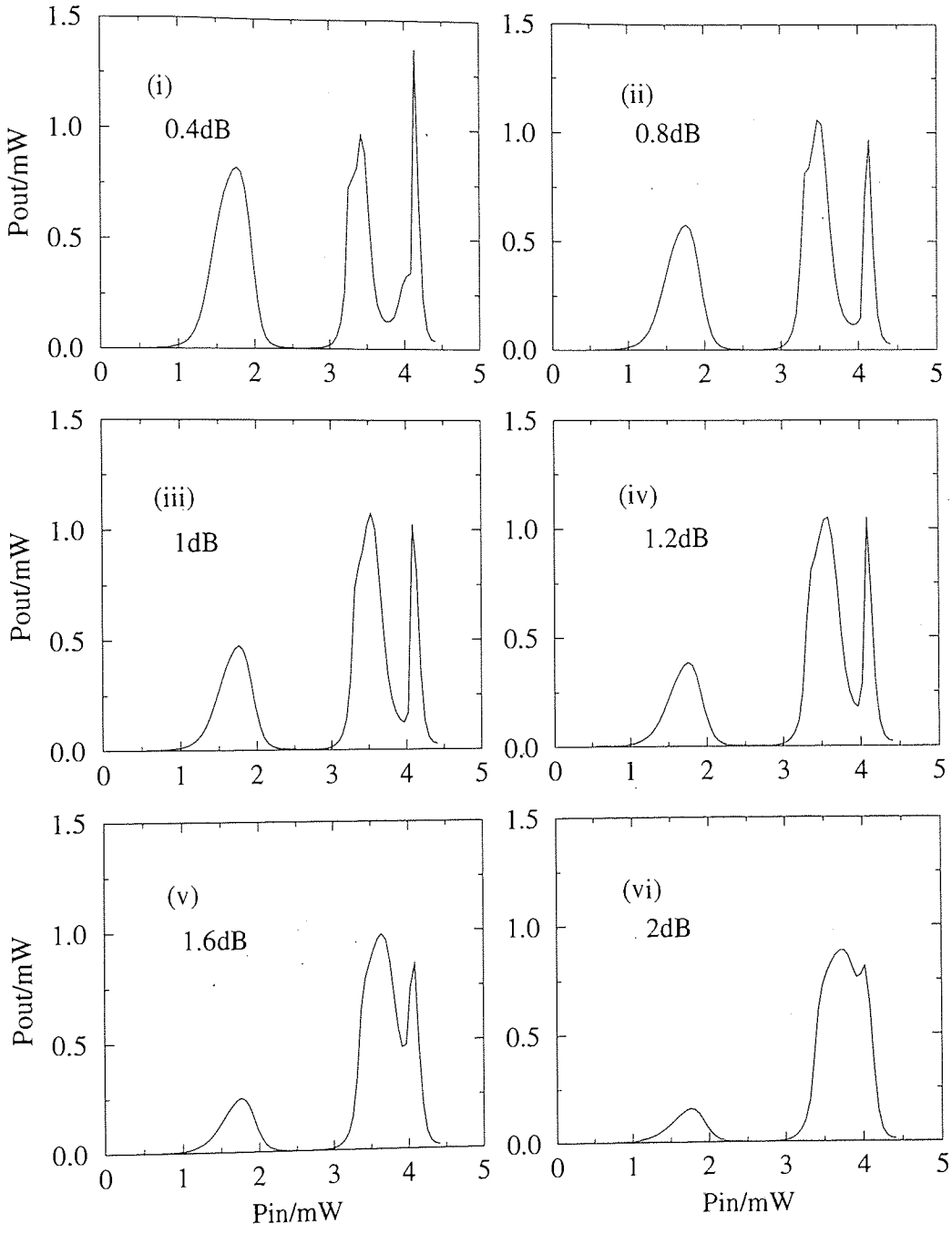

Figure 3.4: Predicted double pass switching curves for excess loss levels of (i) 0.4dB, (ii) 0.8dB, (iii) 1dB, (iv) 1.2dB, (v) 1.6dB and (vi) 2dB.

3.2.3 *Optimised Two-Device Cascade*

Prediction of the optimum experimental parameters was performed by application of the soliton phase model which provides a simple analytical formula relating the transmission characteristic of a NOLM to its input power. As already discussed, the phase of a pulse with a profile of the form Asech(t) evolves as the phase of the underlying soliton. For a pulse of this form, this phase is given by [54, 16],

$$\phi_s = \begin{cases} 2(A-1/2)^2 L, & A > 1/2 \\ 0, & A < 1/2 \end{cases} \tag{3.1}$$

where A is the pulse amplitude. Substituting these relationships into eqn. 2.5 of chapter 2, the soliton transmission characteristic is approximated by,

$$T = e^{-2\Gamma L}[1 - 2\alpha(1-\alpha)(1+cos\theta)] \tag{3.2}$$

where α is the coupler ratio, Γ is the loop fibre loss, L_{eff} is an effective length which is smaller than the actual fibre length due to loss given by (page76, [29]),

$$L_{eff} = \frac{L(1-e^{-2\Gamma L})}{\Gamma}. \tag{3.3}$$

and,

$$\theta = \pi \frac{L_{eff}}{z_0}\{(1-2\alpha)A^2 - [(1-\alpha)^{1/2} - \alpha^{1/2}]A\}. \tag{3.4}$$

Figure 3.5 shows the output predicted using this model and that predicted by the full split-step fourier solution of the Nonlinear Schroëdinger Equation (NLSE) for the 4.3km NOLM used in the feedback experiment of section 3.2.2. It is clear that there is close agreement between these two methods of solution at the first peak of the characteristic and, consequently, that the more simple soliton phase solution may be used to give a reliable prediction of the optimal experimental parameters.

It has been shown that loss in the two-device configuration must be compensated by appropriate design of the second NOLM. Since loss results in a mismatch between the power launched into the second NOLM and the input power at its first peak the required matching must involve reduction of the switching power

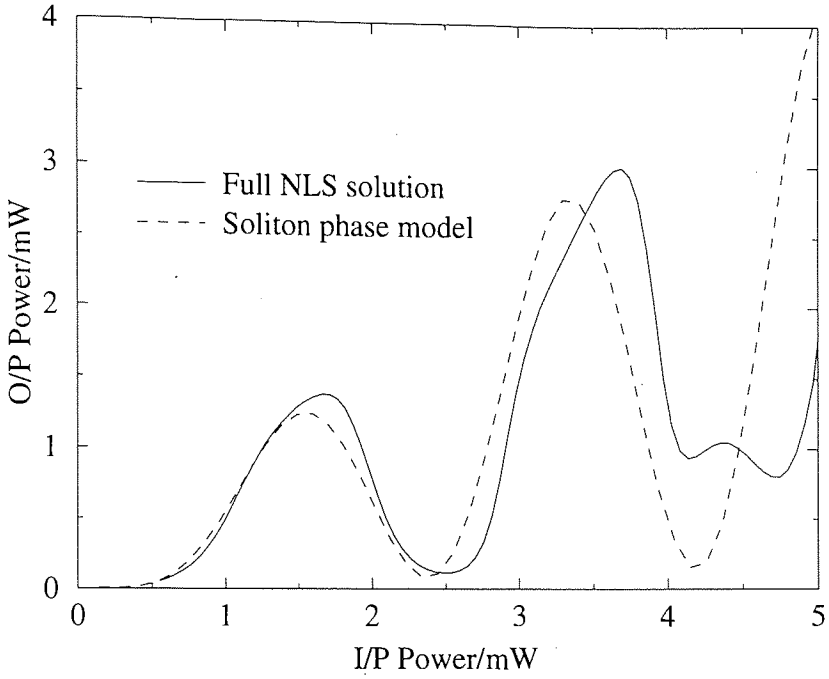

Figure 3.5: Predicted NOLM switching characteristic for previous experimental parameters using full split-step fourier solution of the NLS and using the soliton phase model.

at this peak. This is performed by introducing an increase in the accumulated nonlinear phase within the second loop, a condition which may be met by simply increasing the coupler asymmetry or by lengthening the loop. By taking the output predicted by the model for the 4.3km NOLM as a starting point the device parameters required for matching may be predicted.

Figure 3.6 plots the corresponding combinations of coupler ratio and loop length for the second NOLM which will produce optimal switching in the cascade. Taking a coupling ratio for this NOLM of α=0.4, and an estimated excess loss of between 0dB and 0.5dB, a reasonable assumption given the low quoted insertion loss of the couplers of ~0.1dB, this series of curves predicts an optimum fibre length of between 5.9km and 7km. The loop length of 6.4km used was therefore chosen to lie between these limiting values.

Figure 3.7 (i) shows an autocorrelation and sech^2 fit for pulses launched into the cascade and fig. 3.7 (ii) the corresponding spectrum. The measured pulse width was 6.9ps at 1527.8nm with a time-bandwidth product, $\Delta\nu\Delta\tau$, of 0.3. Figure 3.8 shows the individual response profiles of each device for these input

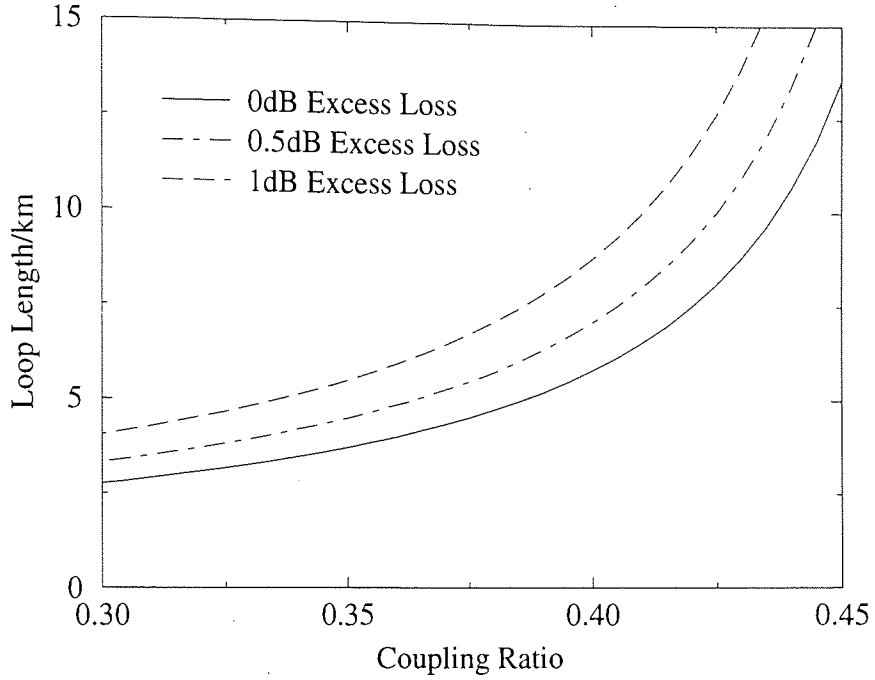

Figure 3.6: Relationship between coupler ratio and loop length of second NOLM for optimal switching in a two device cascade for excess loss levels of (i) 0dB, (ii) 0.5dB, and (iii) 1dB.

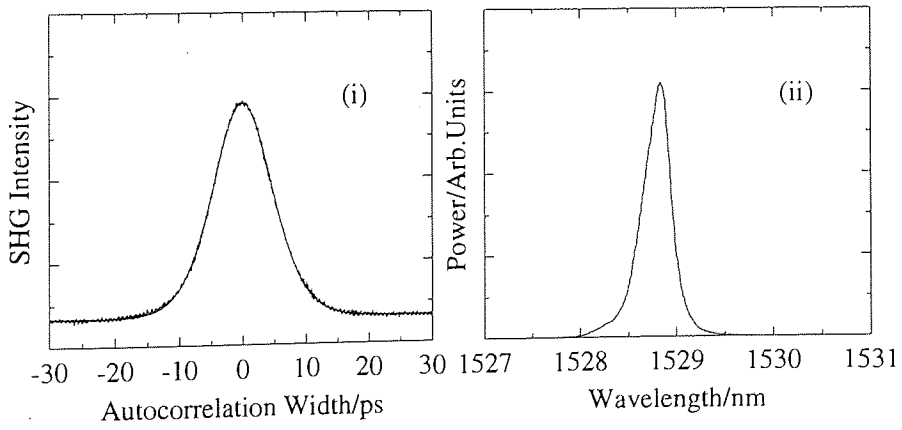

Figure 3.7: F-centre laser input pulses. (i) Autocorrelation and sech^2 fit. $\Delta\tau$ =6.9ps. (ii) Spectrum. λ = 1527.8nm, $\Delta\lambda$ =0.33nm, $\Delta\nu\Delta\tau$ =0.3.

pulses. The first and second peaks of the 4.3km NOLM characteristic (fig 3.8 (i))

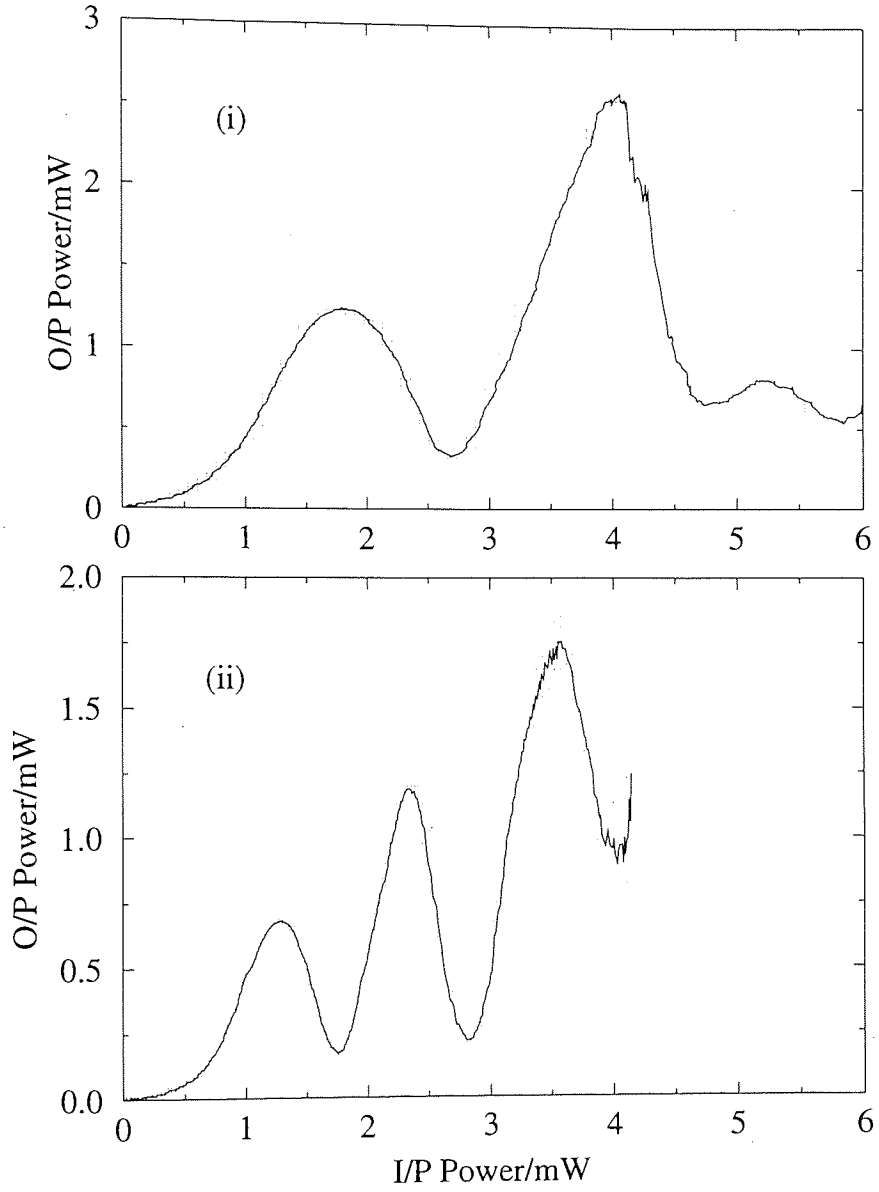

Figure 3.8: Time-averaged characteristic for (i) 4.3km NOLM. (ii) 6.4km NOLM.

occur at average powers (soliton order) of 1.8mW (N=1.8) and 4.2mW (N=2.7) respectively, with corresponding peak transmissions of 82% and 76%. The measured interpeak extinction ratios at the first and second minima are 8.3dB and 7.1dB. The switching peaks of the 6.4km NOLM occur at average powers (soliton order) of 1.3mW (N=1.5), 2.4mW (N=2) and 3.5mW (N=2.5) with extinction ratios at the first and second minima of 7.1dB and 8.3dB respectively. It is clear

that there is now close correspondence between the output power at the first peak of the first NOLM of 1.4mW and the input power at the first peak of the second NOLM in the sequence of 1.3mW. Thus, the soliton phase model is shown to give an accurate prediction of the device parameters required for optimal switching.

In passing, it is instructive to compare the input power levels at each of the main features of the 4.3km NOLM characteristic in this analysis with the results predicted by the numerical simulation in fig. 2.10 (ii) of chapter 2. It will be seen that the switching powers recorded here correspond more closely with the predicted values than those measured in that investigation (first peak input power=1.7mW and second peak input power=3.7mW). Since the operating wavelength chosen in this investigation was 1527nm rather than the wavelength used earlier of 1548nm, it may be concluded that this convergence is attributable to the wavelength dependence of the coupling ratio. Thus, it is probable that the ratio is closer, in this investigation, to the chosen numerical simulation parameter of α=0.4.

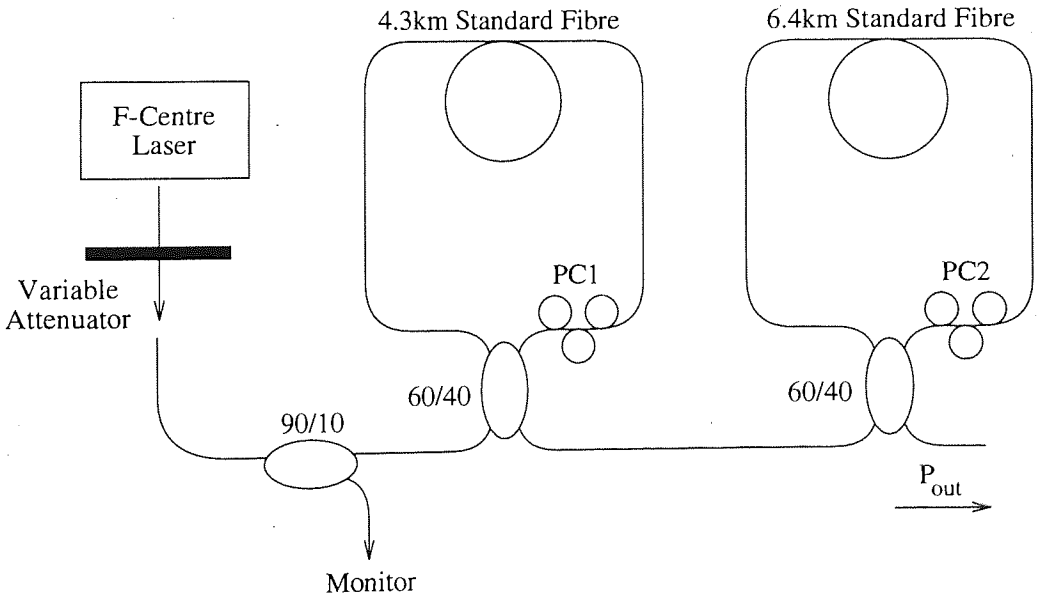

Figure 3.9: Schematic of optimised two device cascade.

Figure 3.9 shows a schematic of the amended two-device cascade. Pulses from the F-centre laser were launched into the sequence via a 90/10 coupler, and the switching response of the cascade was recorded using the technique already described. Figure 3.10 (i) shows the experimentally measured switching response

and fig. 3.10 (ii) the response predicted by numerical simulation including an excess loss of 0.6dB.

Taking each in turn, the first and second peaks of the experimental characteristic occur at average powers (soliton order) of 2mW (N=1.9) and 3.8mW (N=2.6) with measured peak transmissions of 37.5% and 32% respectively. The measured interpeak extinction ratio was 30dB. It is clear from inspection of this trace that an optimal cascade produces a flattened first peak with strongly sharpened edges. In addition, from comparison of the extinction ratios at the first minimum of each of the individual characteristics of 8.3dB and 7.1dB, it is clear that cascading results in a two-order-of-magnitude increase in this parameter. Thus, it has been shown that the response enhancement due to device cascading which has been demonstrated in CW switching may also be effected in the soliton regime.

Analysing the predicted response: the first and second peaks occur at average powers (soliton order) of 1.7mW (N=1.7) and 3.9mW (N=2.6) with peak transmissions of 43% and 39% respectively. The predicted interpeak extinction ratio is 30dB, in agreement with experiment and, again, there is reasonably good qualitative agreement between the predicted profile and the experimental trace. The slight discrepancies in predicted switching power are most likely due to the technique used to set the bias of each of the two NOLM's. Each was initially biased into linear reflection using a small input signal as described before. Further optimisation was then performed in real-time with the nonlinear response viewed on the digitizing oscilloscope. Since the nonlinear transmission of each device is critically dependent on the polarisation bias it is inevitable that the final switching characteristic will vary slightly from the predicted response.

As already mentioned, however, it is not enough just to consider the time-averaged response. For a data processing system, the spectral and temporal integrity of the emerging pulse train must remain uncompromised. Figure 3.11 (i) shows an autocorrelation and sech^2 fit for pulses emerging at the first peak of the cascade response and fig. 3.11 (ii) the corresponding spectrum. The measured pulse width, $\Delta\tau$, is 11.7ps with a time-bandwidth product, $\Delta\nu\Delta\tau$, of 0.39. The predicted pulse width is 9.2ps with a time-bandwidth product of 0.33. Thus, as in the case of pulses emerging from a single NOLM, the switched pulses undergo a small degradation in time-bandwidth product but retain their sech^2 temporal profile. It can be seen, then, that even after transmission through two NOLM's,

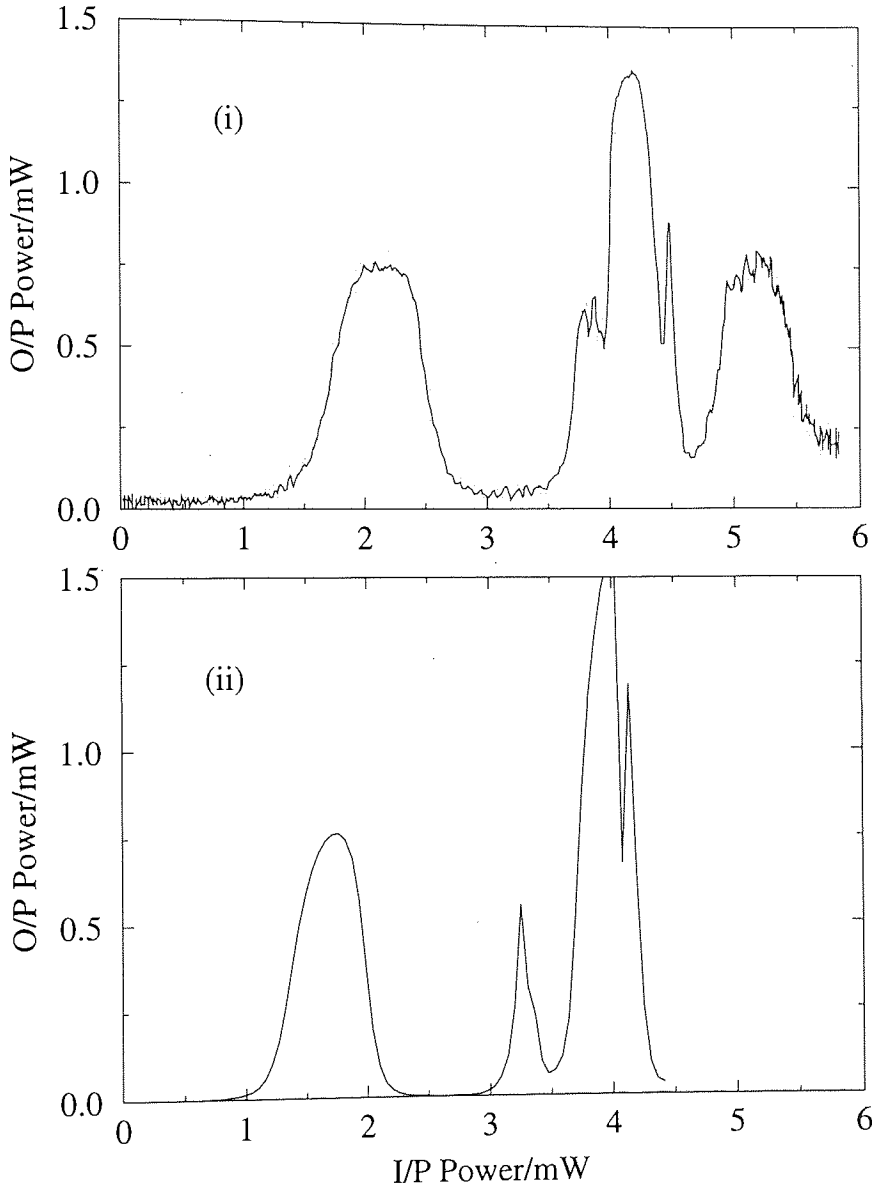

Figure 3.10: (i) Experimental time-averaged characteristic for optimised NOLM cascade. (ii) Predicted time-averaged response including 0.6dB excess loss.

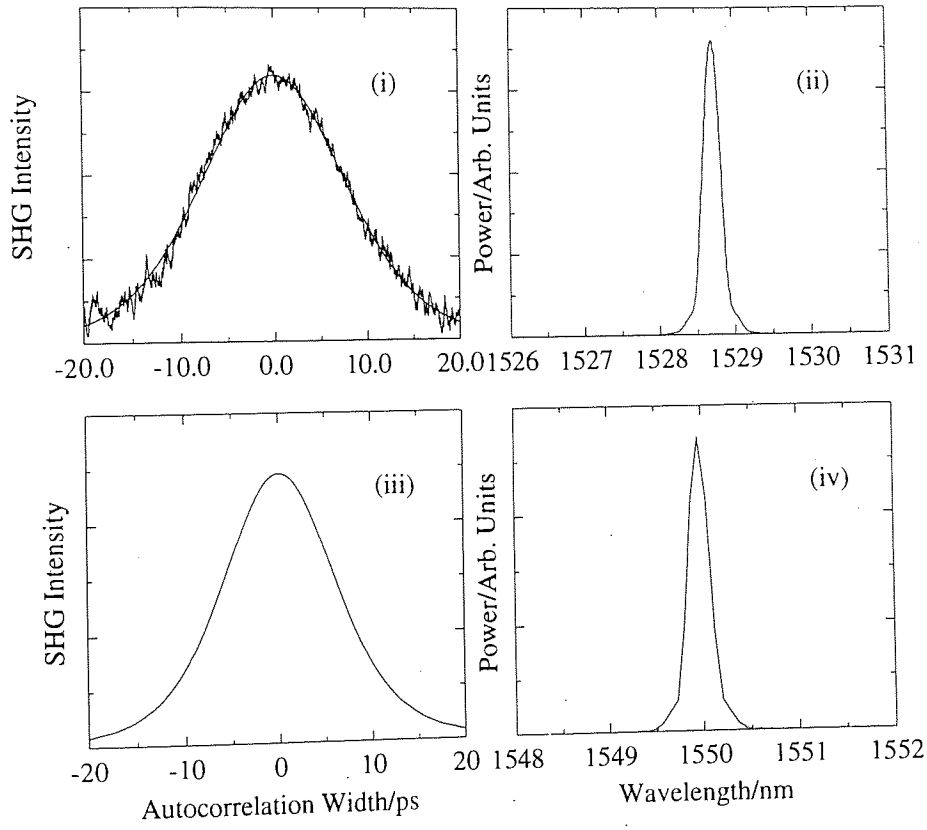

Figure 3.11: (i) Experimental autocorrelation and sech^2 fit for pulses emerging at first peak of concatenated response. $\Delta\tau$ =11.7ps, P_{in} = 2mW. (ii) Corresponding spectrum. λ =1528.7nm, $\Delta\lambda$ =0.26nm, $\Delta\nu\Delta\tau$ =0.39. Predicted autocorrelation at first peak. $\Delta\tau$ =9.2ps, P_{in} = 1.7mW. (iv) Corresponding spectrum. $\Delta\lambda$ =0.29, $\Delta\nu\Delta\tau$ =0.34.

emerging pulses have largely retained their soliton characteristics. Since the input pulses are extremely close to perfect solitons in this analysis, the effect of self-adjustment to compensate for an initial chirp is probably minimal and the increase in pulse width is most likely dominated by loss-induced adiabatic broadening as a result of the longer propagation distance of the cascade. However, the effects of this phenomenon may be readily overcome by the inclusion of an appropriately designed erbium-doped fibre amplifier (EDFA).

Despite these effects, it remains clear that the soliton is robust enough to travel even through a cascade of two NOLM switches without significant perturbation. Moreover, the pulses emerging from the sequence are shown to largely retain their soliton characteristics. Thus, device cascading in the soliton regime leads to an enhancement of time-averaged performance, with only minimal degradation in data integrity.

3.3 Enhancement of Spectral Selectivity Using In-fibre Bragg Reflectors

3.3.1 Introduction

In a recent experimental demonstration, the concept of wavelength division multiplexing (WDM) was shown to be capable of sustaining a data rate of 100Gbit/s over trans-oceanic distances by the simultaneous transmission of 20 discrete wavelength NRZ channels, each at a base data rate of 5 Gbit/s [73]. Components for such multi-wavelength systems, which exploit the extremely large optical bandwidth of fibres by extending the transmission dimension into the spectral domain, require processing devices which will respond to only a single, or defined set of discrete wavelengths [74].

Since the traditional NOLM configuration is an inherently broadband device due to the "slow" variation of coupling ratio with wavelength [59], a technique which significantly increases wavelength selectivity must be found if it is to meet the demands of WDM systems.

In response to this need, the current section extends the discussion of response enhancement by concatenation to include tailoring of the spectral responsivity of the NOLM. Results from two experimental configurations are presented which combine the excellent spectral discrimination of the in-fibre Bragg grating with the advantages of the NOLM to produce a nonlinear switch with a low switching power and high spectral selectivity.

3.3.2 The In-Fibre Bragg Grating

Recent years have seen a rapid growth in interest in the in-fibre Bragg grating, a device which is of potentially great practical importance in optical communications due to the wide range of applications to which it is suited [75, 76]. Currently, fibre Bragg gratings are formed by transverse exposure of photosensitive optical fibres to the fringe pattern resulting from interference of two intense UV beams. Two fringe formation techniques have been used. In the first, interference is effected by the splitting and recombination of a single beam [77, 78, 79] and in the second technique, near-contact fibre exposure through a phase mask, by interference between the diffracted orders of a surface relief grating [80]. In both cases, the sinusoidal intensity variations associated with the interference pattern give rise to an accompanying positive sinusoidal modulation of the core refractive index given by [75],

$$n(z) = n_{core} + \delta n[1 + cos(2\pi z/\Lambda)] \tag{3.5}$$

where n_{core} is the core refractive index, δn is the amplitude of the photoinduced index excursion and,

$$\Lambda = \frac{\lambda_{uv}}{sin\theta/2}. \tag{3.6}$$

where λ is the wavelength of the incident light, and θ is the angle between the interfering beams. To an incident optical signal, this modulation appears as a series of partially reflecting refractive index boundaries which give rise to a coupling of the forward propagating optical energy into a counter-propagating mode with maximum reflection occurring at the Bragg wavelength,

$$\lambda_B = 2n_{eff}\Lambda \tag{3.7}$$

where n_{eff} is the mode effective index in the fibre. It is this spectral selectivity, combined with the fibre-integrated nature of the device, which lies at the root of the considerable interest which the Bragg grating has aroused.

A number of grating-based interferometric and resonant configurations have been developed which are aimed at applications requiring spectral filtering. These include Fabry-Perot structures for soliton control [81, 82, 83] as well as, for WDM processing systems, Mach-Zehnder-based wavelength demultiplexers [84, 85, 86] and Michelson-interferometer-based [87, 88] transmission filters. In addition, aperiodic (chirped) structures, in which the grating pitch varies along the length of the device, have found applications in dispersion compensation [89, 90, 91], and pulse compression [92, 93].

In the succeeding discussion, application of the fibre grating is taken a step further. By inclusion of the device inside the fibre loop, the grating is used as a means of spectrally quantising the overall response of a NOLM by confining the influence of both SPM and XPM within the device to a discrete range of wavelengths. The result is a nonlinear fibre device with the combined advantages of each: strong wavelength discrimination and low switching power. Before going on to a discussion of the experimental details, the next section addresses the underlying the switching mechanisms exploited.

3.3.3 Further NOLM Switching Mechanisms

So far, these experimental investigations of NOLM switching have been confined to the asymmetric coupler configuration, a configuration which, as stated above, is inherently broadband in operation. However, two other mechanisms exist which, although not inherently wavelength-selective in themselves, may, nevertheless, be accessed to produce wavelength selectivity by the use of in-fibre Bragg reflectors.

The first uses an asymmetrically arranged gain or loss element to perform self-switching. In self-switching, asymmetric phase evolution due to different counter-propagating intensity levels leads to an intensity dependent transmission characteristic, a switching regime which, as demonstrated already, may be implemented using an asymmetric coupling ratio. Asymmetry may also be induced, however, by the introduction of an asymmetrically arranged gain or loss element [94, 95, 96]. This particular solution has the benefit of allowing a coupling ratio of 50/50 (α=0.5), a value which ensures that the linear reflectivity of the device

is at its maximum value of 100%.

The second technique uses the induced asymmetric cross-phase-modulation (XPM) of a strong control pulse on weaker signal pulses. By configuring the loop so that a high intensity control pulse co-propagates with the input signal stream in only one arm of the device, an asymmetric phase shift is induced on the weaker input signal pulses due to XPM. If the power of the control stream is high enough to induce a phase shift of π on the signal pulses which accompany it, then the NOLM will switch. This second switching technique has been demonstrated using two schemes. The first uses a control signal at a second wavelength [97] and the second a control in the orthogonal polarisation state to that of the signal [98]. The dual-wavelength technique has found extensive application in ultrafast demultiplexing both using fibre [99, 100, 101] and semiconductor laser amplifier nonlinearity [102], with reported demultiplexing from data streams at rates in excess of 100Gbit/s [103, 102, 104].

By introducing fibre Bragg gratings into a basic NOLM configuration, both of these switching mechanisms can be effected. Firstly, since the Bragg reflector may be thought of as a wavelength-dependent loss, self-switching may be achieved in a NOLM by inclusion, in the fibre loop, of an asymmetrically placed partially reflecting grating. In this way, differential nonlinearity is achieved only over the reflection bandwidth of the grating. Taking this concept a step further. If the reflectivity of this asymmetrically placed reflector is increased to 100% it will act to completely block transmission of the wavelengths which lie within its reflection band, thereby confining those wavelengths to only one arm of the device. Thus if strong control pulses are incident at a wavelength within the grating reflection band, dual-wavelength switching may be achieved. At wavelengths outside the grating reflection profile, switching is inhibited by the symmetric XPM from two counter-propagating control signals.

It is clear, therefore, that the wavelength response of a NOLM may be quantised in both the self- and control-pulse-switched cases by inclusion of asymmetrically placed Bragg gratings with appropriate reflectivities. The following sections present results from experimental demonstrations of each of these concepts. In both cases it is shown that bandpass switching, *i.e.* switching only at wavelengths within the reflection bands of each grating, is achieved.

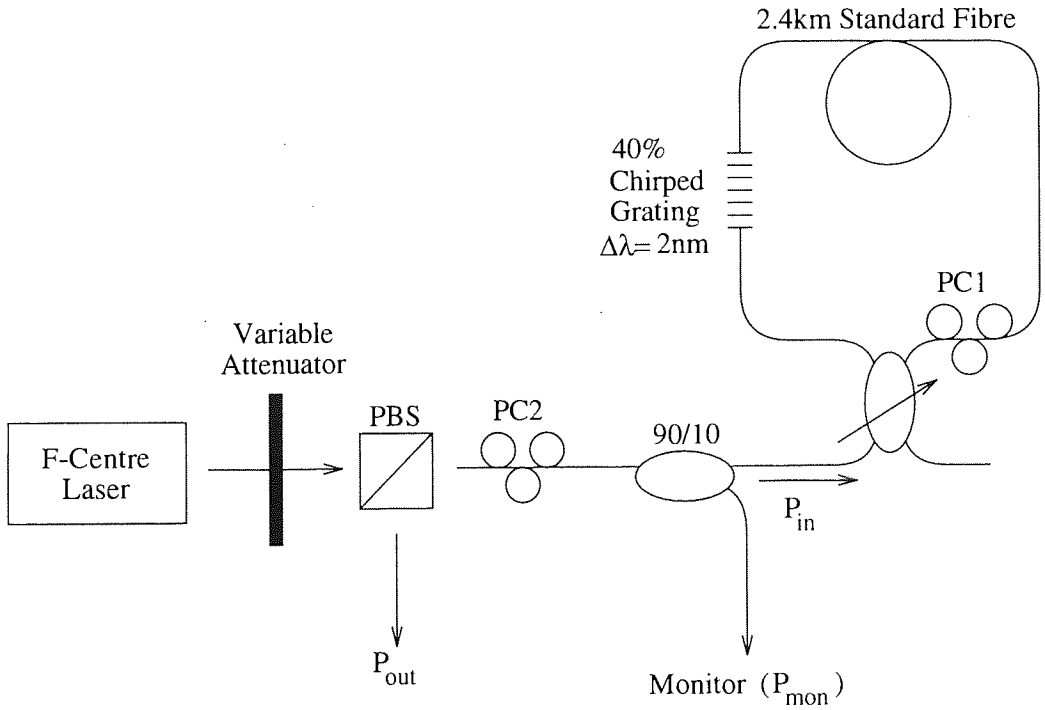

Figure 3.12: Schematic of experimental configuration for investigation of bandpass self-switching in a NOLM.

3.3.4 *Bandpass Self-Switching in a NOLM*

A schematic of the experimental configuration is shown in fig. 3.12. Pulses at 76MHz from the same F-centre laser were launched into the NOLM via a 90/10 coupler. The NOLM was constructed using a variable ratio coupler and a 2.4km length of standard telecommunications fibre (STF). The asymmetric loss element was implemented using a chirped in-fibre Bragg reflector centred at 1550nm with a bandwidth of 2nm and a peak reflectivity of ~60%. The grating was fabricated in-house by side-exposure of photosensitive fibre with a UV beam at a wavelength of 244nm [78]. The reflection profile, recorded using broadband erbium doped fibre fluorescence, is shown in fig. 3.13. The insertion loss of the NOLM, measured with low signal power at a wavelength inside the grating reflection profile, was found to be 6dB.

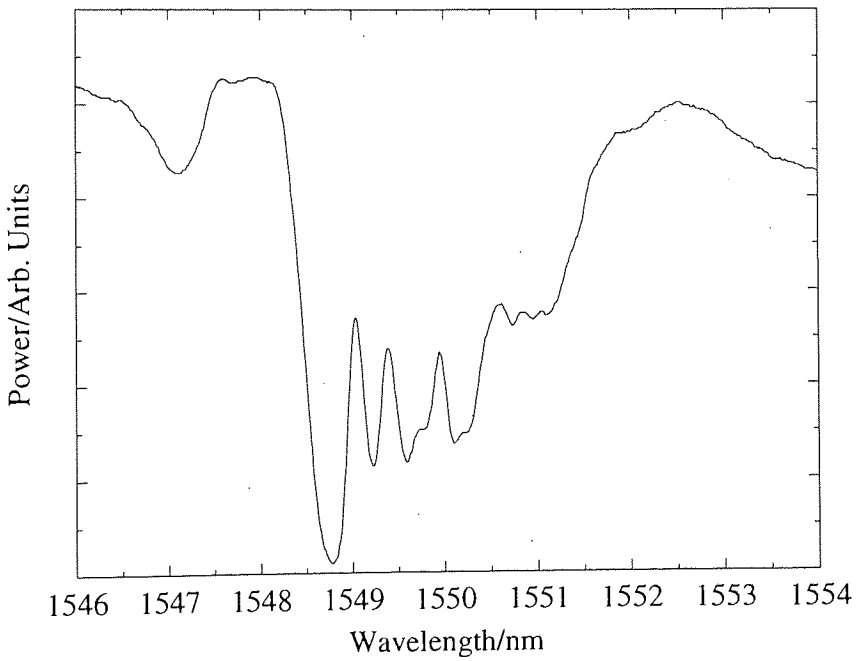

Figure 3.13: Reflection profile of grating used as a wavelength dependent loss element for bandpass self-switching in a NOLM. Peak reflectivity = 60%.

Since the grating is partially reflecting, there is a need for separation of the nonlinearly switched signal from these reflections. This was achieved by operating the NOLM in linear transmission. In this mode of operation the nonlinearly reflected signal is orthogonally polarised to the input signal and hence, also, to grating reflections [59, 105]. Thus, in a similar manner to the double-pass

configuration of section 3.2.2, the nonlinearly reflected signal can be isolated using the polarising beam splitter (PBS) by adjustment of PC2 to maximise P_{out} (see fig. 3.12). The nonlinear response may then be viewed in the usual manner by displaying P_{out} and P_{mon} on the Gould digitizing oscilloscope.

Figure 3.14 (i) shows an autocorrelation and sech^2 fit of pulses launched into the NOLM and fig. 3.14 (ii) the corresponding spectrum. The measured pulse

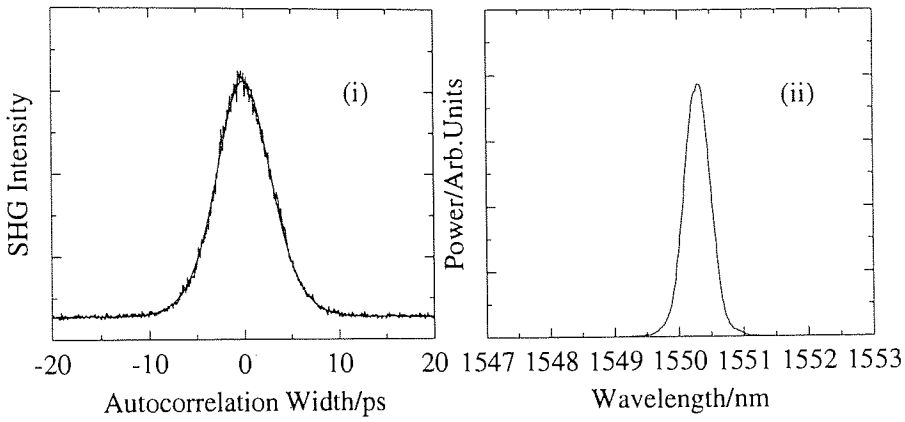

Figure 3.14: F-centre laser input pulses. (i) Autocorrelation and sech^2 fit. $\Delta\tau$ =6.7ps. (ii) Spectrum. $\Delta\lambda$ =0.4nm, $\Delta\nu\Delta\tau$ =0.33.

width was 6.7ps with a time-bandwidth product, $\Delta\nu\Delta\tau$, of 0.33. In order to ensure that any observed nonlinear switching was due solely to the grating, it was necessary to compensate for asymmetry arising from other sources, e.g. splice loss. This was performed by tuning the colour centre laser to a wavelength shorter than the grating reflection peak and varying the coupler splitting ratio until the nonlinear response of the device was extinguished. Under these conditions the grating is transparent to pulses propagating in the loop and any switching observed must, therefore, be due to other sources of asymmetry.

Figure 3.15 (i) shows the time-averaged nonlinear response of the NOLM with the F-centre laser tuned onto the grating reflection profile. The first and second peaks occur at average input powers (soliton order) of 3.8mW (N=2.56) and 7.8mW (N=3.66) respectively. It is clear from Fig.2(ii), which shows the response of the device when the laser is tuned off the grating peak to 1546nm, that the switching response is virtually extinguished at wavelengths outside the grating reflection band, indicating that nonlinear switching is quantised due to the wavelength selectivity of the Bragg grating. Although the potential for wavelength

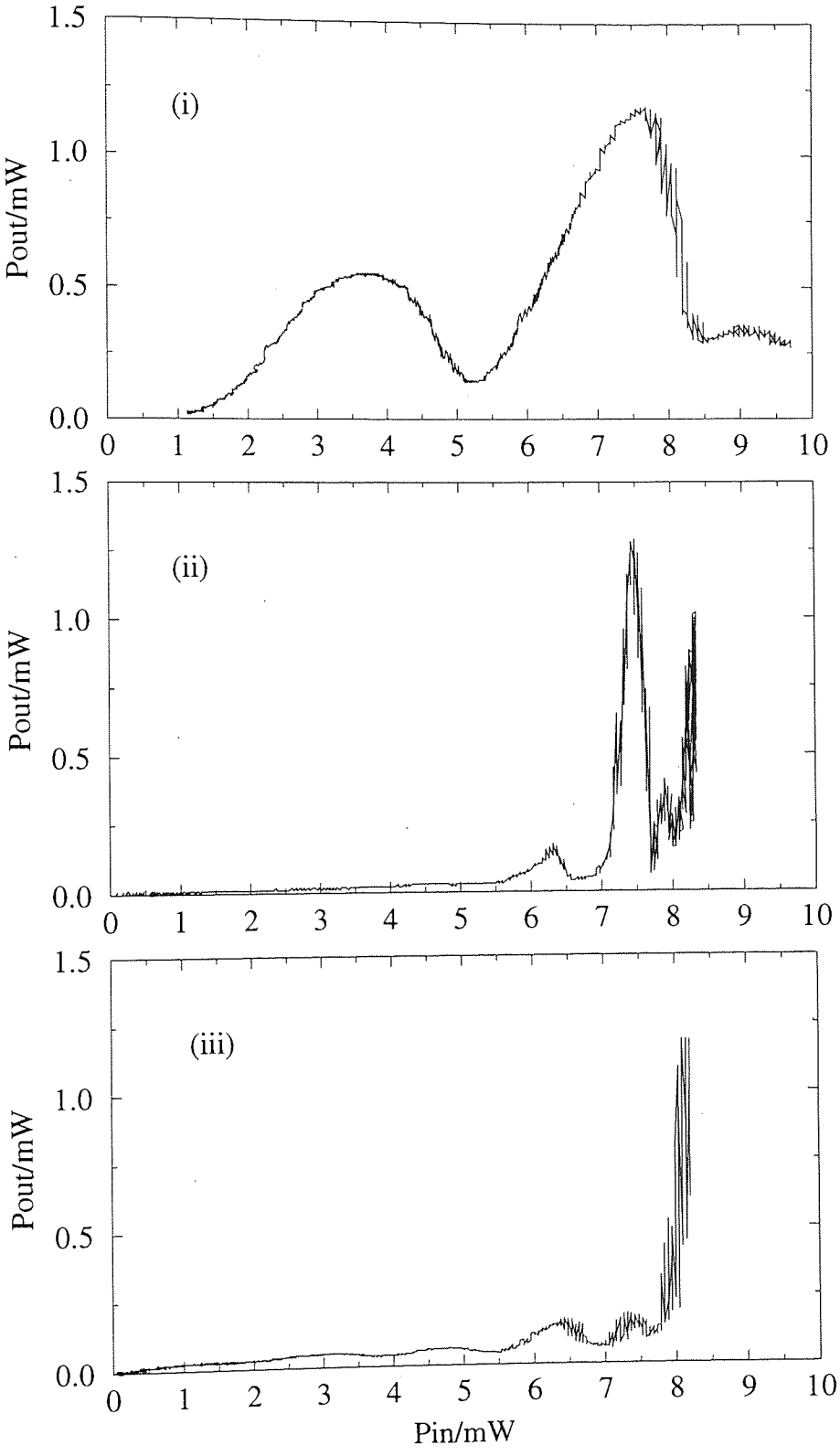

Figure 3.15: Nonlinearly reflected signal with (i) F-centre laser tuned onto grating. (ii) F-centre laser tuned away from grating reflection profile. λ =1546nm. (iii) grating cooled using liquid nitrogen vapour.

dependent nonlinear switching in Bragg gratings has been recognised for some time [106, 36], in practice, switching using the device on its own has required prohibitively high switching powers of around 4kW [107]. The switching power at the first peak of this configuration, which corresponds to a peak input power level of 7W, therefore, represents a three order-of-magnitude reduction in switching threshold. Thus, this new configuration is an optimal combination of the principal advantages of each device *i.e.* the high degree of wavelength discrimination of the Bragg grating and the low switching power of the NOLM.

An alternative technique by which the nonlinear response of the NOLM may be turned off is by tuning the grating away from the F-centre laser signal wavelength, which may be performed by heating or cooling of the grating. Figure 3.15 (iii) shows the nonlinear response of the NOLM when the grating is cooled using liquid nitrogen vapour. Again, it is clear that the nonlinear response of the device has been extinguished. The slightly higher output power level in this case is ascribable to the change in loop birefringence caused by mechanical deformation of its protective plastic coating on cooling. Thus, it would appear that this configuration, while demonstrating good nonlinear wavelength discrimination, may have limitations in sensing applications.

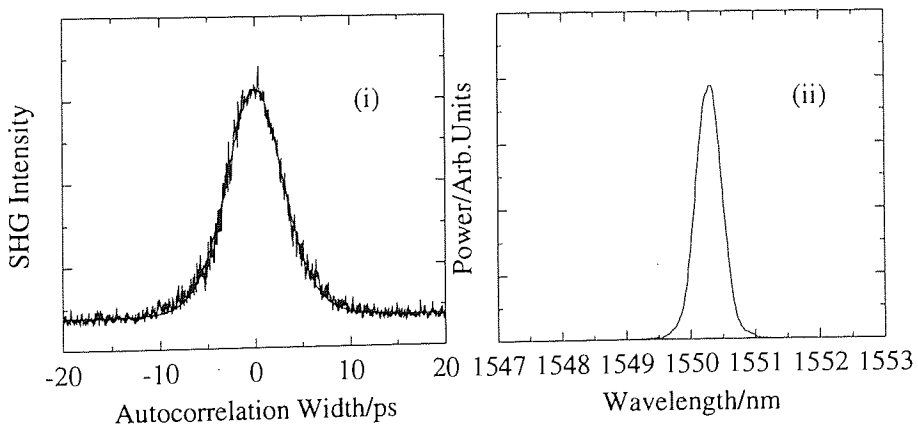

Figure 3.16: (i) Autocorrelation and sech^2 fit at first peak of NOLM switching characteristic. $\Delta\tau$ =7.0ps, P_{in} =3.8mW (ii) Corresponding spectrum. $\Delta\lambda$ =0.46nm, $\Delta\nu\Delta\tau$ =0.4.

Figure 3.16 (i) shows and autocorrelation and sech^2 fit of pulses emerging at the first peak of the switching characteristic and fig. 3.16 (ii) the corresponding spectrum. The measured pulse width is 7.0ps with a time-bandwidth product,

$\Delta\nu\Delta\tau$, of 0.4. Thus, as in previous experiments, there is only marginal degradation of pulse quality on transmission through the combined device. The wavelength discrimination of this configuration is limited, ultimately, by the relative bandwidths of the grating and the incident signal. Numerical analysis performed in this lab for linear gratings has shown that the quality of pulses transmitted through a Bragg reflector is significantly degraded only when the bandwidth of the reflection profile is smaller than the overall bandwidth of the input pulse spectrum [108], a condition which did not hold in this experiment. Thus it is shown that, provided the reflection bandwidth of the grating is large enough to contain the entire spectral content of the input signal, pulses emerging from the device remain capable of further processing, in line with previous findings.

3.3.5 Dual-Wavelength Switching Using A Fibre Bragg Reflector

As already mentioned, by extending this concept and increasing the reflectivity of the grating towards 100%, a signal incident on the NOLM at a wavelength within the grating reflection band will be restricted to only one arm of the device. Using this principle, a high power control pulse at a wavelength λ_1, which lies within the grating reflection characteristic, may be used to switch a low power signal pulse at a second wavelength, λ_2, which falls outside the reflection band. For control pulses at wavelengths beyond the grating profile switching is inhibited due to the symmetric XPM of two counter-propagating control signals and nonlinear switching is, therefore, spectrally confined.

A schematic of the experimental arrangement used to demonstrate this concept is shown in fig. 3.17. In this case, the NOLM was constructed using a 50/50 coupler and 11km of dispersion-shifted fibre (DSF1) with a zero dispersion wavelength, λ_0, of 1551nm. Rejection of the control signal from one arm was achieved using a linear Bragg grating centred at λ_g=1535nm with a nominal reflectivity of 95%. Signal light at 1539nm (λ_2) from a DFB laser, amplified using a 980nm pumped EDFA, was combined with 10ps control pulses at 1535nm (λ_1) from the colour centre laser using a 90/10 coupler. For these two wavelengths, the control pulse walk-off length, *i.e.* the propagation distance required for the two signals to accumulate a relative delay of 10ps, was 10.6km. Residual control pulse energy reflected by the grating was separated from the switched signal stream using a bulk diffraction grating, and the isolated signal was monitored using a 22GHz

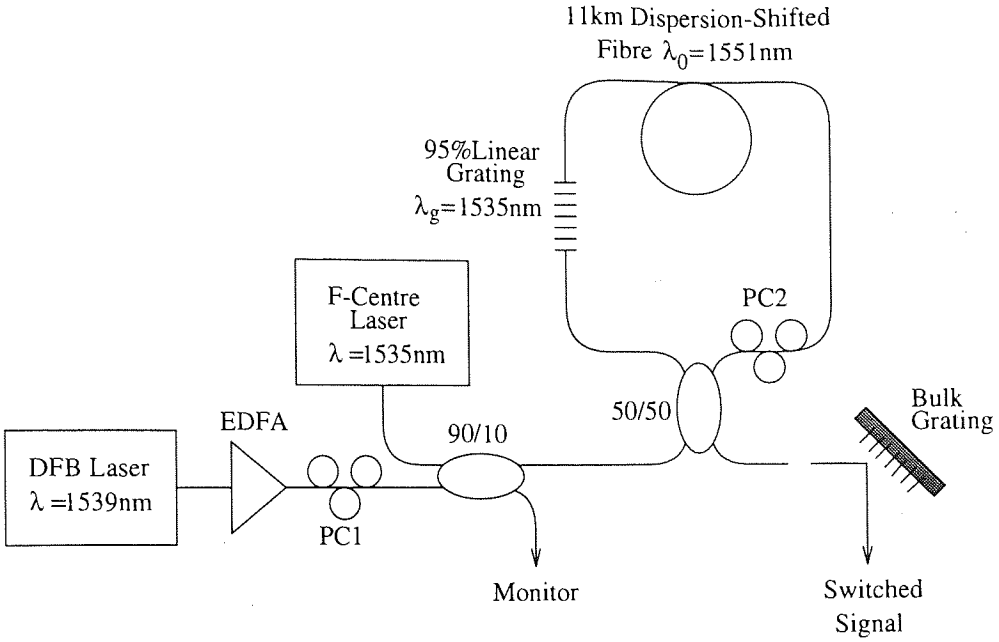

Figure 3.17: Schematic of experimental configuration for investigation of bandpass control-pulse-switching in a NOLM.

photodiode.

The switching window of the device was measured, initially, with the DFB laser running CW and the NOLM biased into linear transmission. In this mode of operation, the presence of control pulses from the F-centre laser results in nonlinear reflection of the portion of the signal which they overlap giving rise to a "hole" in the transmitted signal. Figure 3.18 (i) shows this result. The measured extinction ratio was 4.8dB with a switching window width, τ_{win}, of 70ps. Since the walk-off length for these wavelengths is 10.6km, it might have been expected that the measured switching window would have been unlikely to be much greater than 10ps. This higher measured value may be attributed to SPM enhanced dispersive broadening, since the control signal wavelength lies in the normal dispersion regime (chapter 4, [29]), a conclusion which is borne out by the switching window asymmetry [109].

Figures 3.18 (ii) and (iii) summarise results taken with the DFB gain-switched at a repetition rate of 76MHz using a HP 8133A pulse generator . Synchronisation between the control and signal pulses was achieved by triggering the pulse generator with a signal derived from the modelocker used by the F-Centre laser

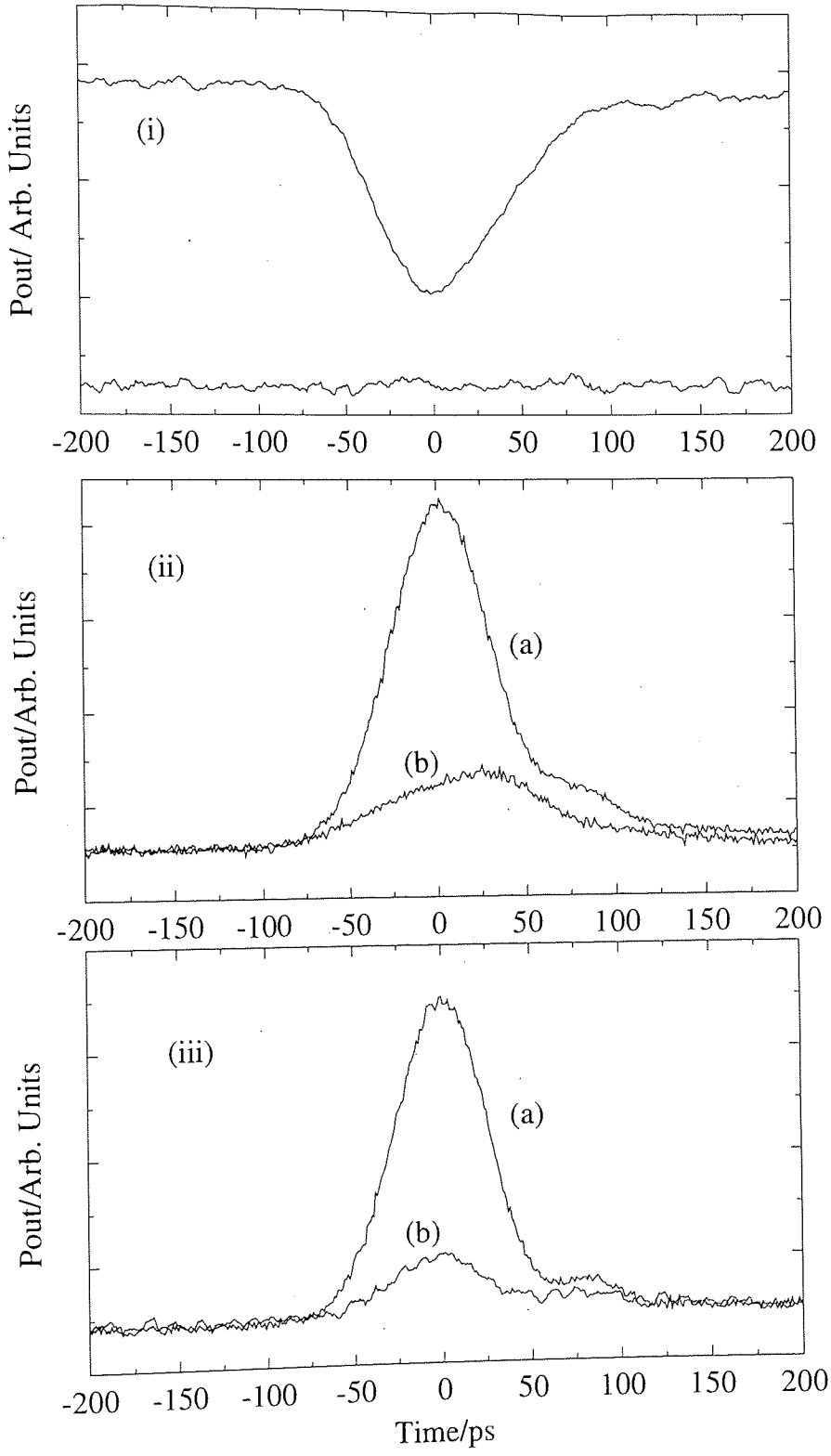

Figure 3.18: (i) Switching window of dual-wavelength NOLM configuration. τ_{win}=70ps. (ii) NOLM in linear transmission with (a) control signal absent. (b) control signal present. (iii) NOLM in linear reflection (a) control signal on grating. (b) control signal off grating.

pump source. Figure 3.18 (ii)(a) shows the output at 1539nm with the NOLM biased into linear transmission and the control pulses absent from the loop. The emerging gain-switched pulse has a measured pulse width, $\Delta\tau$, of 62ps. Figure 3.18 (ii)(b) shows the same output with the control pulses present. It is clear that introduction of the control pulses causes the output of the device to be significantly extinguished. The measured extinction ratio was 4.8dB, in agreement with the CW switching window measurement, at a switching threshold of 2mW, corresponding to a pulse energy of 26pJ. It was found that by detuning the modelocking of the colour centre laser to produce longer control pulses, the extinction ratio could be increased to values greater than 7dB due to the improved overlap between the signal and control pulses. This limitation of extinction ratio is a product of the relative temporal widths of the signal and control pulses. Since the control pulse walk-off length in the fibre used was not sufficient to cause complete walk-through at the input wavelengths, whole pulse switching relied largely on SPM enhanced temporal broadening which results in reduced switching efficiency and asymmetry in the device switching window. In chapter 5, dual-wavelength switching in a similar NOLM is shown to be capable of 100% extinction by using control pulses with a similar duration to that of the lower power signal pulses. It is expected, then, that increasing the control pulse width will result in more efficient switching in this grating-based configuration. Using the experimental sources described, this could be simply achieved by using the amplified DFB as the source of switching pulses.

Trace (a) of fig. 3.18 (iii) shows the nonlinearly switched portion of the input signal pulses recorded with the NOLM biased into linear reflection and the control pulses present. To demonstrate the bandpass nature of this nonlinear response, the wavelength of the control signal was tuned away from the grating peak to 1531nm. The resultant output is shown in trace (b). Again, the wavelength detuning required to extinguish the response was 4nm. The low level residual signal can be attributed to a slight imbalance in the coupler splitting ratio which gives rise to a small differential nonlinearity in the arms since the control signal wavelength does not correspond precisely with the 50/50 point of the device (λ = 1550nm). The results clearly demonstrate, however, that the response of the device is confined to control signal wavelengths inside the reflection band of the grating.

It is clear from both demonstrations that the extension of the basic NOLM configuration to include an asymmetrically located in-fibre Bragg reflector has the effect of spectrally quantising the response of the device. A drawback of each experimental configuration, however, is the fact that additional components are required to separate unwanted residual reflections, a difficulty which may be readily overcome by replacement of the gratings used with slanted fringe versions. Thus it has been shown that the concept of device cascading may be used to tailor the spectral responsivity of the device enabling application of the NOLM in WDM.

3.4 Conclusions

This chapter has introduced the concept of device concatenation, a concept which is fundamental to the construction of photonic processing systems. Results have been presented which show that both the amplitude and spectral responses of a NOLM may be tailored by serial and inclusive concatenation.

The first experimental study has shown that loss is a primary design concern for the construction of a device cascade which is based on asymmetric coupler devices. It is imperative that the switching characteristic of the second device in the sequence be designed to account for fibre loss and imperfect nonlinear transmission in the first. The simple analytic analysis which has been developed, and which may be applied to devices of arbitrary length, facilitates this design process by accurately predicting the combinations of fibre length and coupling ratio which may be used in the second device if the parameters of the first are known.

The time-averaged output of such a cascade has been shown to exhibit the clear advantages of a nonlinear device cascade which are known in CW switching. Cascading results in sharper switching edges, squarer peaks, giving rise to an increase in immunity to small-scale input amplitude fluctuations, and increased interpeak extinction ratios, giving enhanced amplitude discrimination at the switching edges. Crucially, however, the temporal and spectral characteristics of pulses emerging from such a cascade are not significantly degraded due to propagation through the individual devices, and the soliton character of the output is largely maintained.

In addition, by adapting the basic NOLM to include in-fibre Bragg reflectors

in alternative implementations of nonlinear switching by asymmetric loss and a strong control signal, the advantages of each device have been combined to produce a configuration with a high degree of wavelength discrimination and low switching power. In both cases, it is clear that self- and control-pulse-switching may be spectrally confined by inclusion of an asymmetrically arranged fibre Bragg grating of an appropriate reflectivity. It is also apparent, however, that the wavelength discrimination is ultimately limited by the relationship between the spectral widths of the grating and the input signal pulses, and further investigation is required to evaluate the extent to which the bandwidth of the configuration as a whole can be reduced before damage is seen to occur to the temporal and spectral integrity of input pulse trains. The only conclusion which can be drawn currently, is that if the reflection characteristic is broad enough to fully contain the spectral content of the input signal, then the emerging pulse train retains its overall temporal and spectral characteristics.

It is clear, then, that serial and inclusive device concatenation using primitive all-optical components enables optimisation of device characteristics to produce enhanced device performance. In the next chapter, the principle of concatenation is further applied to effect ultrashort pulse generation.

Chapter 4

Actively Mode-Locked Dual-Wavelength Erbium Fibre Laser

4.1 Introduction

The development of systems for the generation of ultrashort pulses is a primary requirement for high data rate transmission and switching systems; both applications demanding stable sources of picosecond regime pulses at multigigabit repetition rates. In particular, information processing systems, in which primitive all-optical components are configured to perform such diverse functions as all-optical packet routing [110, 111, 112], demultiplexing [20, 113], regeneration [69], and clock multiplication and division [70, 114] through the interaction of independent data streams, place considerable design constraints on pulsed data sources. Such architectures, in which a multiplicity of wavelengths is inherent, require sources which enable accurate wavelength definition of pulse streams with extremely low levels of relative timing jitter. This chapter presents an experimental demonstration of a laser configuration which meets both of these criteria, enabling the generation of synchronised trains of ultrashort pulses at arbitrarily defined wavelengths with jitter levels which allow application to switching environments with internal data rates in excess of 100Gbit/s.

To date, a number of ultrashort pulse generation techniques have been proposed. These include beat signal conversion through adiabatic soliton compression in dispersion decreasing fibre, pulsed semiconductor lasers and mode-locked erbium fibre lasers [115]. In particular, fibre lasers have attracted considerable attention due to their "natural" generation of solitons as well as for their potential for simple integration into optical fibre environments. Consequently, a range of configurations has been demonstrated, operating in both passive and actively mode-locked regimes.

The figure-of-eight laser (F8L) [116, 117], a passively mode-locked configuration, employs a nonlinear-amplifying loop mirror (NALM) [94] as a saturable

absorber and has been used to generate pulses of a only few hundred femtoseconds duration. However, this configuration has three major drawbacks. Firstly, since the NALM preferentially switches square pulses as well as solitons, the laser has been found to generate not only picosecond regime solitons, but also nanosecond regime square pulses at the cavity round-trip frequency [118]. Secondly, when operating in the soliton regime, the lack of repetition rate control results in the generation of pulse trains whose constituent pulses have randomly distributed temporal positions within the cavity round trip period. Thirdly, the generation of a constant frequency pulse train requires reduction of the intracavity power until only one pulse per round trip can be supported, thereby restricting the maximum achievable repetition rate. This final problem may be alleviated to an extent by the inclusion of a sub-ring cavity [119], but requires accurate control of intracavity power for successful operation. These three factors make the F8L configuration unattractive for optical transmission and switching systems.

To overcome the uncertainty in pulse repetition frequency, active mode-locking techniques have been applied to both ring and standing-wave cavities. Specifically, mode-locking of ring cavities has been achieved by the inclusion of bulk phase and amplitude modulators [120, 121] with typical repetition rates of around 10GHz. However, since the lasers are harmonically mode-locked at these repetition rates, with cavity lengths on the order of hundreds of meters, small mechanical perturbations and thermal expansion result in significant variations in operating frequency as well as degraded long-term pulse stability. Thus, additional components for feedback control are required with a consequent increase in system complexity [121, 122]. In addition, although all-optical modulation has been demonstrated [123, 124], wavelength tunability of the generated pulse train requires the inclusion of bulk tunable filters.

The need for wavelength selectivity can be met through the use of Bragg grating end-mirrors, and this use has been reported in standing-wave cavity configurations [125, 126]. In the implementation of ref. [126] mode-locking was achieved by the use of a dual-wavelength NOLM modulator to produce a fully fibre-integrated picosecond pulse source. Although tunability could be achieved in these configurations through mechanical stretching of the grating, the safe stretch limit for fibre of 0.3% was shown to restrict the tuning range to a maximum of only 3.5nm [125].

The sources summarised so far have been used to generate pulse trains at

a single wavelength. However, since all-optical processing can involve the interaction of pulse streams of different wavelengths, there is also a requirement for sources which can simultaneously generate synchronised pulse trains at a range of wavelengths, a requirement which must also be met for applications in wavelength division multiplexed (WDM) transmission systems. Since ultrafast all-optical WDM components demonstrate tightly specified wavelength responses [127], considerable demands are, consequently, placed on the sources used. As well as allowing their operating wavelengths to be set to high accuracy over a wide range of wavelengths, temporal stability is also a fundamental consideration. In addition, complex all-optical processing architectures, in which independent channels at different wavelengths interact to effect high level switching functions, place tight tolerance limits on the allowed jitter between interacting pulse streams [128, 129, 20]. An additional requirement, then, is that the source jitter performance must fall within the design constraints imposed by ultrafast switching devices.

To date, multiwavelength operation has been demonstrated in both actively mode-locked [130, 131] and passively mode-locked configurations [132]. However, the mode-competition inherent in the use of, largely homogeneously broadened, erbium doped fibre amplifiers (EDFA's) restricts single amplifier configurations to wavelengths receiving the same gain. In the first case [130, 131], this condition is met by choosing closely spaced wavelengths, but the operating range is limited to only a small section of the available gain band. Although the F8L laser of ref. [132] uses a second amplifier to extend the spectral output range, the pulse trains generated suffer from the drawbacks detailed at the start of this section and are not synchronised. Thus, both lasers have significant limitations.

This chapter presents results from an experimental demonstration of a novel, all-fibre, actively mode-locked dual-wavelength laser based on a nonlinear-optical loop mirror (NOLM) amplitude modulator. The NOLM is used to simultaneously mode-lock two cavities which employ chirped fibre Bragg gratings as end-mirrors to define the laser operating wavelengths. Since it acts a broadband reflector and has a response which is independent of the chosen input, the modulator may be used to simultaneously drive two cavities at arbitrary wavelength separations.

The chirped fibre Bragg gratings behave as lumped dispersive elements within the cavities and, as the dominant sources of dispersion, their use enables accu-

rate tailoring of the intracavity dispersion to produce controllable and well-defined pulse characteristics from each laser section. In addition, the use of Bragg reflectors allows the source operating wavelengths to be accurately and arbitrarily chosen across the whole erbium gain spectrum. The laser is shown to generate two synchronised pulse trains which can be independently tuned across the reflection band of each grating by varying the respective cavity length, a property which results in self-stabilisation under environmental variations. Finally, results are presented which show that the generated trains exhibit an extremely low level of inter-pulse-stream timing jitter.

This laser has clear advantages as a source for all-optical switching and WDM applications. Tunability and active mode-locking are achieved without the use of bulk-optic components, with a consequent increase in compactness and reliability. In addition, environmental stabilisation may be achieved without the need for accompanying active control system components. Finally, the use of a dual-cavity configuration enables wavelength choice to be made across the whole erbium gain spectrum, without the need for gain equalisation.

4.2 Experiment

A schematic of the experimental configuration is shown in fig. 4.1 and is based on that in ref. [133]. The NOLM modulator was constructed using a 40m standard fibre phase modulator section (dispersion of 17ps/(nm.km) at 1550nm) and switched at a repetition rate of 76MHz using pulses at 1064nm from a mode-locked Nd:YAG laser (τ_{fwhm} =90ps). The slightly increased switching window width of ~100ps was due to walk-off between the mode-locking laser and the operating wavelengths of the two cavities. The optimum average switching power required to drive the laser lay between a minimum of 100mW and a maximum of 140mW corresponding to modulation depths of between 85% and 99% respectively. This operating point, near the peak of the NOLM switching characteristic, ensured that fluctuations in the average power of the mode-locking pulse-stream were not transferred to the output of the laser. Although operation could be maintained at average switching powers as low as 60mW (modulation depth = 77%), the significant degradation of amplitude stability due to the slope of the NOLM switching characteristic at this input power severely limited the usefulness

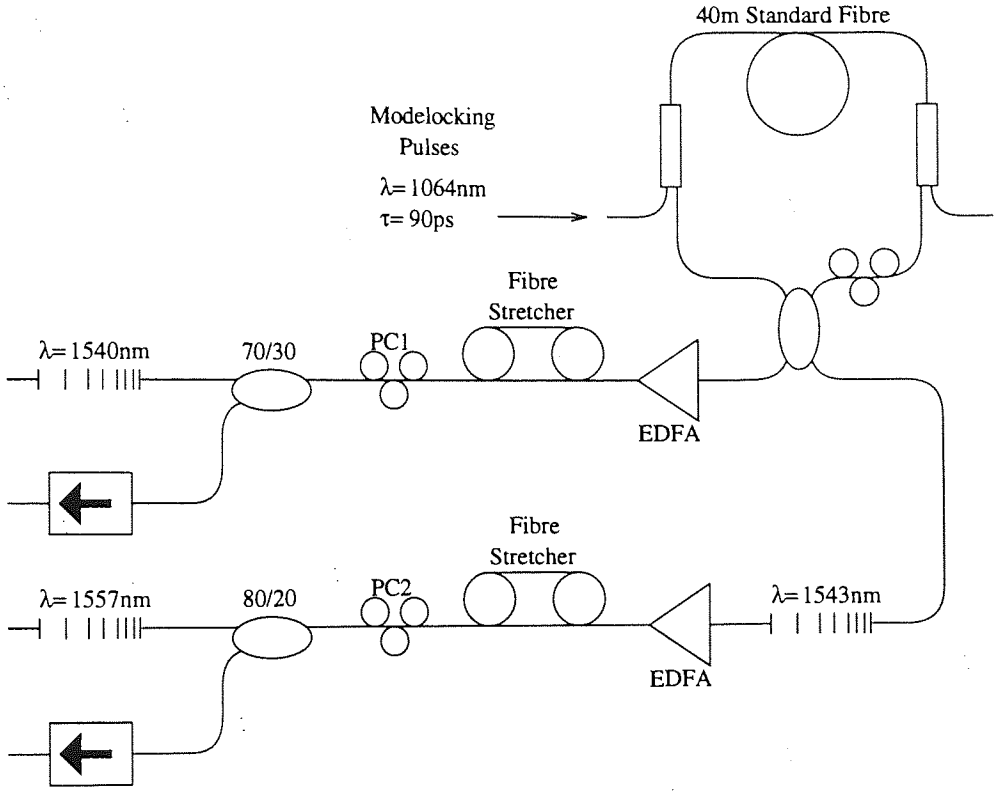

Figure 4.1: Schematic of dual-wavelength laser configuration.

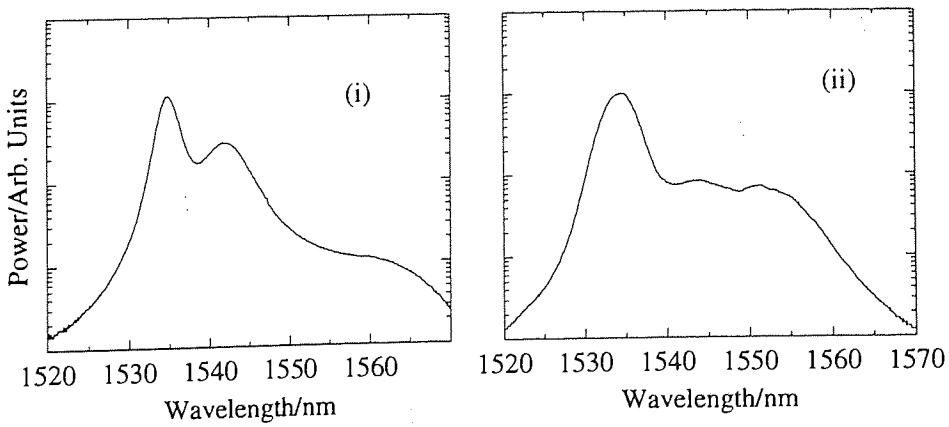

Figure 4.2: Spontaneous emission spectrum of (i) 1540nm cavity amplifier. (ii) 1557nm cavity amplifier.

of the laser.

The cavity operating wavelengths were specified using two, 4mm long, chirped fibre Bragg reflectors centred at 1540nm and 1557nm respectively, with bandwidths of 4nm and reflectivities of nominally 100%. For clarity, each cavity will be referred to the centre wavelength of its respective grating. Gain at 1557nm was provided by an EDFA pumped at 980nm using a CW Ti:sapphire laser and at 1540nm by a 980nm diode-pumped IRE-Polus amplifier module.

Figure 4.2 shows spontaneous emission spectra for the 1540nm and 1557nm cavity amplifiers respectively. It is clear from fig. 4.2 (ii) that leakage at 1540nm due to incomplete nonlinear reflection in the NOLM will receive significant gain from the amplifier in the 1557nm cavity. Indeed, this leakage was found to be capable of saturating the amplifier gain to such an extent that lasing was completely inhibited at 1557nm. This problem was alleviated by the inclusion of an additional strongly reflecting linear Bragg reflector centred at 1545nm, fabricated in hydrogenated standard fibre. The transmission profile of this grating is shown in fig. 4.3 . Strong gratings, *i.e.* reflectors in which the ratio of the induced refrac-

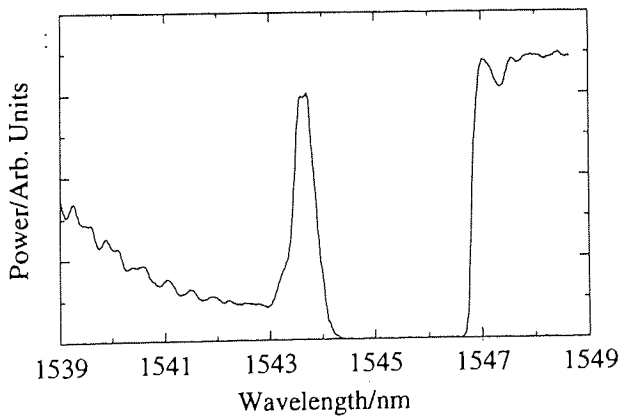

Figure 4.3: Reflection profile of intercavity grating isolator.

tive index change to the refractive index of the fibre, $\delta n/n$ is $\sim 10^{-3}$, suffer from radiation mode-coupling into the cladding [134]. This effect manifests itself as a wavelength dependent loss on the short wavelength side of the grating transmission profile [135] and can be clearly seen in fig. 4.3. By making positive use of this transmission loss, which was measured to be 7.4dB at 1540nm, the leakage signal was attenuated before its single pass through the amplifier allowing the 1557nm

cavity to run normally. An equivalent grating was not required in the 1540nm cavity due to the reduced erbium gain at 1557nm, as seen from fig. 4.2 (i). The low level of flourescence beyond 1545nm is consistent with low concentrations of alumina in the glass (page 240-241, ref [136]).

A summary of typical mode-locked pulse parameters is shown in fig. 4.4. Figure 4.4 (i) shows a typical autocorrelation and sech^2 fit for the 1540nm pulse stream and fig. 4.4 (ii) the corresponding spectrum. The laser produces a stable train of near transform-limited ($\Delta\nu\Delta\tau = 0.30$) sech^2 pulses of duration 5.6ps, in this case centred at 1540.3nm. Figures 4.4 (iii) and (iv) show the corresponding pulse characteristics for the 1557nm cavity. The measured pulse width in this case was 11.5ps at 1554.9nm, with a time-bandwidth product, $\Delta\nu\Delta\tau$, of 0.54. It was observed that when the 1540nm cavity was not operating, the measured pulse width increased to 13.5ps and the time-bandwidth product fell to 0.5. Figure 4.5 (i) shows an autocorrelation and sech^2 fit of these pulses and fig 4.5 (ii) the corresponding pulse spectrum. Although the autocorrelation shows a good fit to a sech^2 profile, it is clear from the time-bandwidth product that the pulses are strongly chirped. This may be attributed to the cavity operating point which was close to the edge of the grating reflection band where pulses receive excess chirp. This operating point was chosen initially since it was the only point on which the cavity would sustain a full train of pulses. The increase in time-bandwidth product when the two lasers are running simultaneously is most likely due to the influence of cross-phase-modulation (XPM) from the shorter, higher energy pulses at 1540nm.

The output wavelength of an individual cavity can be dispersion-tuned by using its intracavity fibre stretcher to vary the overall cavity length. When stretched or relaxed, the cavity compensates by adjusting its wavelength. Since the chirped grating end-mirror reflects different wavelengths along its length, the new wavelength is such that the change in effective reflection point exactly matches the change due to the fibre stretcher. This characteristic also has the added benefit of making the cavity mode-locking stable under environmental fluctuations. A constant repetition rate is, thus, maintained by small variations in wavelength. When the operating wavelength is tuned to the centre of the 1557nm grating using the intracavity fibre stretcher as described, the laser generates near bandwidth-limited pulses of $\sim$6ps duration.

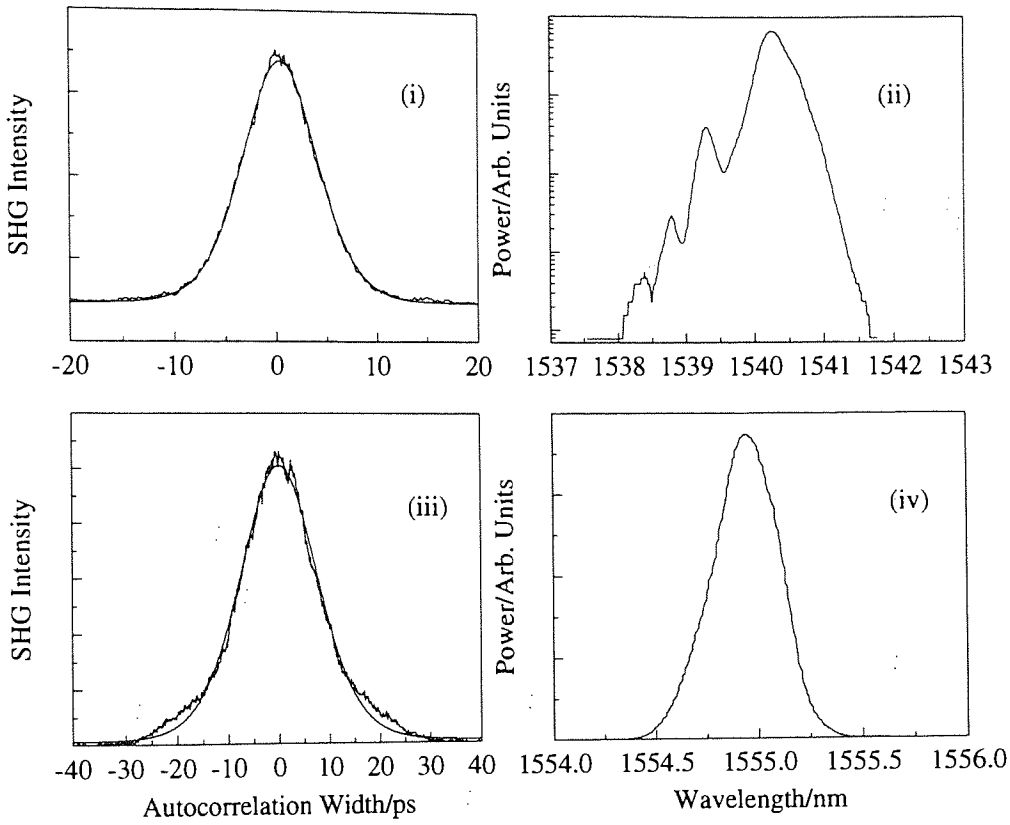

Figure 4.4: 1540nm cavity (i) autocorrelation and sech^2 fit. $\Delta\tau$ =5.6ps (ii) spectrum. λ =1540.3nm, $\Delta\lambda$ =0.43nm, $\Delta\nu\Delta\tau$ =0.30. 1557nm cavity (iii) autocorrelation and sech^2 fit. $\Delta\tau$ =11.5ps (iv) spectrum. λ =1554.9nm, $\Delta\lambda$ =0.38, $\Delta\nu\Delta\tau$ =0.54.

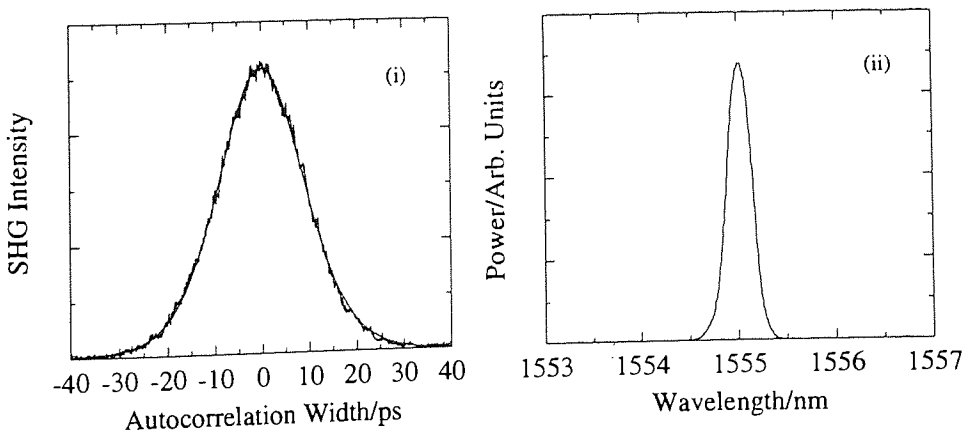

Figure 4.5: 1557nm cavity operating alone (i) autocorrelation and sech^2 fit. $\Delta\tau$ =13.5ps. (ii) spectrum. λ =1555nm, $\Delta\lambda$ =0.3nm, $\Delta\nu\Delta\tau$ =0.5.

Fig. 4.6 shows an analogue oscilloscope trace taken under these conditions. The amplifier gain is not sufficiently high to maintain a full soliton pulse train in this operating regime due to the increase in pulse energy which is required to support it. This quantisation of pulse energy is well known and has been observed in both active and passively mode-locked soliton lasers [137, 138] which have a "preference" for operating in defined soliton units with pulse widths defined by the intracavity dispersion [139].

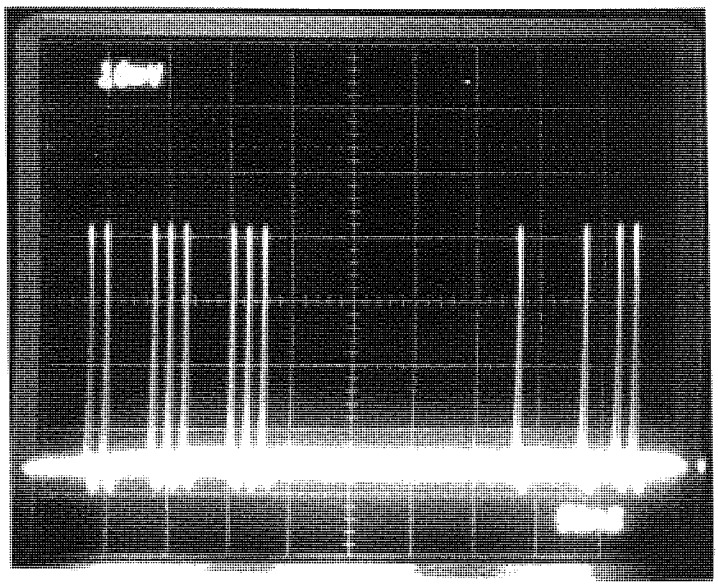

Figure 4.6: Oscilloscope trace showing pulse drop-out.

Propagating pulses experience periodic exponential gain and lumped loss on successive cavity round trips. When the period of these perturbations is on the order of the soliton period for the generated pulse, energy is shed in the form of a dispersive wave to enable the perturbed pulse to evolve to a soliton. This dispersive wave is initially shed with the same phase as the soliton, but each frequency component then propagates at a phase velocity defined by the dispersion characteristics of the laser as a whole. On successive round trips the dispersive wave interferes destructively with the soliton except at wavelengths which accumulate a relative phase shift of an integer multiple of 2π. This gives rise to a series of distinct spectral sidebands at specific wavelength offsets from the pulse central wavelength [140, 141, 142]. Sideband generation represents a loss proportional to the amplitude of the soliton spectrum at the sideband wavelength and, thus, limits the pulse width supported by the cavity since, for a

given repetition rate, the available energy per pulse is fixed [143].

Correspondingly, it was observed that when the available pump power was increased, the laser did not produce narrower pulses, which might be expected for an increase in intracavity energy, but resulted only in more energy being shed into the spectral sidebands. Similarly, reduced pump power did not cause a decrease in pulse width, but as stated above, pulses were successively dropped out so that the remaining pulses could propagate at the cavity's limiting pulse width. This problem can be overcome by simply increasing the intracavity gain, in order that more pulses may be sustained, or by increasing the intracavity dispersion and thereby increasing the cavity's steady-state pulse width. Since the latter is dominated by the chirped grating end-mirrors, this may also be achieved by appropriate grating design. The effect of grating dispersion on the overall intracavity dispersion is discussed in more detail in the next section.

Fig. 4.7 shows the 1557nm cavity pulse parameters with the Ti:Sapphire pump reconfigured to produce a full pulse train in the centre of the grating reflection band. In this case the laser produces a complete train of transform limited ($\Delta\nu\Delta\tau$ =0.37) sech^2 pulses of 6.1ps duration centred at 1556nm.

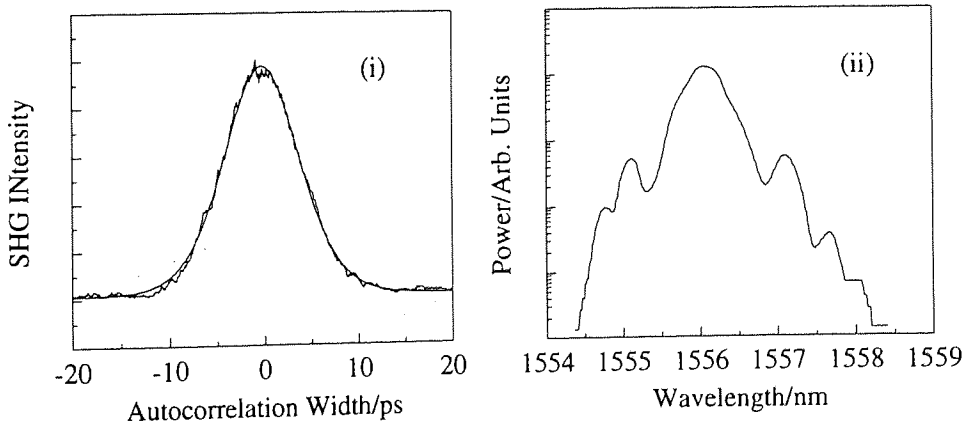

Figure 4.7: 1557nm cavity (i) autocorrelation and sech^2 fit. $\Delta\tau$ =6.1ps (ii) spectrum. λ =1556nm, $\Delta\lambda$ =0.49nm, $\Delta\nu\Delta\tau$ =0.37.

4.3 Intracavity Dispersion Measurement

Having detailed the temporal and spectral characteristics of the pulses generated by this configuration, the current section goes on to deal with experimental

measurement of intracavity dispersion. It is found that the average dispersion of each cavity is dominated by its respective chirped grating end-mirror. Thus, as discrete components, chirped fibre Bragg gratings provide an attractive alternative to current methods of intracavity dispersion adjustment involving the insertion of appropriate of lengths of fibre, simplifying the tailoring of laser pulse characteristics.

4.3.1 Measurement of Grating Dispersion

A schematic of the configuration used to measure the reflection profiles and individual dispersion characteristics of each grating is shown in fig. 4.8. The signal from a HP8186B tunable CW laser source was fed into a Lithium Niobate Mach-Zehnder amplitude modulator which was sinusoidally driven at a frequency of 1GHz using a signal derived from a HP8505A network analyser. 50% of the reflected signal was detected using a 22GHz detector and light from the 10% arm of the 90/10 coupler was detected using a power meter to simultaneously record the grating reflection profile. The electrical signal from the 22GHz photodiode was sent to the network analyser where its phase was compared with the signal used to drive the modulator.

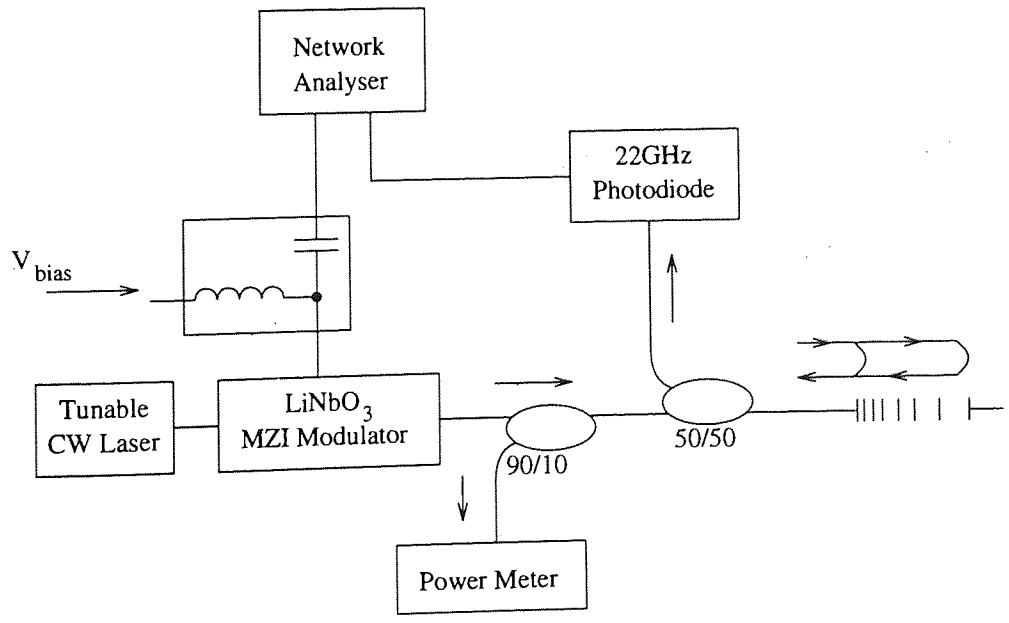

Figure 4.8: Schematic of experimental configuration for simultaneous measurement of grating phase and reflection profiles.

Since the grating reflects different wavelengths along its length, it follows that, as the laser source wavelength is tuned across the grating reflection band, the phase of the reflected signal with respect to the modulator drive signal will vary. For a perfect linearly chirped grating this phase differential would scale linearly with wavelength. Thus, by recording the relative phase of these two signals over the reflection band of the grating, the phase profile, and hence the grating dispersion characteristic, can be plotted.

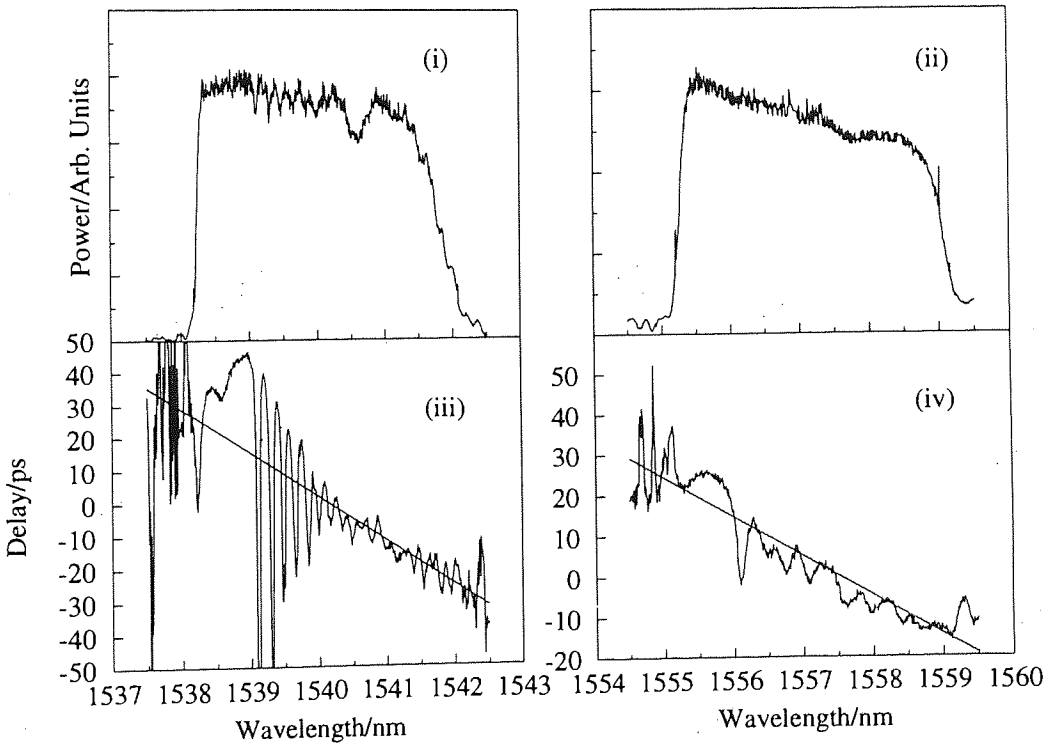

Figure 4.9: Reflection profile of (i) 1540nm grating. (ii) 1557nm grating. Phase profile of (iii) 1540nm grating. (iv) 1557nm grating.

Figures 4.9 (i) and (ii) show the reflection profiles of the 1540nm and 1557nm gratings respectively and figures 4.9 (iii) and (iv) the corresponding phase profiles together with linear curve fits recorded using 0.01nm wavelength steps. Using the gradients calculated from each fit the average grating dispersions were found to be +13.4ps/nm and +9.7ps/nm at 1540nm and 1557nm respectively. It can be seen that the phase plots of both reflectors exhibit significant phase "ripple", a feature which is characteristic of gratings with sharp reflection band edges [144, 145].

Both profiles, therefore, deviate significantly from the expected linear relationship for a perfect chirped grating, and, ultimately, it would be expected that these would translate into localised dispersion variations.

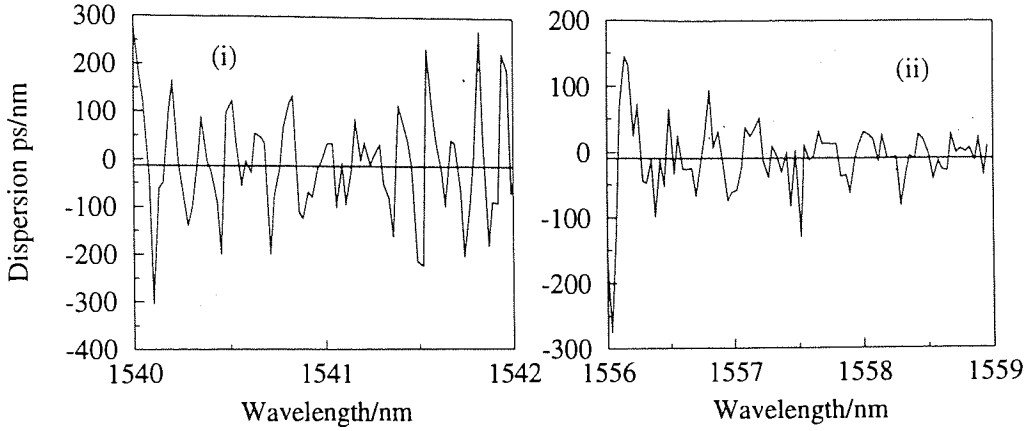

Figure 4.10: Grating dispersion characteristics. (i) 1540nm grating. (ii) 1557nm grating. Horizontal lines show average dispersions calculated from phase profiles.

The grating dispersion profiles were derived by differentiation of the respective phase profiles and the results for the smoother central regions of each reflection band are shown in figure 4.10. The horizontal lines show the average dispersions of each grating quoted above. As expected, the magnitude and sign of the dispersion is a strong function of wavelength and, consequently, it was observed that both cavities could only be step-wise tuned, an observation which is consistent with these strong localised dispersion variations. Thus, the cavity mode-locking was found to drift off over time pointing to the inability of the cavities to self-stabilise. This difficulty is easily overcome, however. Hill has shown [145, 146], that apodisation of the grating reflection profile, *i.e.* modulation of the amplitude of the photoinduced refractive index change to produce a bell-like reflection band, leads to a reduction in the phase ripple, and hence to a more linear dispersion characteristic. Thus, by using apodised gratings, continuous tunability and the accompanying self-stabilisation would occur. Inclusion of such gratings was not attempted, however, due to in-house fabrication constraints.

Only one soliton supporting operating point was found in the 1540nm cavity when the wavelength was tuned to 1540.3nm as shown in fig 4.4 (i) and (ii). In regions where strong ringing in the phase profile was observed the cavity was seen to generate gaussian pulses of ~20ps duration, a result consistent with an

intracavity dispersion in the normal regime.

Having examined the individual dispersion characteristics of each grating, two techniques for measurement of the overall intracavity dispersion are described. The first derives average dispersion measurements by plotting the change in the mode-locked operating wavelength of the individual cavities with cavity length, and the second enables measurement of local cavity dispersions by using the positions of the spectral sidebands present on the mode-locked optical spectra.

4.3.2 Measurement of Intracavity Dispersion by Wavelength Tuning

As already described, the cavities in this configuration may be dispersion tuned by stretching of the individual intracavity fibre stretchers. In order to maintain a constant repetition rate, variations in cavity length are offset by a wavelength adjustment to a value with an effective grating reflection point which exactly compensates for the change. Thus, the intracavity dispersion may be inferred by systematically varying the cavity length and plotting the corresponding change in round trip delay time against mode-locked wavelength.

The first stage involves calibration of each fibre stretcher in order that micrometer readings may be translated into actual cavity length variations. This procedure is performed with the cavities running CW, *i.e.* with the mode-locking signal absent and the loop mirror modulator biased into reflection, and viewing the signal on a microwave spectrum analyser. When viewed in this way, spectral peaks due to mode-beating can be seen at the cavity fundamental frequency and its respective harmonics, values which change with cavity length according to the following, readily derived, equation,

$$\Delta L = \frac{cN\Delta\nu_N}{2n\nu_N^2} \tag{4.1}$$

where ΔL is the change in cavity length, $\Delta\nu_N$ is the corresponding change in frequency of the Nth harmonic of the cavity round trip frequency and ν_N is the frequency of the Nth harmonic. Thus, the change in frequency of a high harmonic of the cavity round trip frequency may be used to determine the actual change in cavity length for a given change in fibre stretcher micrometer reading, and, hence, converted into a change in round trip delay time.

Having calibrated the fibre stretchers, the next step is to record the change in mode-locked wavelength with round trip delay. The results from this procedure are shown in fig. 4.11 together with the corresponding linear regression fits.

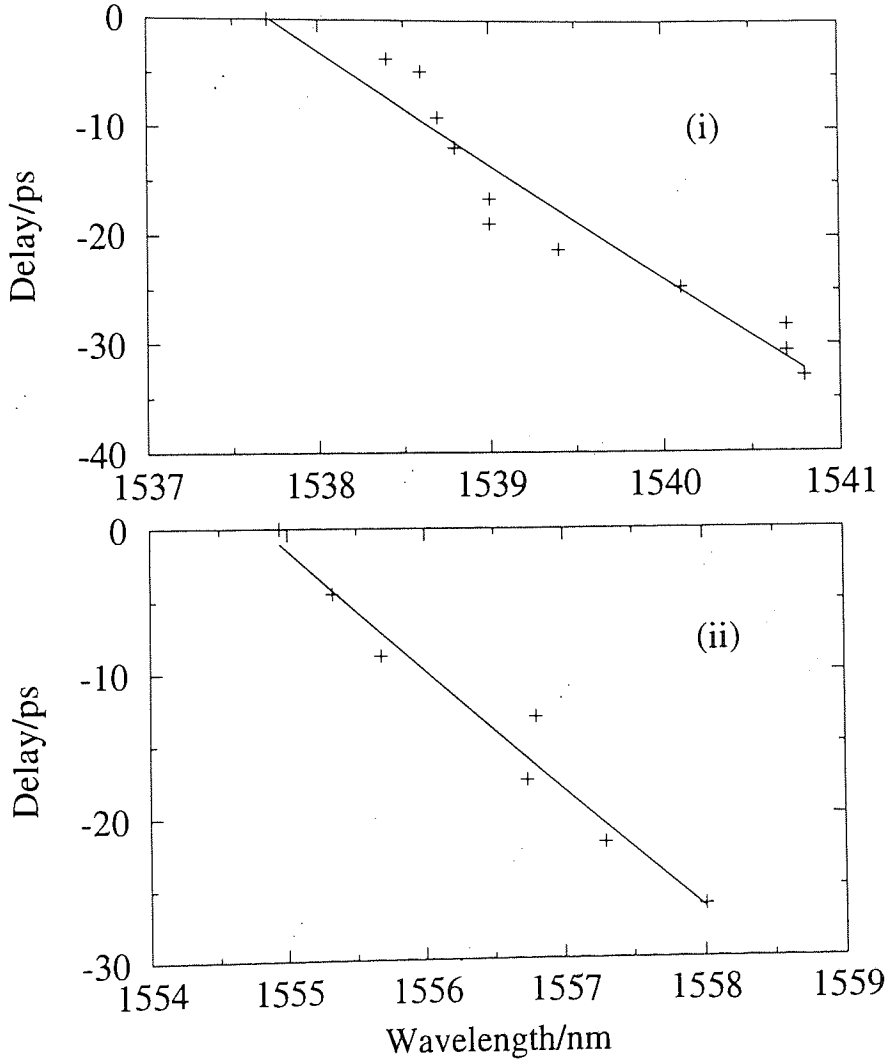

Figure 4.11: Plot of change in cavity round trip delay time against mode-locked operating wavelength and corresponding linear curve fit for (i) 1540nm cavity. (ii) 1557nm cavity.

The average dispersions calculated from the gradients of the linear curve fits are +10.5ps/nm and +8.3ps/nm at 1540nm and 1557nm respectively. Both plots in fig. 4.11 show the stepwise nature of the dispersion tuning of each cavity and indicate the significant effect which grating dispersion variations have on the localised intracavity dispersion.

Is is also clear from the similarity of these average values to the measured values for each grating of +13.4ps/nm and +9.7ps/nm that the overall intracavity dispersion is dominated by the end-mirrors. Thus, chirped gratings facilitate accurate control of both operating wavelength and intracavity dispersion. In addition, a change of grating orientation allows the sign of the average dispersion to be varied. Figure 4.12 (i) shows a typical autocorrelation, together with a gaussian fit, of pulses from the 1557nm cavity with the grating reversed, and fig. 4.12, the corresponding spectrum. The pulses can be seen to be a good fit to a gaussian autocorrelation function, with a measured pulse width, $\Delta\tau$, of 27ps and spectral width, $\Delta\lambda$, of 0.4nm ($\Delta\nu\Delta\tau = 1.3$). The measured average dispersion in this configuration using the technique outlined above was -8.2ps/nm. It is therefore conceivable that the same laser could be configured to produce both $sech^2$ and gaussian pulses simultaneously, should such a mode of operation be required.

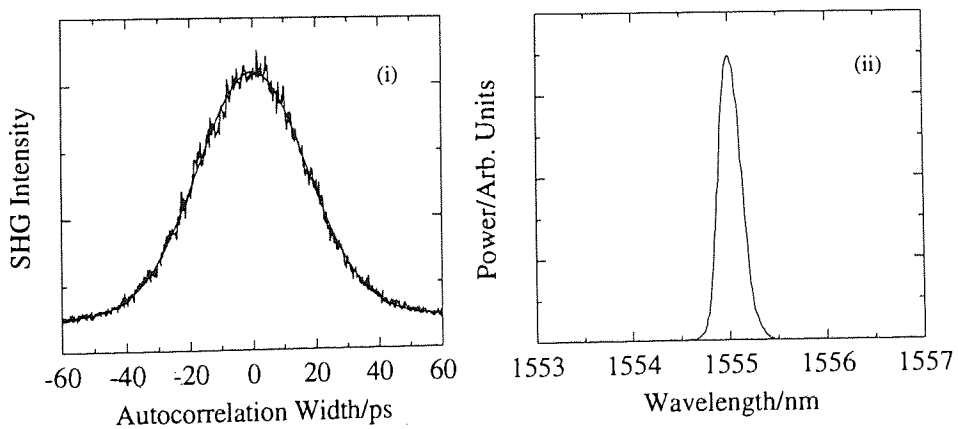

Figure 4.12: 1557nm cavity (i) autocorrelation and gaussian fit. $\Delta\tau$ = 27ps, (ii) spectrum. $\Delta\lambda$ = 0.4nm, $\Delta\nu\Delta\tau$ = 1.3. Cavity in normal dispersion.

4.3.3 Measurement of Intracavity Dispersion Using Spectral Sidebands

Since sideband generation is a resonant effect dependent on the accumulated phase differential between the dispersive wave and the underlying soliton, it follows that sideband position is determined by intracavity fibre dispersion. The

dispersive wave propagation constant is given by [147],

$$\beta_d(\omega) = \beta_0 + \beta_1\Delta\omega + \frac{1}{2}\beta_2\Delta\omega^2 + \frac{1}{6}\beta_3\Delta\omega^3 \tag{4.2}$$

where β_2 and β_3 are the second and third order dispersions per unit length and $\Delta\omega = \omega - \omega_0$ is the angular frequency offset from the soliton central frequency ω_0. The equivalent relation for the soliton, neglecting third order dispersion, is given by

$$\beta_s(\omega) = \beta_0 + \beta_1\Delta\omega - \frac{1}{2}\beta_2\tau_0^{-2} \tag{4.3}$$

where τ_0 is the soliton pulse width. The resonance condition, requires that the relative phase differential,

$$\varphi_s - \varphi_d = 2\pi N = L(\beta_s - \beta_d) \tag{4.4}$$

where N is an integer, β_s is the soliton propagation constant and β_d is the propagation constant for the dispersive wave. Substituting from equations 4.2 and 4.3 into 4.4 gives,

$$N = \frac{1}{4\pi}L\beta_2(\Delta\omega_N^2 + \tau_0^{-2}) - \frac{1}{12\pi}L\beta_3\Delta\omega_N^3 \tag{4.5}$$

where $L\beta_2$ and $L\beta_3$ are the total second and third order fibre dispersions for the cavity. When rewritten as a function of the form

$$N = A(\Delta\omega_N^2 + B\Delta\omega_N^3 + C) \tag{4.6}$$

it is clear that the total second and third order dispersions can be derived from the quadratic and cubic coefficients of a cubic curve fit to a plot of sideband order against angular frequency offset from the soliton central frequency. Thus, by comparison of equations 4.5 and 4.6 the second and third order dispersions can be shown to be,

$$L\beta_2 = -4\pi A \tag{4.7}$$

and

$$L\beta_3 = -12\pi AB \tag{4.8}$$

Figures 4.13 (i) and (ii) show these plots together with cubic fits for the 1540nm and 1557nm cavities giving second order dispersions of +12.8ps/nm

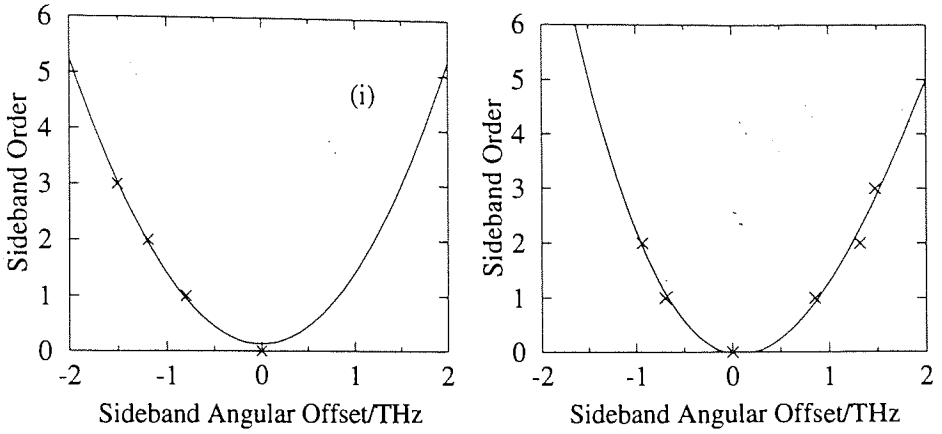

Figure 4.13: Sideband order against angular frequency offset and corresponding cubic fits for (i) 1540nm cavity, (ii) 1557nm cavity.

and +17.7ps/nm at 1540nm and 1557nm respectively. Since the operating pulse widths were relatively long the calculation of third order dispersion proved unreliable due to its very low contribution to overall pulse dispersion.

From these values it is clear that the dispersion "seen" by pulses in each cavity is close to the individual measured average intracavity dispersions giving further evidence of the potential of chirped gratings as dispersion control devices. It is also evident that, although grating dispersion variations may have a detrimental effect on source tunability, the use of solitons ensures that they are not critical to the stability of the overall pulse parameters. It is probable that steady-state pulse width compensates for the strong local wavelength dependence of the grating dispersion by adjusting to a value with a spectral width which is wide enough to straddle the intracavity dispersion perturbations, so that the underlying local average is seen.

4.4 Analysis of Jitter Performance

Having detailed the individual intracavity dispersion characteristics of this configuration, the present section provides an analysis of the inter-pulse-stream jitter between each pulse train, a value of prime importance in determining the maximum switching rate at which this configuration may be applied. Results from

two techniques are presented. The first is a temporal analysis obtained using a digital sampling oscilloscope, and the second a microwave spectrum analysis of each pulse train.

4.4.1 Temporal Measurement of Inter-Pulse-Stream Timing Jitter

The first jitter measurement technique uses the statistics package of a HP54124T digital sampling oscilloscope. By triggering the scope with an appropriate reference signal, the jitter of a source which is synchronised to this reference may be obtained using the instrument's internal statistics package. Thus, relative (inter-pulse-stream) timing jitter between each pulse train may be estimated by triggering the scope using pulses from one cavity, and viewing the other. The absolute jitter of each pulse train *i.e.* the jitter of each relative to the mode-locking signal, may also be obtained by using the mode-locking pulse train as a trigger and viewing each cavity separately.

Inter-pulse-stream jitter was estimated by triggering the scope with the 1557nm pulse stream, detected using a 22GHz photodiode, and viewing the 1540nm train, detected using a 45GHz Newfocus 1014 photodiode, on infinite persist. The resultant scope trace after 1000 samples is shown in fig. 4.14 (i). The measured standard deviation jitter level under these conditions was 800±50fs. In order to null any jitter caused by the measurement system, the 1540nm signal was viewed while triggered against itself. The result is shown in fig. 4.14 (ii). The measured standard deviation jitter in this case was 700±50fs. The relative standard deviation jitter level may be calculated from these measurements using the relationship

$$\sigma_{rel} = \sqrt{\sigma_{meas}^2 - \sigma_{inst}^2} \tag{4.9}$$

where σ_{meas} is the measured relative standard deviation jitter, and σ_{inst} is the standard deviation jitter due to the instrument. Using the upper and lower boundaries of the measured value ranges (σ_{meas}=850fs and σ_{inst}=650fs) a maximum standard deviation inter-pulse-stream jitter level of 550fs is obtained. It is clear, however, that the source relative-jitter level lies extremely close to the resolution limit of the instrument. The reliability of the value calculated is therefore questionable.

Although the relative jitter level gives a measure of the jitter between the

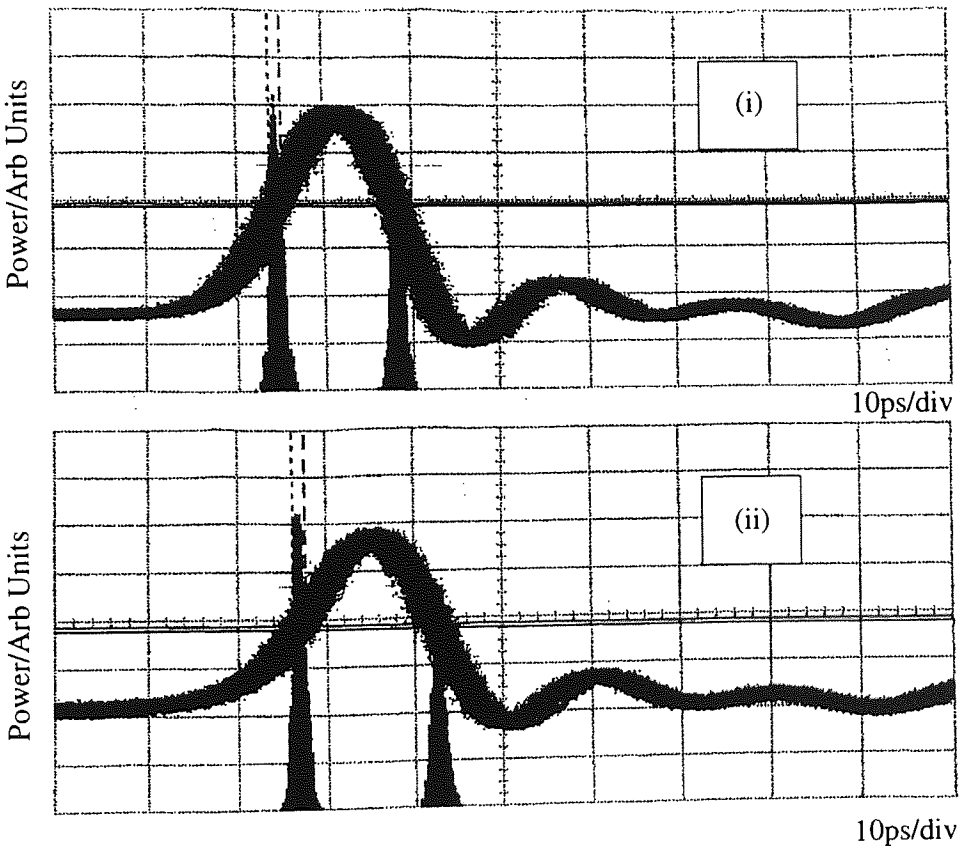

Figure 4.14: Sampling oscilloscope trace after 1000 samples: (i) 1557nm trigger, 1540nm signal. σ_{jitter} = 800±50fs. (ii) 1557nm trigger, 1557nm signal. σ_{jitter} = 700±50fs.

two pulse streams, no indication is given of the absolute jitter of each train. This value was estimated by triggering the scope with the YAG mode-locking pulses at 1064nm exiting from the NOLM modulator and viewing each fibre laser pulse train separately. Figures 4.15 (i) and (ii) show scope traces recorded after 1000 samples of the 1540nm and 1557nm pulse trains, giving measured standard deviation jitter levels, corrected for the instrument resolution limit, of 1.66ps at both wavelengths.

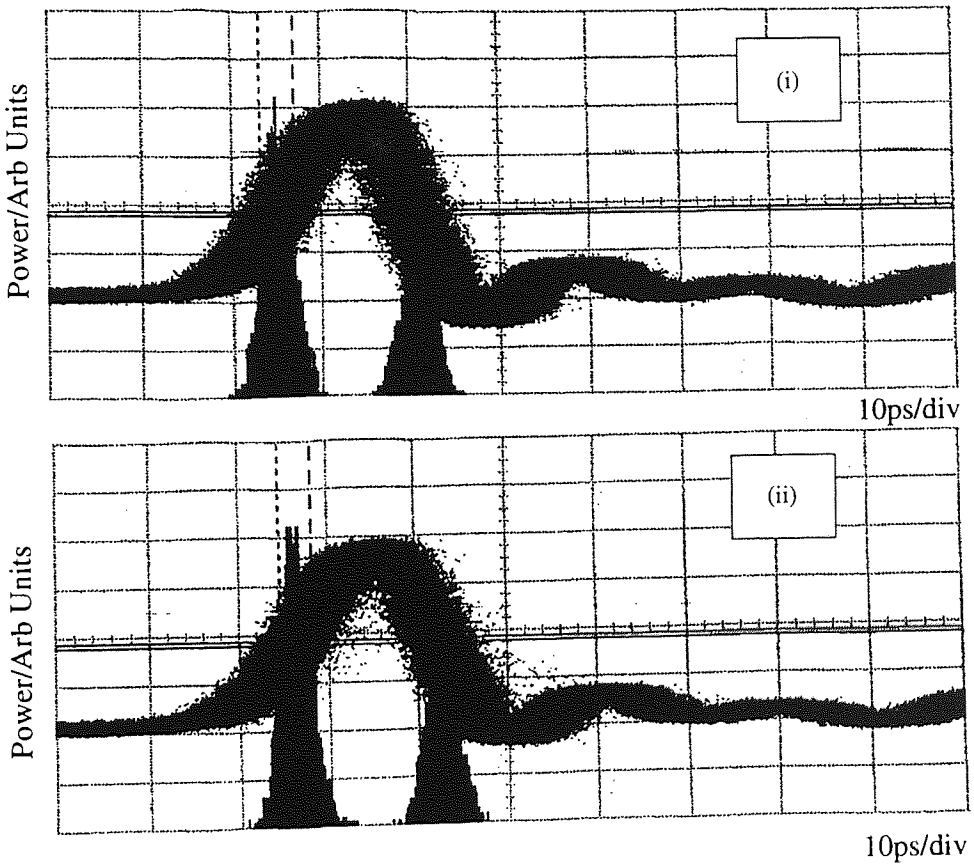

Figure 4.15: Sampling oscilloscope trace after 1000 samples with YAG modulator trigger signal: (i) 1540nm signal. $\sigma_{jitter} = 1.66$ps. (ii) 1557nm signal. $\sigma_{jitter} = 1.66$ps.

Further correction must be made to these measurements for the contribution to timing jitter caused by the high level of amplitude noise present on the YAG mode-locking signal. This correction was not required in the previous measurements since the flat peak of the sinusoidal switching response of the NOLM modulator minimises transfer of mode-locker amplitude fluctuations to the fibre laser cavities. The standard deviation of the amplitude noise, σ_{amp}, is derived

from a histogram of sampled amplitudes over an narrow time window at the peak of the photodiode signal. The resultant temporal jitter, $\sigma_j(amp)$, is obtained using the slew rate at the half maximum point of the oscilloscope trace [148].

The YAG signal was split using a 90/10 coupler, and the 10% portion was used to trigger the oscilloscope, while the 90% portion was viewed on infinite persist. The result after 1000 samples is shown in fig. 4.16. The measured standard deviation amplitude noise in this case is 2.35mV, however, on consecutive measurements, values were found to vary from this lowest value up to a maximum of 4mV. When combined with the measured slew rate of 0.475ps/mV these two values imply a jitter contribution due to amplitude fluctuations, $\sigma_j(amp)$, of between 1.2ps and 1.9ps. Using this value, a final value of absolute jitter for the fibre laser pulse trains is obtained of between 0ps and 1.1ps at each wavelength. Thus, this technique also fails to give a reliable estimate of absolute jitter.

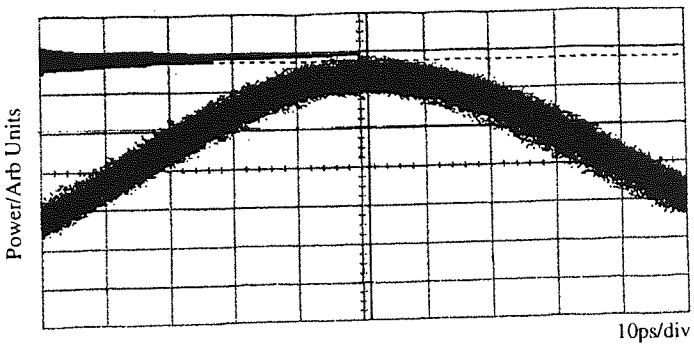

Figure 4.16: Sampling oscilloscope trace after 1000 samples for determination of YAG amplitude noise. $\sigma_{amp} = 2.35$mV.

In summary, it can be concluded that the inter-pulse-stream jitter level of this configuration is too low to be reliably quantified using this temporal characterisation technique. It is therefore necessary to utilise an alternative technique to infer more accurate jitter information.

4.4.2 Measurement of Jitter Using Microwave Spectrum Technique

Von der Linde has shown that information on the jitter content of a mode-locked source may be obtained by detecting its pulse train using a fast photodiode and examining its microwave spectrum [149], a technique which has, to date, been

used to characterise various mode-locked sources such as F-centre lasers [150], Nd:YAG lasers [151, 152], and mode-locked dye and argon ion lasers [148, 149].

Fig. 4.17 shows an illustration of the microwave spectrum which might be expected from a mode-locked pulse train. The spectrum consists of a series of discrete frequency bands spaced at the repetition rate $1/T$ Hz where T is the pulse period. Each frequency band consists of three contributions: a δ-function (i) which corresponds to the contribution from the perfect noise free pulse train; a pedestal of constant intensity (iii) corresponding to the contribution from amplitude fluctuations; and a contribution (ii) which increases as the square of the harmonic number corresponding to the contribution from temporal jitter and pulse width fluctuations [153]. For a fibre laser, the contribution from pulse

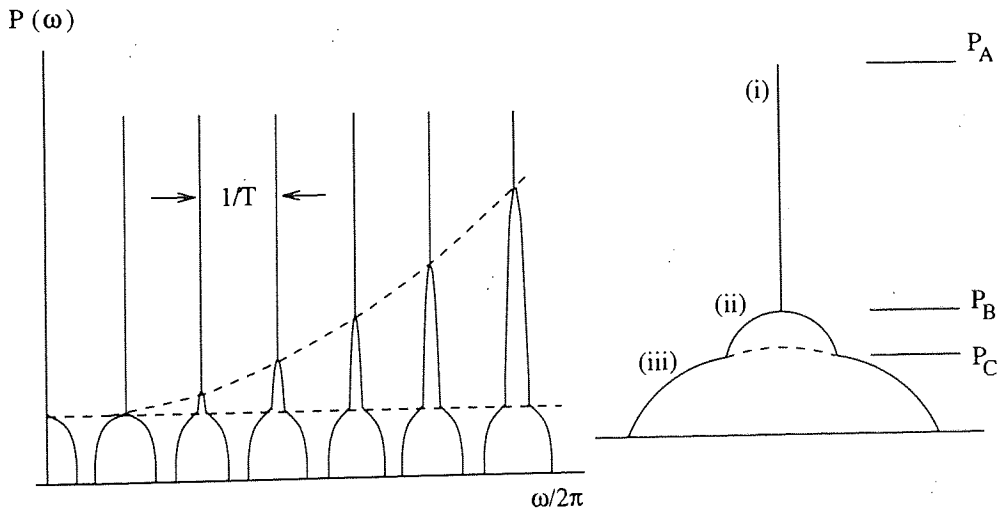

Figure 4.17: Illustration of typical microwave spectrum of a mode-locked pulse train.

width fluctuations can be neglected due to the soliton nature of the pulses generated. Thus, pulse energy fluctuations can be obtained from analysis of the fundamental microwave component and since the jitter contribution increases as the square of harmonic number, jitter information can be isolated by examination of a high harmonic of the microwave spectrum. From the analysis of von der Linde, the pulse energy fluctuations are given by the equation,

$$\Delta E/E = \sqrt{\frac{(P_C/P_A)_0 \Delta f_A}{\Delta f_{res}}} \tag{4.10}$$

where $(P_c/P_a)_0$ is the power ratio at the fundamental (see fig. 4.17), Δf_A is the full width half maximum spectral width of the noise pedestal and Δf_{res} is the resolution bandwidth of the instrument.

Similarly, the standard deviation jitter level is given by,

$$\Delta t/T = \frac{1}{2\pi n}\sqrt{\frac{(P_B/P_A)_n \Delta f_J}{\Delta f_{res}}} \tag{4.11}$$

where $(P_B/P_A)_n$ is the power ratio at the nth harmonic, and Δf_J is the full width half maximum spectral width of the jitter pedestal. Thus, using eqn. 4.11, an estimate of the inter-pulse-stream jitter can be made by combining the values calculated from the individual microwave spectra of each cavity.

Figures 4.18 and 4.19 provide summaries of the microwave measurements taken from the 1540nm and 1557nm cavities respectively.

Inspection of figures 4.18 (i) and 4.19 (i) show that the 66th harmonics of both have significant pedestals, features which were also found to be present on the fundamental components of both pulse trains and which are therefore due to pulse energy fluctuations. Using eqn. 4.10, noise levels of 0.6% and 1.7% are calculated at 1540nm and 1557nm respectively. The higher level at 1557nm can be attributed to the use of the Ti:Sapphire pump laser used in this cavity. In addition, it was observed that these noise levels could be minimised by adjustment of the intracavity polarisation controllers. Figures 4.18 (ii) and 4.19 (ii) show the same microwave spectra under these conditions giving minimised noise levels of 0.1% and 0.2% respectively. This observation, together with the presence of pronounced sidebands at ±25kHz, clearly visible on spectra from both cavities and due to gain relaxation oscillations, is in agreement with results from the mode-locked erbium fibre ring laser of Davey *et. al.* [154]. Although the origin of this polarisation dependence is unclear, it may be caused by detuning away from the polarisation state which gives maximum XPM between the switching pulse-stream and the intracavity pulses.

Applying eqn. 4.11 to the spectra of figures 4.18 (iii) and 4.19 (iii) gives estimated standard deviation jitter levels of 390fs and 480fs at 1540nm and 1557nm respectively. Similarly, the mode-locking signal microwave spectrum shown in fig. 4.20 yields an estimated standard deviation jitter level of 430fs. It is evident, therefore, that the low frequency jitter components of each source are largely

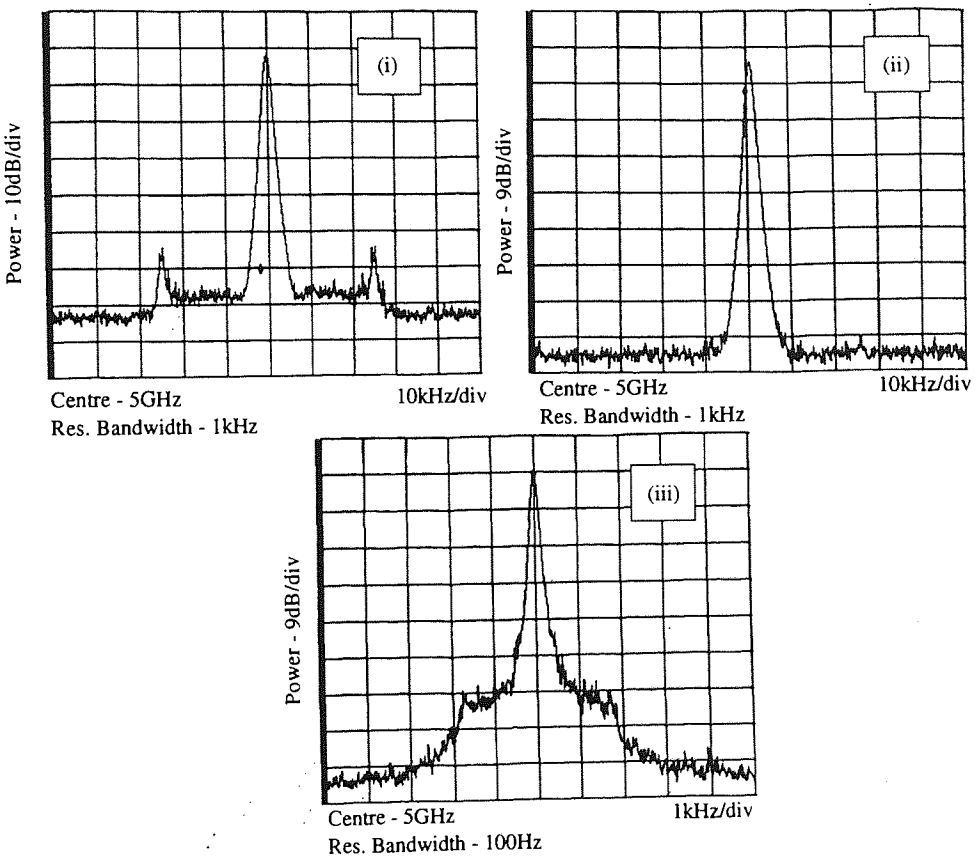

Figure 4.18: Microwave spectrum summary from 1540nm cavity. (i) 66th harmonic over 100kHz span. (ii) 66th harmonic over 100kHz span and (iii) 10kHz span with pulse energy fluctuations minimised. $\sigma_{jitter} = 390fs$.

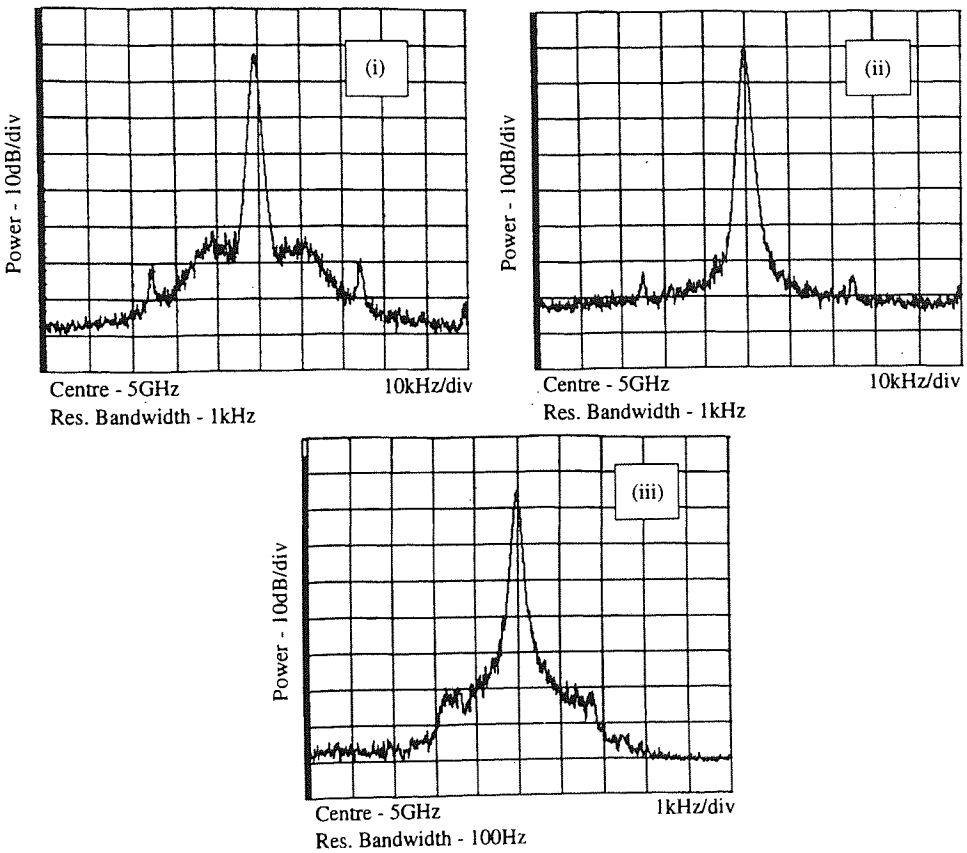

Figure 4.19: Microwave spectrum summary from 1557nm cavity. (i) 66th harmonic over 100kHz span. (ii) 66th harmonic over 100kHz span and (iii) 10kHz span with pulse energy fluctuations minimised. $\sigma_{jitter} = 480fs$.

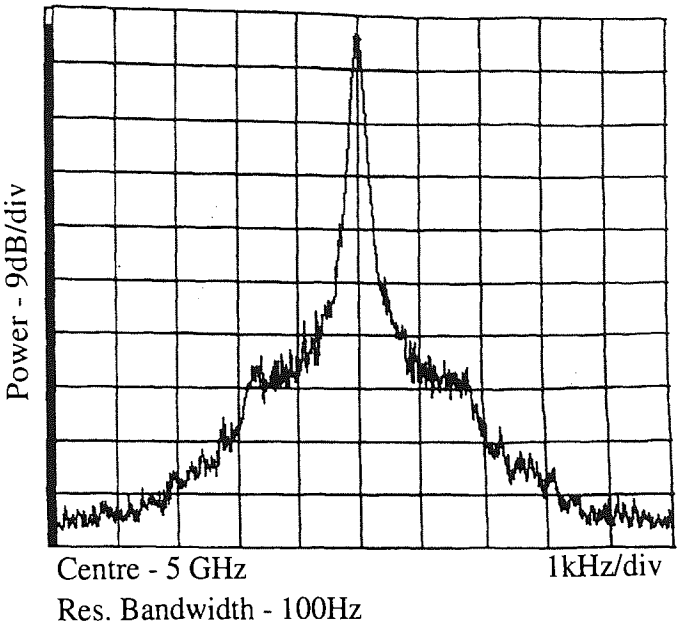

Figure 4.20: 66th harmonic of Nd:YAG mode-locking signal over 10kHz span. $\sigma_{jitter} = 430fs$.

dominated by the phase noise of the mode-locking laser. This observation is consistent with the predictions of Hjelme and Mickelson [155] for actively mode-locked lasers in which the spontaneous decay time is much longer than the round trip delay, a condition which applies in this configuration – round trip delay of $0.4\mu s$ and spontaneous emission decay time for Er doped fibre of 10ms (page 223, [136]).

The resultant inter-pulse-stream jitter level can then be calculated using the relationship

$$\sigma_{ipsj} = \sqrt{\sigma^2_{1540nm} + \sigma^2_{1557nm}}$$

giving a value for σ_{ipsj} of 620fs.

Jinno has shown that, for a dual-wavelength NOLM, a prediction of the theoretical maximum switching rate can be derived when the inter-pulse-stream jitter of the interacting pulse streams is known [128, 129]. For a switching window of width W, a total jitter level of less than W/12 is required for a bit error rate better than 10^{-9}. Using the jitter level, σ_{ipsj}, of 620fs the switching window duration, τ_s, required to meet this criterion is found to be 7.5ps, giving a corresponding maximum switching rate, $1/\tau_s$, of 133GBit/s.

4.4.3 *Comparison With Other Sources*

As mentioned in the introduction, a number of techniques exist for the generation of ultrashort pulses. These include gain switching of DFB lasers with external fibre compression [128, 156] and optical beat signal conversion. References [157], [158] and [159] use adiabatic soliton compression of the beat signal generated between two independent CW lasers to generate pulse trains with repetition rates as high as 123GHz [158] and pulse widths of typically a few picoseconds. However, the linewidth of the sources mixed leads to excessively high jitter levels. This problem is removed through the technique of external phase [160] or amplitude modulation [161, 162, 50]. These modified techniques rely on the beating of modulation sidebands introduced into the optical spectrum of the single CW source used. Since both sidebands share common frequency noise the potential exists for much lower jitter levels.

Table 4.4.3 provides a comparison of the jitter levels of individual pulse streams for a series of generation methodologies. The third column provides a calculation of the theoretical maximum switching rates for the interaction of two pulse trains from each source. Comparison of the maximum switching rates with

Source	*RMS Jitter*	*Max. Switching Speed*
This configuration [163]	480fs(390fs)	133GBit/s
Actively mode-locked ring laser [69]	2.8ps	20GBit/s
Passively mode-locked ring laser [164]	600fs	98GBit/s
Beat signal conversion [50]	<500fs	>120GBit/s
Gain Switched DFB [156]	500fs	120GBit/s

the value calculated for this new configuration shows that the jitter performance of this source is comparable with the highest quality sources reported.

4.5 Conclusion

In conclusion, this chapter has presented results from a novel, all-fibre, dual-wavelength laser which combines the advantages of a dual-amplifier configuration with the use of chirped grating end mirrors. The use of all-fibre components makes

this source more compact and reliable than other fibre laser implementations reported to date.

A dual-cavity configuration eliminates the need for gain equalisation, a requirement in single-amplifier lasers where mode-competition must be overcome. Coupled with the use of chirped grating end-mirrors, this enables accurate and arbitrary definition of source wavelength enabling exploitation of the whole erbium gain band. In addition, independent wavelength tunability has been demonstrated through cavity length control. It has been found that the phase ripples on the chirped gratings used in the implementation cause this tuning to be step-wise rather that continuous with negative implications for the overall environmental stability of the system. However, it is clear that this difficulty is easily overcome by using apodised gratings which exhibit smoother dispersion profiles. Hence, it is expected that continuous tunability will be achieved when the current reflectors are replaced by gratings with smoother reflection band edges.

It has been shown that the overall intracavity dispersions are dominated by the dispersions of the end-mirrors and thus, it can be concluded that, by control of the individual grating design parameters, these components provide a compact and accurate means of dispersion tailoring without the need for insertion of lengths of fibre. Consequently, gratings enable control of both pulse width and temporal profile.

The generation of synchronised trains of solitons has been demonstrated, and it has been shown that grating phase ripple does not adversely affect mode-locked pulse quality. This is most likely due to self-adjustment of the individual cavity pulse widths so that the pulse spectrum straddles any localised dispersion perturbations with the result that only the underlying local average dispersion of each grating is "seen". It has been shown that this source exhibits an ultralow inter-pulse-stream jitter level of 620fs giving a theoretical maximum switching rate for a dual-wavelength NOLM in excess of 130 GBit/s. In addition, it may be concluded that this jitter level is ultimately limited by the jitter level of the mode-locking signal, and that further reduction may be achieved by optimisation of this parameter.

Chapter 5

Application of the NOLM to All-Optical Memory and All-Optical Phase Detection

5.1 Introduction

Thus far, the fibre NOLM has been used as a tool in investigations with the intention of broadly assessing the suitability of the device for nonlinear and soliton processing. It has been shown that this implementation has inherent advantages as a soliton switch, preserving the essential character of the data streams presented to it for manipulation. As an all-fibre switch, the NOLM is also well-adapted to integration into fibre laser configurations as demonstrated in chapter 4. In this final experimental discussion, preliminary results are presented from the use of the dual-wavelength fibre NOLM in two novel configurations. The first is a sequential design for all-optical memory in which two NOLM's are configured with feedback. The second uses the NOLM as an all-optical phase detector for inclusion in a phase-locked-loop (PLL).

The demands of these configurations serve to draw out some crucial limitations of the NOLM in its all-fibre manifestation. Although results from the memory and phase-locked-loop demonstrate that these configurations are, indeed, workable, both are seen to suffer due to instabilities introduced by the primary weakness of the fibre NOLM: its need for long fibre loop lengths. Since the fibre nonlinear coefficient is low, long interaction lengths are required for the accumulation of sufficient nonlinear phase to enable switching at practical power levels. In the memory particularly, these excessive fibre lengths are seen to cause intolerable instabilities in output due to environmental disturbance.

It, thus, becomes clear that, for the NOLM to find its way into more complex and higher speed systems, a more compact version using a more concentrated source of nonlinearity must be found.

5.2 All-Optical Memory

Memory is a function which is fundamental to the operation of high data rate networks; storage being vital for situations in which transmitting nodes must queue for network access, or at receivers where removal of a low bit rate channel and re-insertion of outgoing information may be required. Additionally, where excess traffic arrives at a network node, buffering is essential if information is not to be lost. A number of all-optical memory and buffer topologies have been demonstrated using fibre delay lines [165, 110, 112], amplifying recirculating loops [166, 167, 168, 169] and sequential nonlinear switch configurations [71, 170]. Although both delay line and recirculating loop memories provide the most simple forms of storage, their primary drawback is that they do not enable bit level logic processing. In other words, they perform the function of memory but do not enable higher level data manipulation. The configuration of Avramopoulos and Whitaker [71, 170], in which the output of a dual-polarisation NOLM [98] is fed back on a second pass to the control pulse input of the same device, was shown to be capable of arbitrary bit level inversion of the stored data but in its steady-state, the memory contents were inverted on successive round-trips, a result which is an inevitable outcome of the single-switch configuration used.

This section introduces a new all-optical memory architecture based on two NOLM's configured with feedback. If a word of any length up to a maximum determined by the latency of the two switches and the length of the feedback path, is loaded into the memory it remains stored if followed by a string of "0's". Unlike the implementation of Avramopoulos and Whitaker the stored word is not inverted on successive round trips. If a series of "1's" follows the input word, inversion of the entire memory contents may be performed, otherwise a word level exclusive OR (XOR) between the stored and successive words is achieved. Thus, this configuration may be used to perform basic, controllable logic operations as well as the function of storage.

Figure 5.1 shows an outline schematic and block diagram for this new all-optical memory architecture together with a truth-table summarising its operation. The memory consists of two dual-wavelength NOLM's configured with feedback, with two continuous, synchronised "power supply" pulse trains at wavelengths λ_1 and λ_2 at the input of each NOLM, and a data input at the control port of NOLM A at λ_1. The truth-table may be derived by systematically

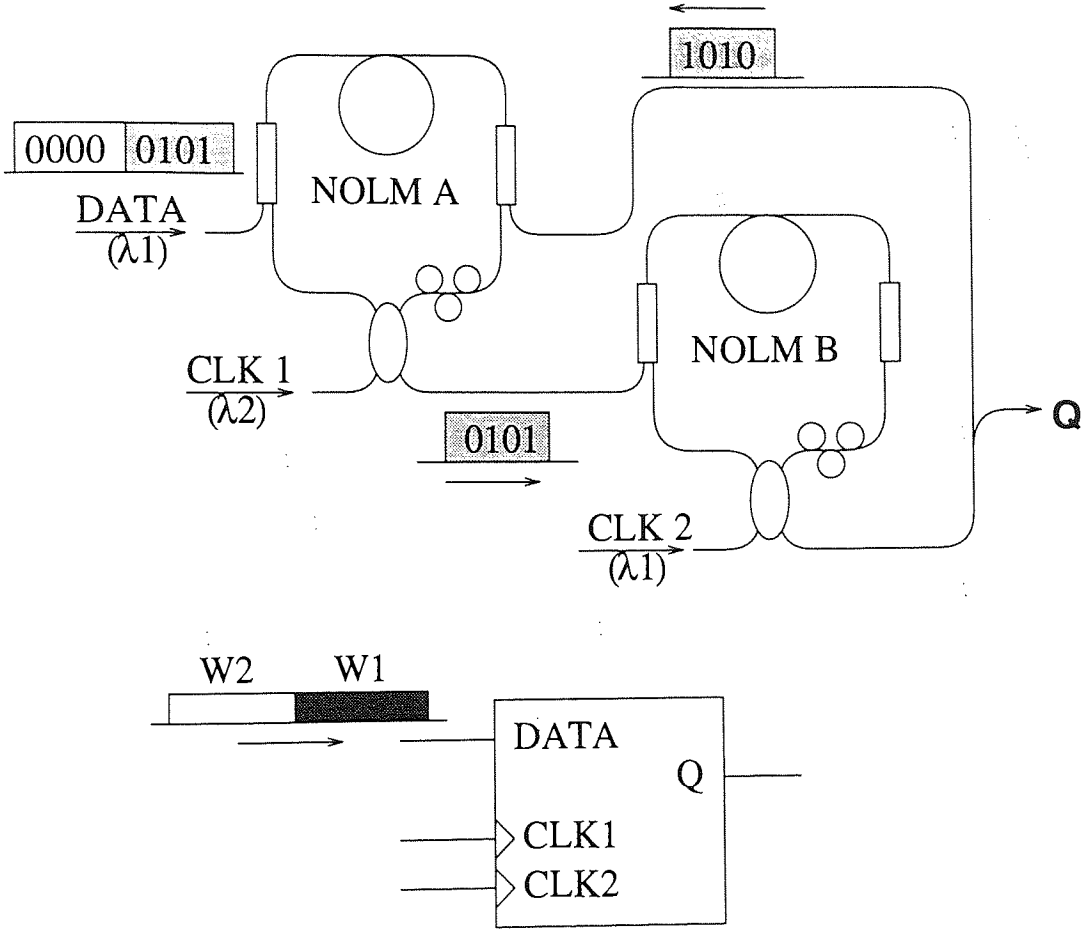

Functional Summary

W2	Q
All 0's	W1
All 1's	$\overline{W1}$
ELSE	W1 $\oplus$ W2

Figure 5.1: Outline schematic, block diagram and truth-table function summary for all-optical memory architecture.

analysing the output of the configuration for a set of all possible input conditions as follows.

Taking the simplest case of a single pulse (data "1") input at the data port and both NOLM's biased into linear reflection: arrival of a single data bit at wavelength λ_1 into NOLM A causes nonlinear transmission of a clock pulse at λ_2 from *CLK1*. This switched pulse then propagates into the control port of NOLM B causing a clock pulse at λ_1 from *CLK2* to be nonlinearly transmitted. On returning to NOLM A via the feedback path this pulse again causes switching of a single clock pulse at λ_2 from *CLK1* completing the cycle and effecting storage of the single bit. If the returning pulse coincides with the incidence of another incoming data "1", the symmetric XPM in NOLM A due to the presence of a control pulse in both arms of the device will result in no net nonlinear transmission giving inversion of the contents. The same result also occurs in the case of coincident returning "0's", which do not alter the linear reflection condition of the NOLM. Thus, the memory may be more generally stated as performing the exclusive OR (XOR) of stored and incoming data.

Extending this analysis to the incidence of words or packets of information, it is clear that the size of the memory is set by the length of the feedback path and the two XPM fibre sections in each NOLM. In the analysis above, the data word consists of a single data bit followed by a string of "0's". For a more general input word consisting of a random sequence of bits, the simple analysis above for the single bit leads to the outcomes summarised in the truth-table of fig. 5.1 for two arbitrary input words, W1 and W2. A single word is stored if the subsequent word contains all "0's" as illustrated for the four bit word "0101" in the schematic of fig 5.1. If the following word is all "1's" the bit XOR function of NOLM A will cause inversion of the stored word, otherwise the memory performs a word level XOR.

Figure 5.2 shows a schematic of the configuration used to verify these predictions experimentally. The NOLM's were constructed using 50/50 ($\alpha = 0.5$) fused-fibre couplers and 5km lengths of dispersion shifted fibre (DSF1) with a zero dispersion wavelength, λ_0, of 1551nm. Data and clock signals at 1557nm (λ_1) and 1540nm (λ_2) were supplied by the dual-wavelength laser detailed in chapter 4 [171]. Signals at each wavelength were combined and separated in the NOLM's using bidirectional JDS Fitel WDM's with 6nm wavelength windows

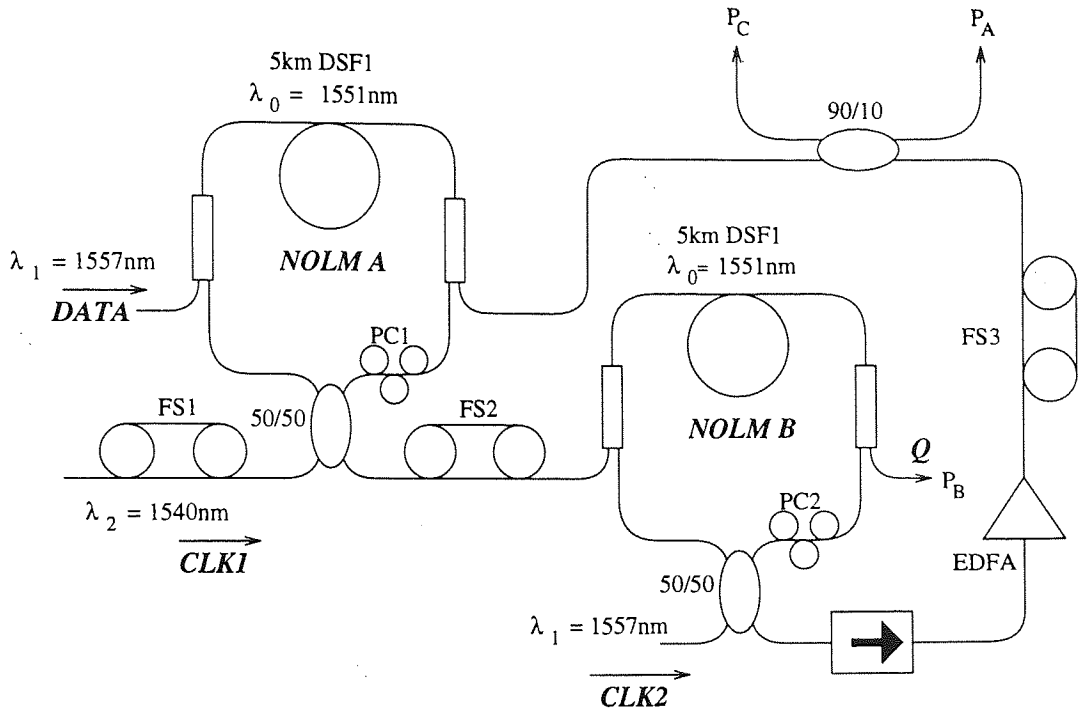

Figure 5.2: Schematic of all-optical memory experimental configuration. FS, fibre stretcher.

at 1535nm to 1541nm and 1555nm to 1561nm. The wavelengths chosen to perform switching were selected to nearly symmetrically straddle the zero-dispersion wavelength , thereby minimising the dispersive walk-off between the signal and control pulses and hence, also the required switching power [100]. To isolate the NOLM's from environmental disturbances, they were placed in sealed polystyrene chambers. Fibre stretchers were included in the configuration to ensure optimum temporal overlap between the interacting pulse trains. The insertion loss of each NOLM was ~3dB, and the measured switching thresholds were at input power levels giving P_A=30μW , P_B=300μW and P_C=70μW corresponding to total input power levels of 630μW . Measured extinction ratios at these powers for NOLM's A and B were 86% and 100% respectively.

Since the pulses at 1557nm lay in the anomalous dispersion regime for the fibre used, difficulties arose in switching NOLM A using switched clock pulses from *CLK2*. It was found that if sufficient power was launched into NOLM B at 1557nm to switch NOLM A directly, the accumulated 11km propagation distance resulted in the break-up of these pulses, due to self-Raman generation, within

NOLM A and hence in the total break-down of switching. A 980 nm pumped EDFA was, therefore, placed in the feedback path so that the input power could be reduced to a level low enough to minimise self-Raman generation and SPM in NOLM B before entering NOLM A. An isolator was placed in front of the amplifier to prevent amplification of the EDFA stimulated emission reflected by NOLM B.

Timing of the sequence was performed as follows. NOLM A was biased into linear transmission and P_B was reduced to a power level well below the switching threshold of NOLM B. With the NOLM rebiased into reflection and P_A set to the switching threshold for NOLM A of 30μW , the relative temporal overlap of the *DATA* pulses and pulses from *CLK1* was optimised using FS1 by maximising P_A. With P_A now increased to the threshold switching power for NOLM B of 300μW and the feedback path blocked using a tight fibre bend, FS2 was varied to maximise P_C, the point at which *CLK2* and the nonlinearly switched pulses from *CLK1* are optimally overlapped. The signal emerging from this same port was then viewed using an optical spectrum analyser and the input power level of *CLK2* was reduced until SPM induced spectral broadening was minimised and Raman generation did not occur. The amplifier pump power was then adjusted to take the power level P_C to 70μW , the switching threshold for NOLM A. Finally, P_A was again reduced to well below the threshold switching level and both NOLM's A and B were biased into linear transmission. With the feedback path open, pulses from NOLM B coincident with pulses at the *DATA* input cause extinction of the nonlinearly transmitted signal, Q, as described above, thus feedback path timing is matched when P_A is minimised. When timed, operation of the memory occurs when P_A is increased to the threshold switching level and both NOLM's are, again, linearly biased for reflection.

Figure 5.3 shows a trace taken from the memory output port, Q, for a continuous train of pulses at the data input. A random data pattern was introduced into the configuration by mechanically disturbing one of the NOLM's and the output was recorded using a medium area photodetector with a bandwidth of 200kHz. Although the detector is not fast enough to follow individual pulses, it is clear from the trace that the memory is storing a data pattern which is being inverted on every round trip, the behaviour predicted by the truth-table in fig. 5.1. The period of this cycle is 107μs corresponding to a transmission distance of 11.3km

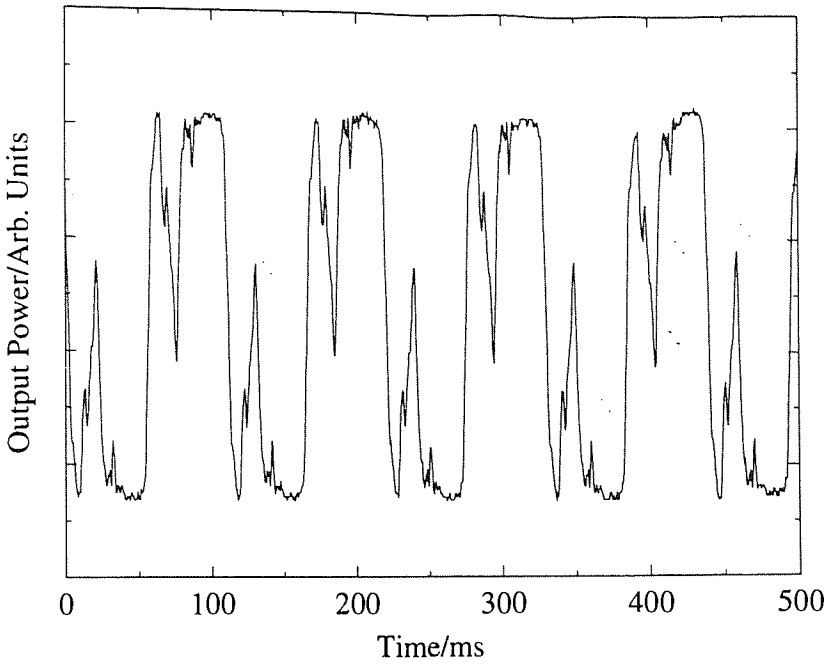

Figure 5.3: Output of memory at port Q with a continuous pulse train at the data input.

and a word length, at 76MHz, of 0.5kBytes.

Thus it is clear that this configuration is capable of storage as predicted. However, even after significant experimental effort, the output was found to be intolerably unstable. As already discussed in the introduction, the root of this instability lies in the excessive fibre lengths required to enable switching at practical power levels. The next section traces a number of inherent instabilities which are a direct result of this requirement. It concludes with recommendations which are likely to increase reliability; the first being based on a fundamental change in implementation in which the NOLM is replaced by alternative, more compact, semiconductor-based devices; and the second on a reconfiguration of the fibre-based memory already discussed.

5.2.1 Sources of Instability

Three major sources of instability arise from the long fibre loop lengths used. Firstly, vibrational and acoustic disturbances, the effects of which could not be reliably quantified, were observed to cause the superposition of noise on the non-linearly switched signal from each device. These fluctuations were found to vary

randomly in magnitude, but were mostly around a few percent, with occasional momentary drop-outs of nearly 100%. Clearly, such extreme variations will have a detrimental effect on the stored pattern, causing it to be unpredictably corrupted over time.

Secondly, there is the influence of drifts in loop birefringence as well as polarisation drift in the circulating and interacting signals, both of which may be attributed to environmental changes in fibre orientation, thermal expansion and contraction in the fibre stretchers and fibre reels as well as to circulating air currents. It was observed that, even over a period of only 30 to 60 seconds after the NOLM's had been linearly biased for maximum reflection, environmental fluctuations caused appreciable changes in the loop reflectivity due to drift of the fibre loop birefringence. This drift in linear bias was also seen to affect the nonlinear switching characteristic, altering the extinction ratios, and nonlinear switching thresholds of each NOLM as well as the percentage nonlinear transmissions at the initial clock and data input power levels. In addition, it was observed that, as the bias drifted, the output developed a decreased immunity to acoustic disturbances resulting in an increase in noise in the switched signals [105].

Similarly, the nonlinear switching characteristic of the NOLM is altered as the relative polarisations of the clock and control signals drift from the point at which XPM between each is a maximum. Figure 5.4 (i)(a) shows the measured nonlinear switching profile for NOLM B when the polarisations of the control and signal pulse trains are set for optimal nonlinear switching, and fig. 5.4 (i)(b) the same results when they are oriented orthogonally. It is clear that, as the relative polarisations drift away from the optimum, the switching threshold of the device increases and the transmitted intensity drops. Thus, these two manifestations of environmental polarisation drift are seen to cause a gradual degradation in the nonlinear switching characteristic with decreasing transmitted signal power leading, ultimately, to pulse drop-out and data corruption.

Finally, and with similar results to the mechanisms described above, there is the effect of thermal length changes in the fibre stretchers. Figure 5.4(ii)(a) shows the nonlinear switching characteristic for NOLM B when the temporal positions of the signal and control pulses are optimised, and fig. 5.4(ii)(b) the output when the pulses have been temporally offset by 26ps. It is clear that the switching response is significantly degraded. Figure 5.5 shows a more systematic

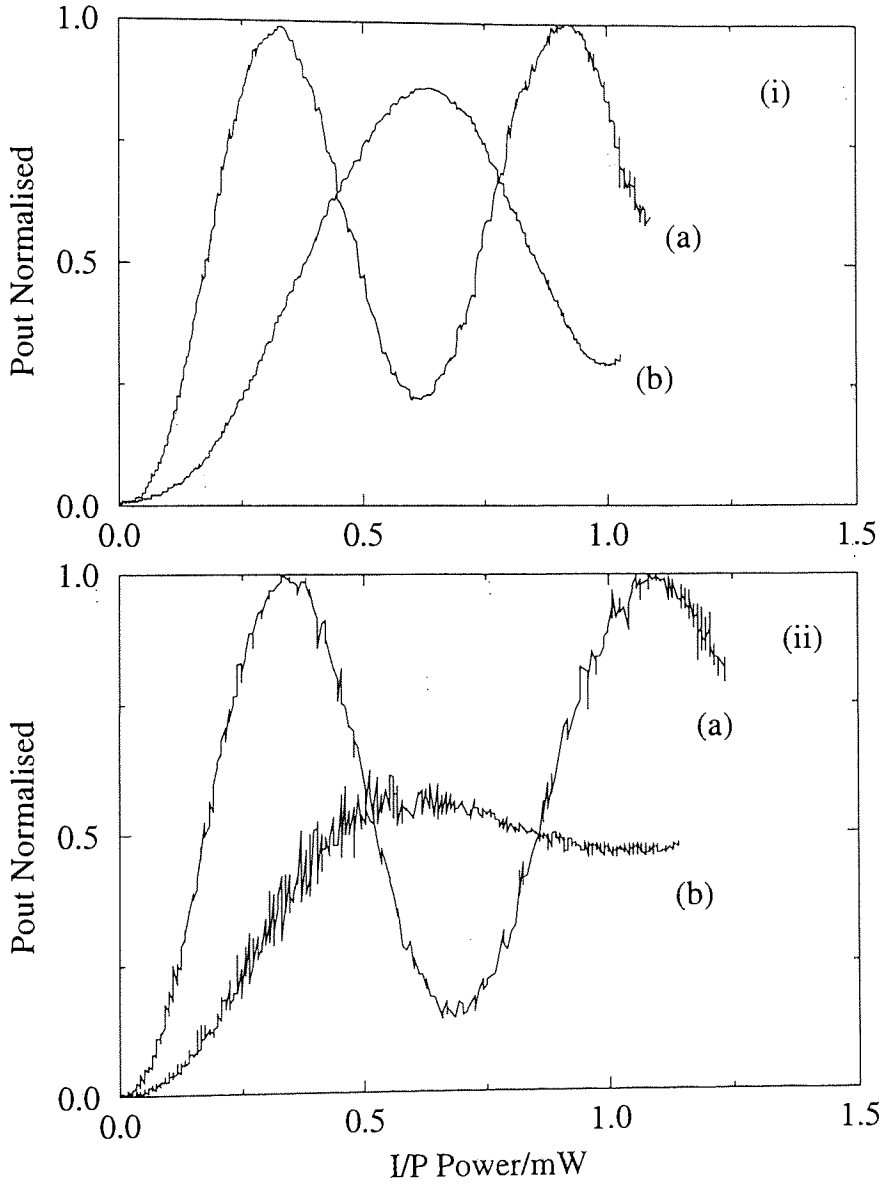

Figure 5.4: NOLM B nonlinear transmission profiles with (i)(a) signal and control polarisations oriented for maximum switching efficiency, (i)(b) signal and control polarisations in the orthogonal state; (ii)(a) optimal temporal overlap, (ii)(b) relative time delay of 26ps.

analysis of the effect of timing drift on the nonlinear switched signal, plotting the change in transmitted intensity with relative temporal offset. It is clear from

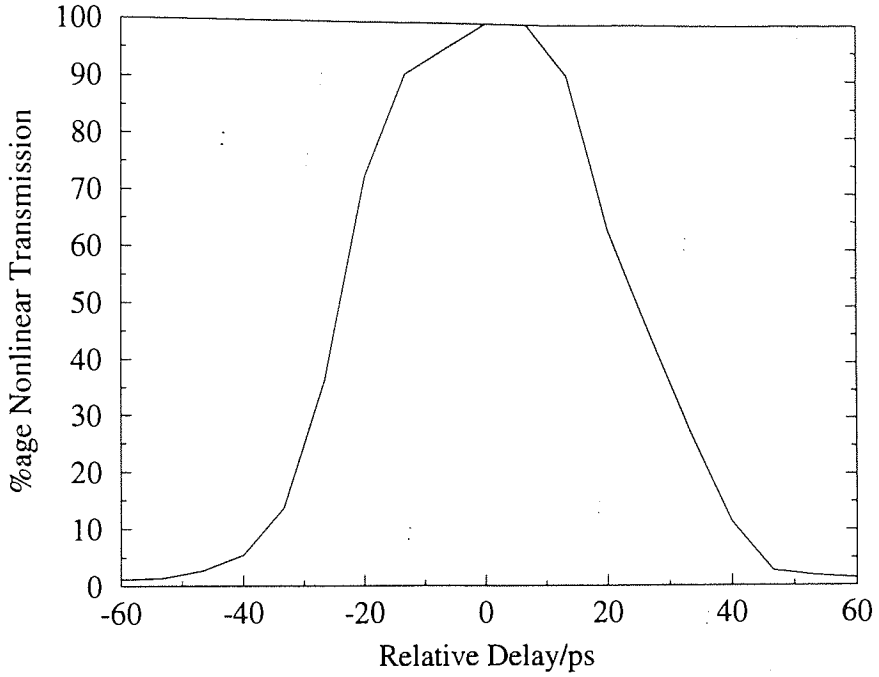

Figure 5.5: Plot of percentage nonlinear transmission against relative temporal offset between signal and control pulses for NOLM B.

the measured switching window width of 40ps that source jitter is not the major temporal limitation, since the minimum switching window width required by the dual-wavelength laser configuration used is 7.5ps (see section 4.4.2 of chapter 4). However, it is also apparent that the output of the device drops off steeply for relative temporal drifts beyond $\pm$12ps, corresponding to an overall length change of only $\pm$3.6mm. The fibre stretchers used in the experiment each carried 34 turns of fibre between two drums, the relative positions of which were varied using motor driven actuators. If it is assumed that they are all equally affected by thermal drift, this corresponds to a change in relative position of the drums in each stretcher of only 11μm . Thus thermal expansion and contraction is also a primary concern.

In addition to these environmental instabilities, another source of failure in nonlinear switching, which has already been referred to, is the influence of Raman break-up of control pulses in the anomalous dispersion regime. Pulses at the switching threshold power for NOLM A of 630μW correspond, initially, to a

higher order, N=9, soliton. Figure 5.6 summarises measured autocorrelations and spectra recorded at the end of the 5km fibre span used in NOLM A at a series of input power levels. Figures 5.6(i) shows the autocorrelation at an input power of 400μW and, therefore, just below threshold; (ii) at 700μW , just beyond threshold; and (iii) at 1.2mW. It is clear from the gradual appearance of a short central spike and from the growth of a marked peak to long wavelength in the spectral progression in figs.(iv), (v) and (vi), that Raman break-up is an important consideration in this configuration. Crucially, the autocorrelation and spectrum at an input power level of 700μW show that Raman generation and pulse break-up are clearly present even at the switching peak, providing the most likely explanation of the relatively low peak transmission of 86% in this NOLM as compared with 100% in NOLM B. Thus, it would appear that a way must be found of decreasing the impact of this problem on the overall functioning of the memory.

It is clear from the foregoing discussion, that the major sources of memory failure are due, ultimately, to the long loop lengths used in the NOLM's. The following section makes recommendations which are likely to reduce the impact of these phenomena.

5.2.2 Recommendations for Revised Memory Architecture

Two alternatives may be used to alleviate these difficulties. Firstly, since both sets of problems are a result of the long loop lengths used in the NOLM's, their replacement with semiconductor laser amplifier-based nonlinear loop mirrors [172, 173, 174, 175] are likely to reduce the impact of environmental disturbances. Since nonlinearity due to gain modulation in SLA's is sufficient to induce nonlinear switching alone, this enables minimisation of the fibre waveguide component, thereby maximising environmental robustness. This reduction also has the incidental benefit of removing Raman-induced pulse break-up.

Alternatively, taking the configuration as it stands, and accepting the effects of environmental change, the impact of higher order pulse break-up may be reduced by reconfiguring the NOLM's so that switching in the anomalous regime occurs only once. The revised configuration, shown in fig. 5.7, has both the *DATA* and *CLK2* inputs at 1540nm with NOLM B as the data input device,

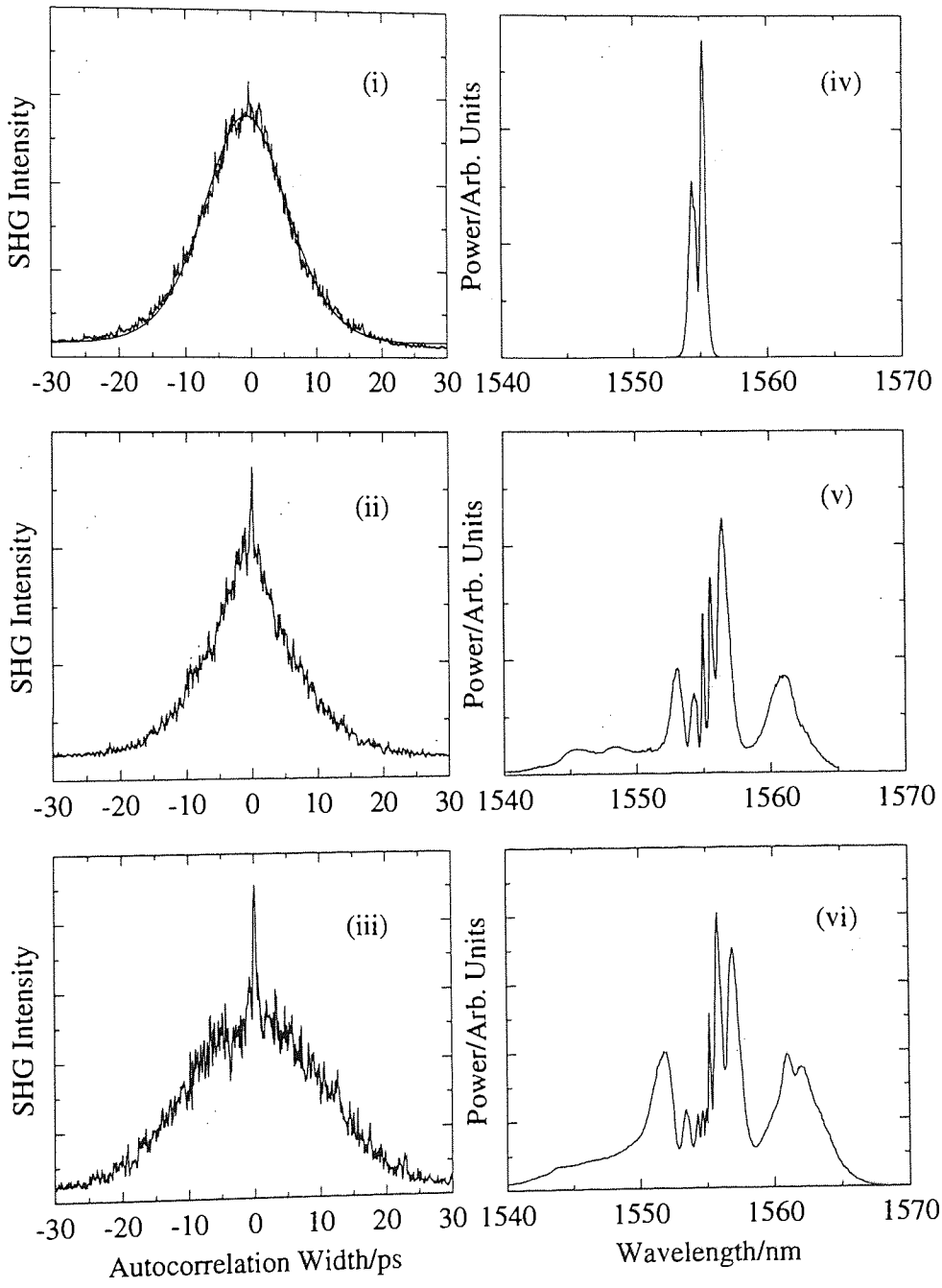

Figure 5.6: Autocorrelation at output of 5km span of DSF1 at (i) 400μW , (ii) 700μW , and (iii) 1.2mW input power levels. (iv), (v) and (vi): respective spectra.

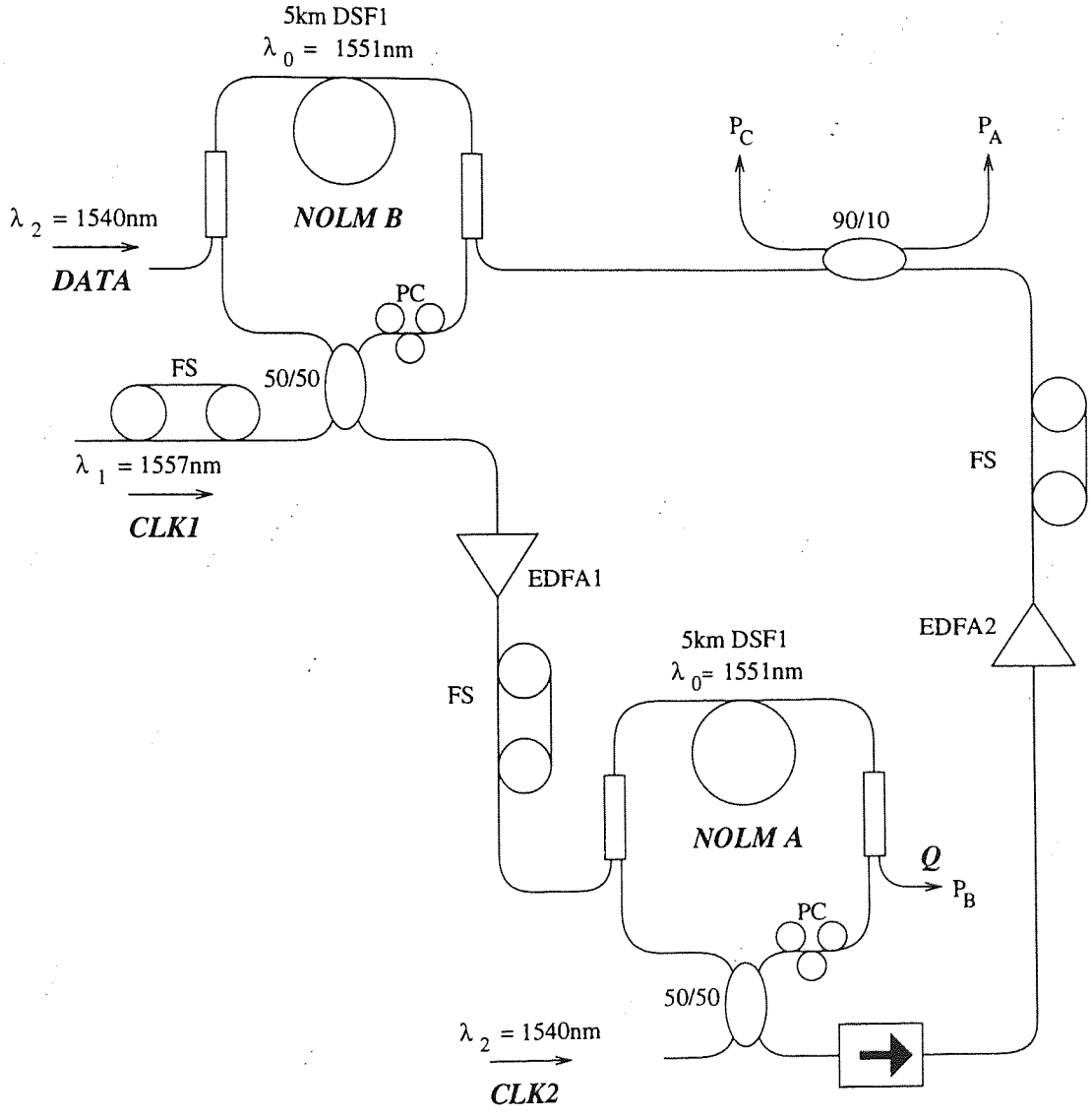

Figure 5.7: Schematic of revised memory configuration for minimisation of the effects of higher order soliton break-up in the anomalous regime and of SPM enhanced temporal broadening in the normal regime.

thus, ensuring that switching in the anomalous regime occurs only once in each memory cycle and minimising the negative impact of higher order pulse break-up on the peak transmission level. Note that the feedback path amplifier has been retained. This enables the injection of only a lower power clock signal at *CLK2* and has the effect of minimising SPM enhanced temporal broadening of these pulses within NOLM A ensuring that pulses from CLK2 do not broaden beyond the switching window of the device and maximising the peak transmission level. This reconfiguration was not performed, as experimental effort was redirected to minimisation of the impact of inter-pulse-stream timing jitter by development of the laser configuration of chapter 4.

5.3 NOLM as an All-Optical Phase Detector in a Phase-Locked-Loop

The current section addresses a further application of the dual-wavelength NOLM, namely that of phase detection, and its inclusion, in this capacity, within a phase-locked-loop configuration.

The use of the NOLM as a phase detector is an extension of its use as an all-optical sampling oscilloscope [176]. When a train of ultrashort pulses is used as the control signal for a dual-wavelength NOLM which has a slowly varying periodic signal at its input, the output of the NOLM will consist of a series of pulses with amplitudes proportional to the magnitude of the input signal at the temporal positions of the switching pulses (sampling instants) as illustrated in fig. 5.8(i). Thus, the control signal pulse train may be thought of as a comb function. For the case in which there is a frequency mismatch between the input and sampling signals, the output pulse train will be seen to vary continuously in amplitude at the difference frequency, f_s-f_{in}, where f_s is the frequency of the sampling pulses and f_{in} is the frequency of the signal at the input of the NOLM. If this pulsed output is detected and fed into a low pass filter the product will then be a continuously varying voltage level proportional to the relative phase of the sampling and input signals. It is this function which enables the use of the NOLM as an all-optical phase detector in a phase-locked-loop (PLL) configuration. Figure 5.8(ii) illustrates the output of the device when the frequencies are identical. In this case, the sampling instant coincides with the same point on the

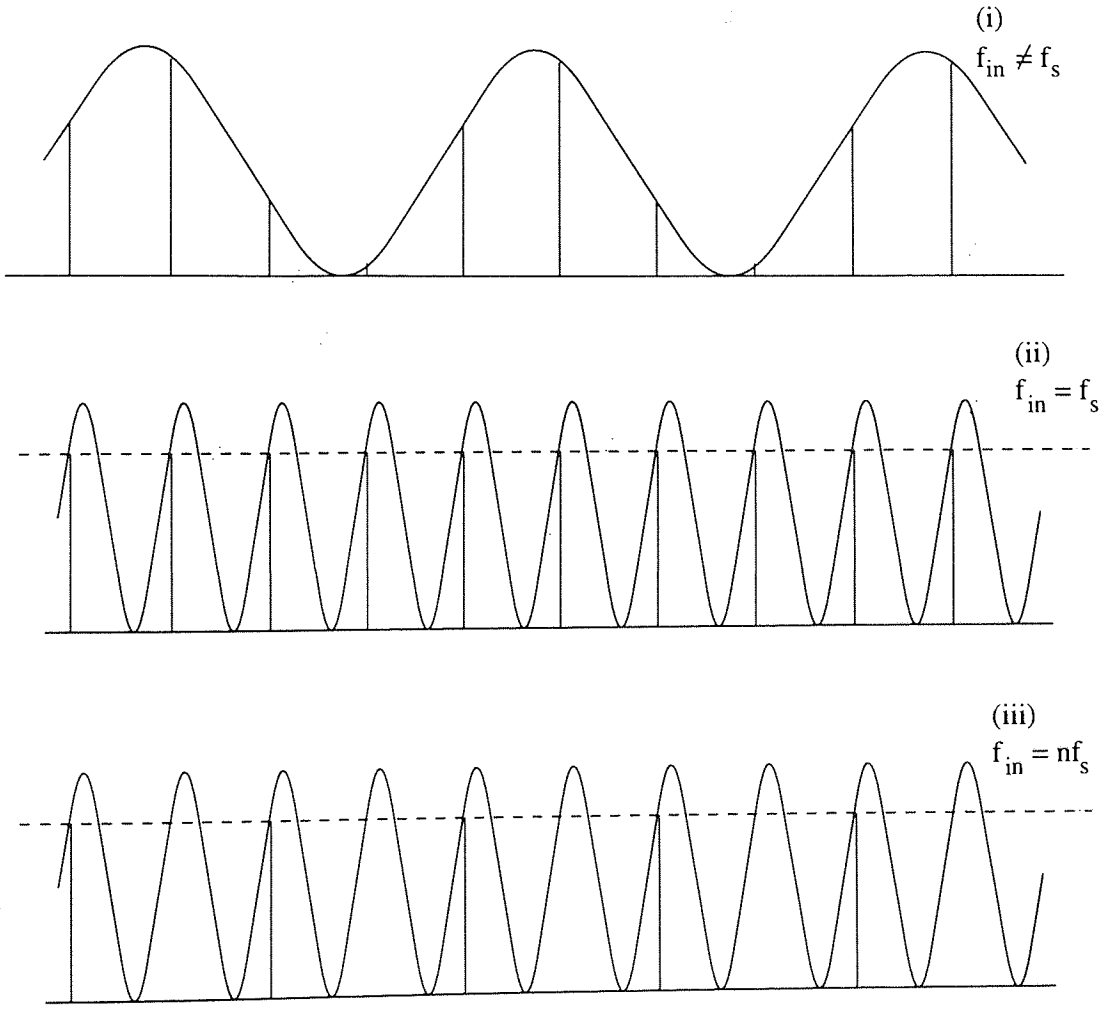

Figure 5.8: NOLM sampling. (i) signal frequency (f_{in}) $\neq$ sampling frequency (f_s), (ii) f_{in}=f_s (iii) f_{in}=nf_s where n=2.

input signal waveform. It is clear from fig. 5.8(iii) that the same is also true for input signals at frequencies which are integer multiples of the sampling rate. In both cases, the phase relationship between the input and sampling signals is constant. It is this point towards which as PLL will converge, and it is apparent that the use of the NOLM as a phase detector will enable locking at both harmonics and sub-multiples of the sampling frequency.

Phase locking is a standard technique for clock recovery and subsequent demultiplexing of high bit rate data streams [177]. All-optical phase detection using gain modulation in semiconductor laser diode amplifiers, devices which have an advantage of low latency, has been used to perform PLL timing extraction at data rates as high as 200Gbit/s [104]. However, the configuration used is capable only of timing extraction at the total received data rate. The recovery of a base data rate clock signal from a time-division multiplexed (TDM) data stream requires extraction of a low frequency component from higher frequency data, a function which may be performed, at the cost of increased system complexity, by inclusion of additional frequency multipliers in the PLL feedback path [178]. By using a NOLM as a phase detector, however, timing information at both multiples and sub-multiples of the sampling rate (baseband) frequency may be achieved without additional components.

Figure 5.9 shows a schematic of the experimental PLL configuration used to demonstrate this principle. The NOLM was constructed using a 100m section of DSF1 (λ_0=1551nm) and a 50/50 (α=0.5) coupling ratio. In preliminary experiments it was found that loop lengths any greater than 500m resulted in poor phase-locking due to switch latency. By reducing the length to 100m this instability was overcome but at the expense of reduced switched power. A trade-off is likely to exist, therefore, between the need to minimise latency and the need to maximise the magnitude of the error signal; maximisation of the error signal being desirable for phase-locking since it enables reduction of feedback-amplifier gain with a consequent increase in overall PLL bandwidth. It is clear that, as in the memory configuration, the NOLM-based PLL detector will also benefit significantly from the use of an SLA-based device. Sampling pulses of 7ps duration at 1557nm and a repetition rate of 76MHz were provided by a dispersion modified actively mode-locked erbium fibre laser [133] and the sampled output was detected using a medium-area detector with a bandwidth of 200kHz. Sig-

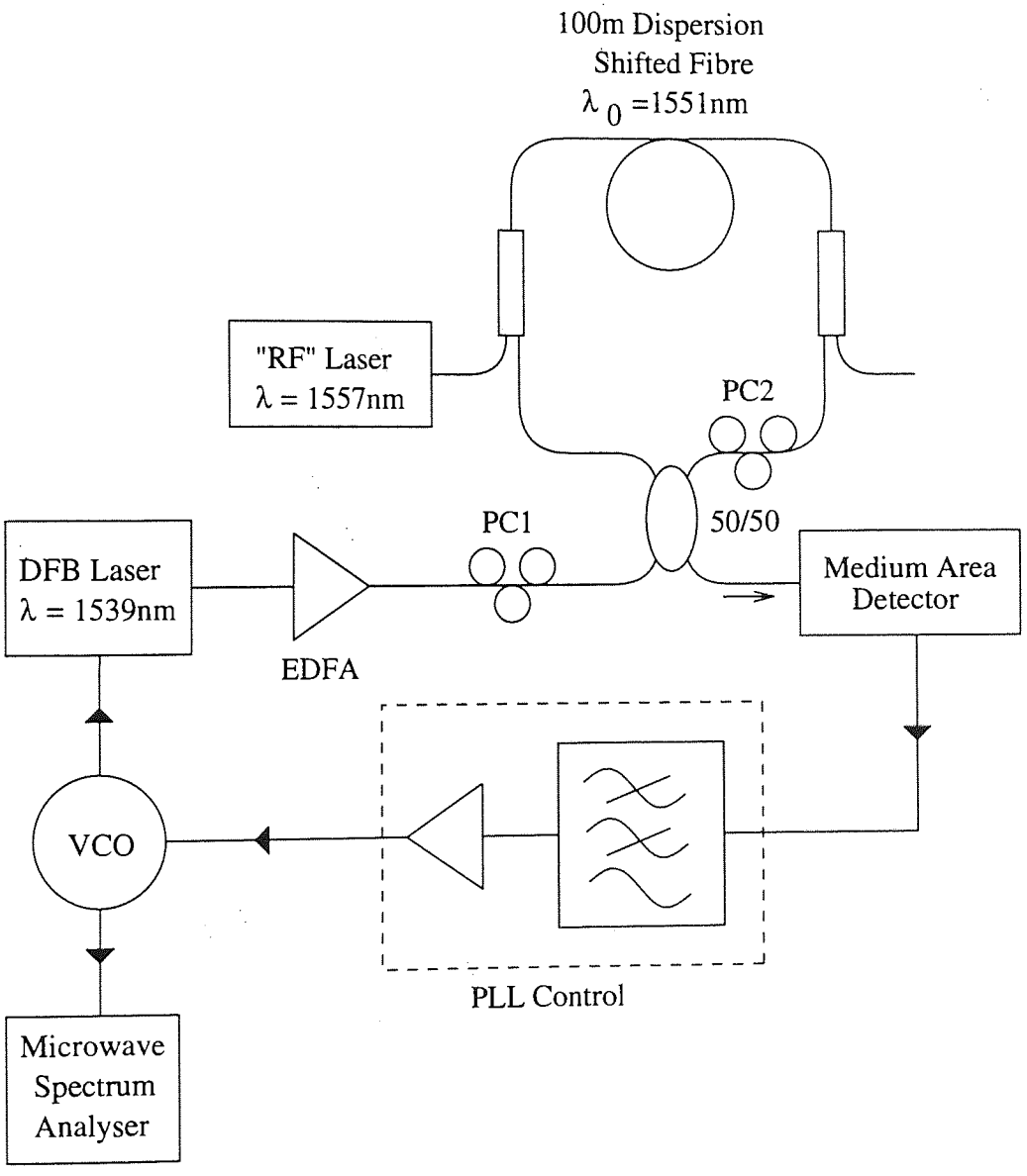

Figure 5.9: Schematic of experimental phase-locked-loop configuration using a NOLM as an all-optical phase detector.

nal light at 1539nm was provided by an amplified DFB laser, modulated using a HP83650A synthesised sweeper.

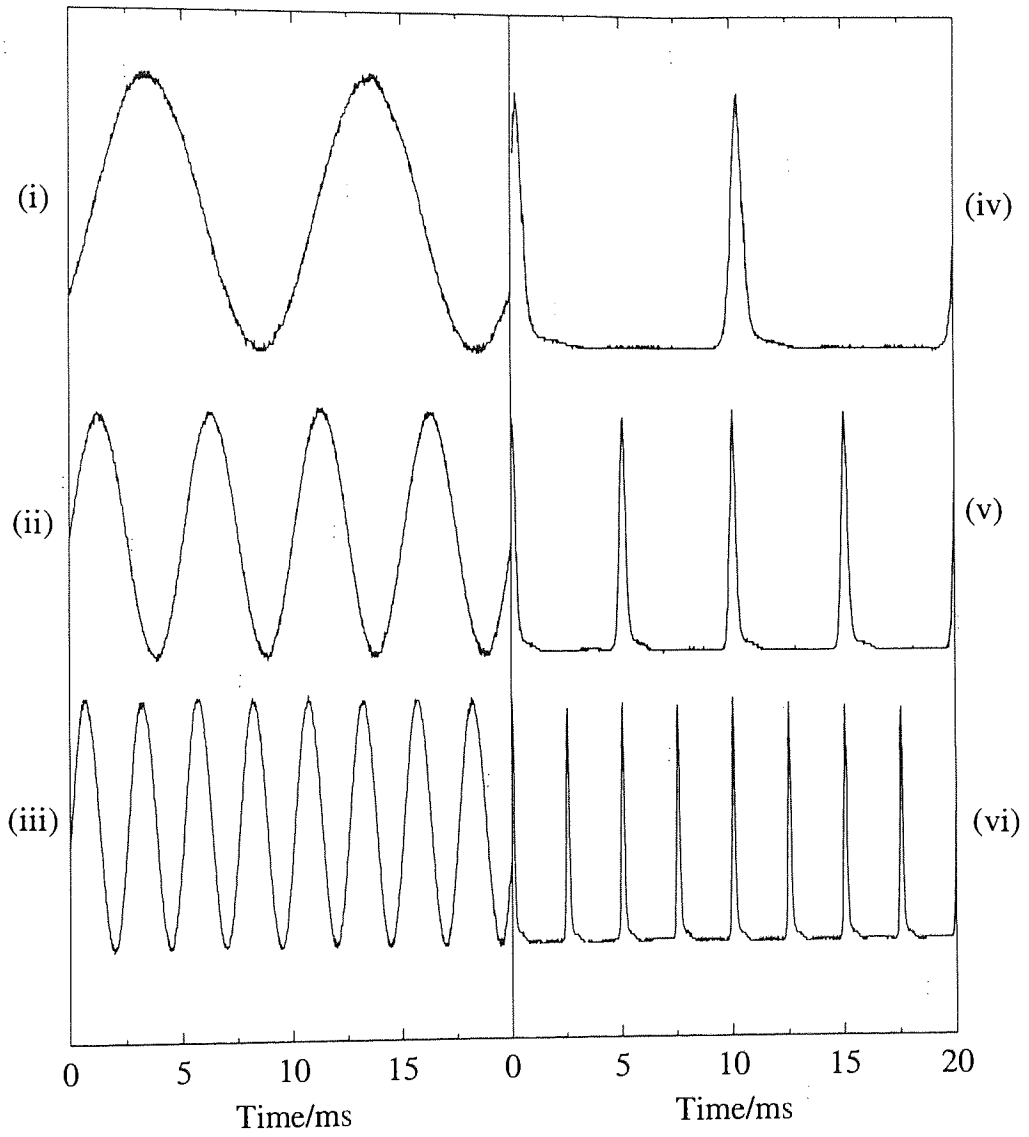

Figure 5.10: NOLM output with sinusoidal input signal: signal frequency = f_s+ (i) 100Hz, (ii) 200Hz, (iii) 400Hz. Output with gain-switched DFB input signal: signal frequency = $10f_s$+ (iv) 100Hz, (v) 200Hz, (vi) 400Hz.

Figure 5.10 shows the output of the NOLM with the DFB sinusoidally modulated at frequencies of (i) f_s+100Hz, (ii) f_s+200Hz, and (iii) f_s+400Hz. The average power of the sampling pulse train was ~2-3mW. These traces clearly show the beat signal due to frequency mismatch between the two signals illustrated in fig. 5.8 (i). Figures 5.10 (iv), (v) and (vi) show the output with the

DFB gain-switched at frequencies of $10f_s$+100Hz, $10f_s$+200Hz and $10f_s$+400Hz. It is clear from these that the behaviour of the NOLM as a phase detector is identical at multiples of the baseband frequency, as suggested in fig. 5.8 (iii). By feeding the output of the NOLM into the synthesised sweeper, configured as a voltage-controlled-oscillator (VCO), the loop may then closed, and phase locking may be achieved.

Figures 5.11 (i), (ii) and (iii) show microwave spectra over a 100kHz span with the DFB gain-switched and phase-locked to the sampling pulse train at frequencies of the 76MHz, 531MHz, and 1.062GHz corresponding to the fundamental, seventh and fourteenth harmonics respectively. Figures (iv) and (v) show traces at 531MHz and 1.062GHz over a 10kHz span. It is clear from examination of these results that the phase noise pedestal does not rise significantly, even when the DFB is phase-locked at the fourteenth harmonic. Thus the performance of the PLL within this range may be considered independent of the harmonic chosen.

A disadvantage of this implementation is its sensitivity to drift in loop birefringence. It was found that, as the bias of the NOLM drifted due to environmental influences, the gradual rise in output signal power caused phase locking to decay over time until locking could no longer be achieved. This may be alleviated by using polarisation maintaining fibre, but has also been removed by frequency dithering of the clock signal [179]. This configuration has been used to demonstrate phase locking at a harmonic of the baseband frequency. However, by simply reconfiguring the setup so that the sampling source is driven by the VCO, phase locking at a sub-multiple may also be achieved [22] an implementation which may enable simultaneous clock extraction and demultiplexing of a base rate data channel.

5.4 Discussion

Results from these novel configurations demonstrate that each is clearly operational but severely limited by instabilities introduced by the NOLM. Summarising results from each in turn, it is clear that the output of the memory is that predicted by the truth table in fig. 5.1 for a continuous set of 1's, and consequently, that with modification, the other functional characteristics may also be obtained. The major impact of fibre length on this configuration arises, ultimately, from

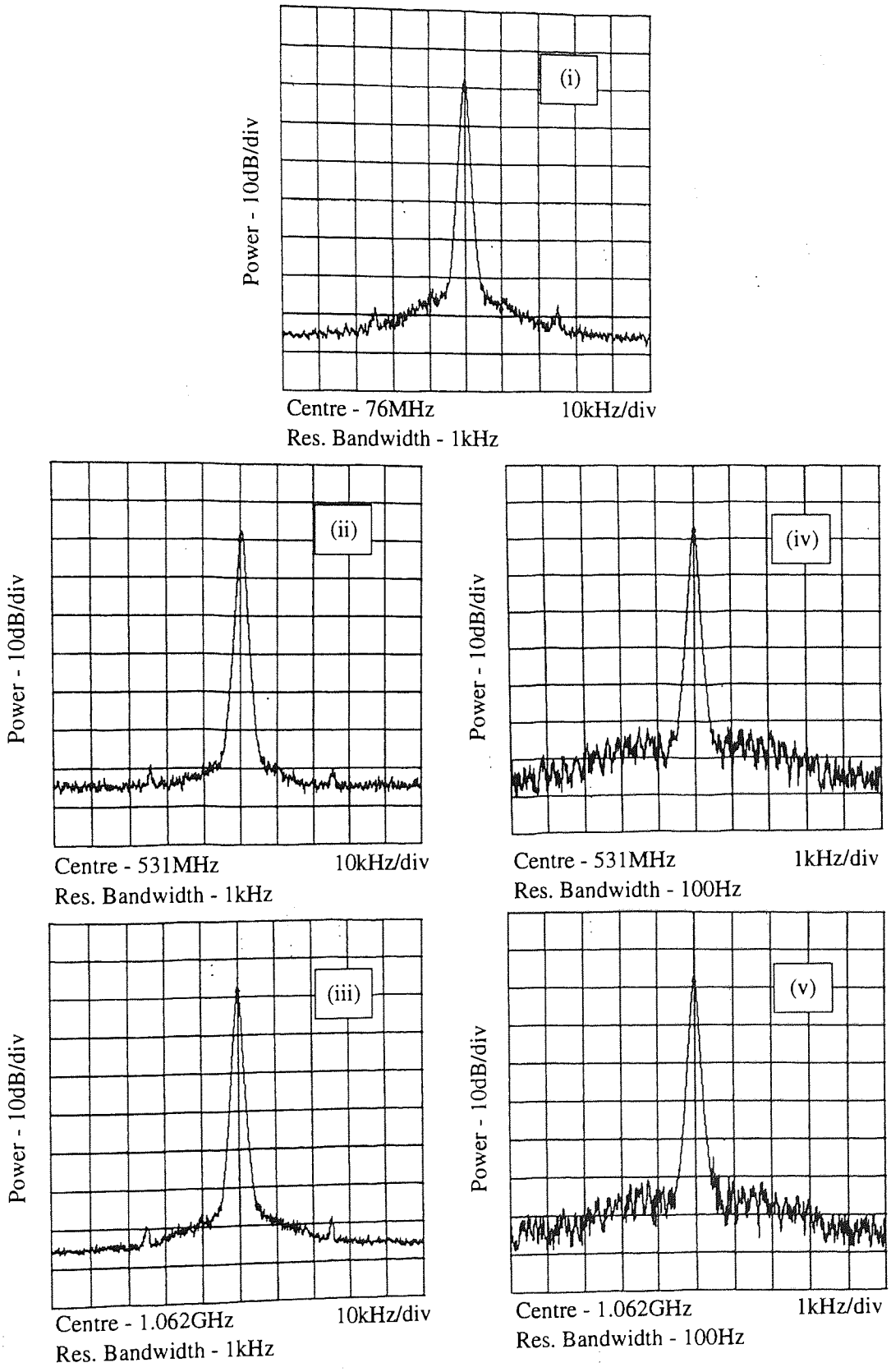

Figure 5.11: Microwave spectrum of VCO drive signal with DFB gain-switched and phase-locked at (i) 76MHz, (ii) 531MHz, (iii) 1.062GHz, over a 100kHz span; (iv) 531MHz and (v) 1.062GHz over a 10KHz span.

environmental changes in fibre birefringence and length as well as from Raman-induced pulse break-up.

The PLL configuration has been shown to be capable of phase-locking to as high as the fourteenth harmonic of the baseband frequency. Reconfiguration also enables locking to sub-harmonics, with consequent potential for simultaneous timing extraction and demultiplexing. Although the PLL was also environmentally sensitive to an extent, with birefringence effects causing the gradual drift in quality of the phase-locked microwave spectrum, the much smaller loop length significantly reduced the impact of this effect. The primary implication for the PLL was found to be the inherently high latency of the device, a factor which dictated that error signal power be sacrificed for stability, with a consequent reduction in the dynamic range of the loop due to the accompanying requirement for increased feedback-amplifier gain.

The modification with the greatest potential benefit for both of these configurations is the replacement of the fibre NOLM with a SLA-based device. The concentration of nonlinear phase due to gain modulation in the amplifier negates the need for waveguide nonlinearity, and, thus, minimises the overall length of the NOLM. The use of such a device will also reduce switch latency to a minimum, and extend the bandwidth of the loop. A reduction in overall loop length also has the effect of minimising the impact of environmental disturbance and removes problems of pulse break-up due to self-Raman generation in the soliton regime.

In conclusion, these results show that a limit exists to the usefulness of the all-fibre configuration. Although the simplicity of the device and the accessibility of fibre nonlinearity make this form of NOLM an excellent tool with which to evaluate novel configurations, it is clear that in "real-world" scenarios where high speed, low latency and robustness are of primary importance, alternative implementations such as those based on SLA's may provide a more successful alternative.

Chapter 6

Conclusions

6.1 General Conclusions

The central concept addressed in this thesis has been that of device concatenation, a concept which is clearly fundamental to the construction of any data processing architecture. As a device which has received a great deal of attention in the past few years, the nonlinear-optical loop mirror (NOLM) is a good choice as a basis for such an experimental investigation. In its fibre form, with its simplicity of construction and easily accessible nonlinearity, the NOLM is useful as a tool for study and has significant advantages as a primitive switching element over other devices, including low switching power, and relatively good environmental stability. In addition, being constructed from optical fibre, it is a device well-suited to further evaluation of the advantages of the soliton as a data carrier.

After introducing the concepts which govern operation of the NOLM, chapter 2 presents the first, foundation, experimental investigation aimed at characterising a single NOLM, a natural starting point for an extended analysis involving concatenation of multiple devices. This first analysis is centred on two fundamental characteristics of device performance: the amplitude response to a train of solitons, and the effect of transmission through the device on the temporal and spectral integrity of pulses passing through the device.

Using pulses of 7ps duration, an order-of-magnitude longer than input pulses used in previous experimental investigations, the time-averaged response of the NOLM has been extended to demonstrate, for the first time, a multiple-peaked switching characteristic. The primary source of device failure has been known for some time to be incomplete interference on return to the coupler due to Raman-induced soliton self-frequency shift (SSFS) and ultimate break-up of higher order pulses. By choosing longer pulses with narrower spectral content, overlap with the Raman gain spectrum is decreased, and the influence of both effects is reduced. Systematic numerical analysis of the impact of this phenomenon, plotting the

change in switching characteristic with input pulse width shows that quality of response is not significantly improved by further increases in pulse width. Indeed, from the τ^2 dependence of z_0 , and hence, also of loop length, it is probable that any benefit which might be gained from a more extensive switching characteristic will be more than offset by unacceptable environmental sensitivity. The influence of higher order pulse shaping may well limit the usefulness of the device beyond the first peak anyway.

As has been stated on a number of occasions throughout this thesis, it is not enough to consider the amplitude response of the device divorced from its impact on the essential temporal and spectral characteristics of the pulses processed. Thus, comparison has been made between input pulse characteristics and those of emerging pulses. This has shown that transmission through the device causes only minimal degradation of the soliton nature of an input pulse train, with increases in pulse width and time-bandwidth product being dominated by asymptotic self-adjustment of solitons within the arms of the device due to the launching of slightly chirped pulses. Thus, the primary conclusion of this preliminary experiment is that, since the NOLM causes only slight degradation in the soliton nature of processed pulses, emerging data remains capable of further processing.

In chapter 3 this hypothesis is tested by an investigation of soliton switching in a two-device cascade. The first configuration used, based on a single NOLM with feedback serves to highlight the factor which dominates the design of such a cascade, namely loss. The mismatch between the power level of the return signal on the second pass and the switching threshold at the first peak is shown to significantly degrade performance of the overall configuration. By constructing a simple model based on evolution of the soliton phase, the fibre length and coupling ratio required by the second device for optimal matching are predicted. Investigation of this optimised cascade has shown that the enhancement of amplitude response which is known to occur in CW switching *i.e.* sharpening of the switching edges and flattening of switching peaks, also occurs in the soliton regime, but with one crucial difference: this enhancement is not accompanied by a significant degradation in the soliton nature of emerging pulses. As in the single-device analysis, output pulses are temporally broadened due to self-adjustment of initially chirped pulses. An additional contribution from loss-induced adiabatic broadening is also

probable. Thus the benefits of device cascading for the amplitude response of increased immunity to input noise at the switching peaks and enhanced discrimination at the switching edges may be achieved without significant impact on pulses processed. Further support for the use of the soliton in fibre all-optical switching is thus given. The stability of this pulse under perturbation is a factor which may give the soliton a primary role as a data carrier in future ultrafast switching systems.

In addition to investigating means of enhancement of the amplitude response of the device, the principle of concatenation is also applied to effect quantisation of the spectral responsivity of the NOLM. Since it is a broadband reflector with a spectral response dominated by the weak wavelength dependence of the coupling ratio, its basic form is limited in WDM processing environments where strong wavelength selectivity is a primary requirement. By modifying the basic configuration to include an in-fibre Bragg reflector, a device which is highly wavelength selective, the response of the NOLM becomes tightly quantised in wavelength.

By asymmetric placement of a Bragg reflector inside the fibre loop, two switching mechanisms are accessed. Firstly, using the differential SPM caused by a partially reflecting Bragg grating, wavelength-specific, soliton-regime self-switching is achieved, in which operation is restricted to input wavelengths which lie inside the reflection band of the grating. By increasing the reflectivity of the grating to $\sim$100%, the consequent restriction of signals within the grating reflection band to one arm of the device is used to effect control-pulse switching of a low power signal. In this case, switching is confined only to control pulses at wavelengths which lie inside the grating reflection band. Thus, by combining the merits of each of these devices, a configuration is produced which has the low switching power of the fibre NOLM and the high wavelength discrimination of the fibre Bragg reflector.

Having addressed some basic issues in fibre NOLM concatenation, the work is then turned to NOLM-based device configurations with more well-defined functional requirements. Chapter 4 introduces a novel all-fibre dual-wavelength laser in which the dual-wavelength NOLM is used an amplitude modulator for simultaneous active mode-locking of two cavities with chirped grating end-mirrors.

The use of chirped gratings in combination with a dual-cavity configuration enables tight and arbitrary wavelength specification across the whole erbium

gain band, a primary requirement of WDM systems. As the dominant source of dispersion within its cavity, chirped gratings are shown to be a convenient discrete component for accurate control of intracavity dispersion facilitating tailoring of output pulses characteristics. In addition, by simply altering the cavity length using intracavity fibre stretchers, each pulse train may be independently dispersion-tuned across the reflection band of its grating. The configuration is shown to generate stable, synchronised trains of picosecond pulses at 1540nm and 1557nm with an ultra-low inter-pulse-stream timing jitter enabling application to in switching environments at data rates in excess of 130GBit/s.

An additional feature of this configuration is its potential for self-stabilisation under environmental changes in cavity length, but due to the strong wavelength dependence of the dispersion characteristics of the gratings used in this first demonstration, evidence of this characteristic is not seen. However, by inclusion of gratings with apodised reflection profiles, these imperfections will be removed.

Chapter 5 presents results from two, further, NOLM-based configurations which perform the functions of memory and phase-locking. The primary value of each configuration is that, as workable but more demanding architectures, they serve to highlight the most significant limitations of the dual-wavelength NOLM in its fibre form.

The proposed memory architecture is based on a sequential design of two NOLM's configured with feedback. Its advantages over previous ring- and switch-based memories lie, firstly, in the fact that arbitrary, bit-level logical manipulation may be performed on stored data, and, secondly, that a stored word may remain unaltered on consecutive round trips. The failure of the configuration to operate in a stable manner is an outcome, not of the configuration itself, but of the long fibre lengths required to compensate for the relatively low nonlinear coefficient of fibre. The impact of fluctuations in fibre birefringence and length due to thermal drift and air-currents on the nonlinear characteristics of each device have been shown to contribute to corruption of stored data. In addition, the occurrence of Raman-induced pulse break-up is also thought to negatively influence stable operation of the configuration.

Although environmental disturbances are also a factor in degradation of the strength of phase-locking in the PLL configuration, the central difficulty arises from switch latency. Although the 100m NOLM used is shown to enable high

quality phase-locking to as high as the fourteenth harmonic of the baseband repetition rate, the trade-off between the requirements of low latency for stability, and maximum error-signal power for wide dynamic range, will ultimately place limits on the usefulness of phase-locking in this form.

Thus, the primary disadvantage of the fibre NOLM becomes apparent. As a tool for investigation, its simplicity and ease of construction make it a powerful medium with which to investigate the feasibility of a novel idea. In practice, however, for more demanding applications which are highly latency-critical, and require a high degree of ruggedness, the fibre NOLM is not the answer. From chapter 5 it is clear that the future exploitation of this device may well lie with the semiconductor laser amplifier implementation; the so-called TOAD or SLALOM. Its advantages over the all-fibre NOLM of concentrated nonlinearity in an integrable semiconductor device, enabling reduction of the waveguide component of the configuration to a minimum, makes this configuration potentially much more robust.

6.2 Future Directions

Since this study began, the research community has largely settled on the niche into which it considers the NOLM to be a best-fit; as already mentioned, in its dual-wavelength form, it is now routinely used in all-optical demultiplexing of ultra-high-speed data streams. Although a small number of papers have been published recently which introduce alternative applications of this device, relatively few groups have explored additional avenues of interest. To an extent, however, this would seem to be a premature and unfortunate pigeon-holing of a device which holds far greater potential. This section sets out to discuss the general findings of this thesis with this in mind.

What can be gleaned from this settled view of the NOLM is that the dual-wavelength form of the device is the one which is its most important manifestation. For data manipulation, the amplitude filtering property of the self-switched NOLM may have restricted practical application, indeed, as the emphasis in transmission systems research moves towards the use of dispersion-management rather than in-line filtering, its importance in this area may also be diminishing. The most important aspect of this work is not necessarily what it says about the

NOLM but what it says about the soliton. It is clear that even after transmission through 10km of fibre with phase perturbations from couplers, and without amplification, the soliton remains largely intact serving to pinpoint the great potential of this data format in the future. Further avenues of investigation for this data carrier will be discussed shortly.

For different reasons, similar comment might be made regarding fibre lasers. In the lab environment, where output can be continuously monitored, instability may be dealt with easily. In "the real world", the drift in mode-locking quality due to the seeming myriad of destabilising contributions would be unacceptable. Thus, as simple sources of high quality solitons, they are excellent tools, but as elements in future networks, they may well prove to be too prone to environmental instability to be of much value. It is clear that semiconductor sources perform just as well in transmission experiments with pulse-stream jitter levels as low as a few hundred femtoseconds. Coupled with environmental stability, these factors would seem to make them a far superior alternative.

Probably the most interesting aspect of this earlier work is the advantages which are shown to accrue from the integration of the fibre Bragg grating into the basic NOLM configuration. With the increased importance of WDM it would be beneficial to investigate the degree to which the wavelength response of the NOLM may be further confined. In this way, its evident usefulness may be further exploited in time-wavelength multiplexed systems.

The work with the greatest potential for further development, however, is that coming out of the memory and PLL configurations. As the thrust of the great percentage of work in all-optical processing is packet oriented, spurred on by the growth of interest in ATM, both of these configurations are extremely interesting and potentially important. Neither configuration is limited by its inherent design, but by the use of the all-fibre NOLM. Thus, further work could be carried out aimed at implementing each using SLA based NOLM's (TOAD's). The "fly-wheel" action and potential stability of a SLA-based PLL combined with the ultrafast switching of the TOAD, with its flexibility and increased robustness, may also provide a basis for an alternative form of all-optical regenerator. In combination with a transmission experiment the jitter suppression and retiming of a such a configuration could be put to the test in a realistic environment. An incidental advantage of such an experiment would be its potential for further

establishing the robustness of the soliton as referred to above. By integrating a regenerator or working memory into a recirculating loop transmission experiment, functions typical of a network node could be simulated and the effect on retransmitted data evaluated.

In conclusion, among recent developments in all-optical switching, the NOLM is a device with a great deal of potential and the development of the TOAD as a direct extension of principle opens up further, and potentially exciting, application areas. The NOLM may have much more to contribute as the field of photonic processing matures to its inevitable reality.

References

[1] T.F. La Porta, M. Veerarghavan, E. Ayanoglu, and R.D. Gitlin. B-ISDN: a technology discontinuity. *IEEE Communications Magazine*, (pp.84-97), October 1994.

[2] S.D. Personick. Towards global information networking. *Proceedings of the IEEE*, 81:pp.1549–1557, 1993.

[3] T. Miki. The potential of photonic networks. *IEEE Communications Magazine*, pages 23–27, December 1994.

[4] D.M. Spirit, A.D. Ellis, and P.E. Barnsley. Optical time division multiplexing: systems and networks. *IEEE Communications Magazine*, (pp.56-62), December 1994.

[5] A.D. Ellis, D.M. Patrick, D. Flannery, R.J. Manning, D.A.O. Davies, and D.M. Spirit. Ultra-high-speed OTDM networks using semiconductor amplifier-based processing nodes. *IEEE J. Lightwave Technol.*, 13:pp.761–770, 1995.

[6] M.J. O'Mahony, D. Simeonidou, A. Yu, and J. Zhou. The design of a European optical network. *IEEE J. Lightwave Technol.*, 13:pp.817–828, 1995.

[7] H.A. Haus. Molding light into solitons. *IEEE Spectrum Magazine*, pages pp.48–53, March 1993.

[8] L.F. Mollenauer. Soliton transmission speeds greatly multiplied by sliding-frequency guiding filters. *Optics and Photonics News*, pages pp.15–19, April 1994.

[9] M. Nakazawa, K. Suzuki, E. Yamada, H. Kubota, and Y. Kimura. Straight-line soliton data transmissions over 200km at 20Gbit/s and 100km at 40Gbit/s using erbium-doped fibre amplifiers. *Electron. Lett.*, 29:1474–1476, 1993.

[10] H. Taga, M. Suzuki, N. Edagawa, H. Tanaka, Y. Yoshida, S. Yamamoto, S. Akiba, and H. Wakabayashi. Multi-thousand kilometer optical soliton data transmission experiments at 5Gb/s using an electroabsorption modulator pulse generator. *IEEE J. Lightwave Technol.*, 12:pp.231–235, 1994.

[11] T. Widdowson, D.J. Malyon, X. Shan, and P.J. Watkinson. Soliton propagation without transmission control using a phase-locked erbium fibre ring laser. *Electron. Lett.*, 30:pp.661–663, 1994.

[12] L.F. Mollenauer, P.V. Mamyshev, and M.J. Neubelt. Measurement of timing jitter in filter-guided soliton transmission at 10Gbits/s and achievement of 375Gbits/s-Mm, error free, at 12.5 and 15Gbits/s. *Opt. Lett.*, 19:pp.704–706, 1994.

[13] K. Iwatsuki, K. Suzuki, S. Nishi, and M. Saruwatari. 80Gb/s optical soliton transmission over 80km with time/polarisation division multiplexing. *IEEE Photon. Technol. Lett.*, 5:pp.245–247, 1993.

[14] M. Nakazawa amd K. Suzuki, E. Yoshida, E. Yamada, T. Kitoh, and M. Kawachi. 160Gbit/s soliton data transmission over 200km. *Electron. Lett.*, 31:pp.565–566, 1995.

[15] F.M. Knox, W. Forysiak, and N.J. Doran. 10 Gbit/s soliton communication systems over standard fibre at 1.55 μm and the use of dispersion compensation. *IEEE J. Lightwave Technol.*, 13:pp.1955–1963, 1995.

[16] K.J. Blow, N.J. Doran, and S.J.D. Phoenix. The soliton phase. *Opt. Commun.*, 88:pp.137–140, 1992.

[17] N.J. Doran and D. Wood. Soliton processing element for all-optical switching and logic. *J. Opt. Soc. of Am., B*, 4:pp.1843–1846, 1987.

[18] M.N. Islam. *Ultrafast Fiber Switching Devices and Systems.* Cambridge Studies in Modern Optics, 12. Cambridge University Press, Cambridge, 1992.

[19] N.J. Doran and D. Wood. Nonlinear-optical loop mirror. *Opt. Lett.*, 13:pp.56–58, 1988.

[20] D.M. Patrick, A.D. Ellis, and D.M. Spirit. Bit-rate flexible all-optical demultiplexing using a nonlinear optical loop mirror. *Electron. Lett.*, 29:pp.702–703, 1993.

[21] S. Bigo and E. Desurvire. 20GHz all-optical clock recovery based on fibre laser mode-locking with fibre nonlinear loop mirror as variable intensity/phase modulator. *Electron. Lett.*, 31:pp.1855–1857, 1995.

[22] K.L. Hall, K.A. Rauschenbach, E.A. Swanson, S.R. Chinn, and G. Raybon. Picosecond-accuracy all-optical bit phase sensing using a nonlinear optical loop mirror. *IEEE Photon. Technol. Lett.*, 7:pp.935–937, 1995.

[23] K.A. Rauschenbach, K.L. Hall, J.C. Livas, and G. Raybon. All-optical pulse width and wavelength conversion at 10GBit/s using a nonlinear optical loop mirror. *IEEE Photon. Technol. Lett.*, 6:pp.1130–1132, 1994.

[24] G. Keiser. *Optical Fiber Communications.* Electrical and Electronic Engineering Series. McGraw-Hill, Singapore, 1991.

[25] B.J. Ainslie and C.R. Day. A review of single-mode fibers with modified dispersion characteristics. *IEEE J. Lightwave Technol.*, 4:pp.967–979, 1986.

[26] K.S. Kim, R.H. Stolen, W.A. Reed, and K.W. Quoi. Measurement of the nonlinear index of silica-core and dispersion-shifted fibres. *Opt. Lett.*, 19:pp.257–259, 1994.

[27] N.J. Doran and K.J. Blow. Solitons in optical communications. *IEEE J. Quantum Electron.*, 19:pp.1883–1888, 1983.

[28] K.J. Blow and N.J. Doran. *Solitons in Optical Fibres.* Nonlinear Waves in Solid State Physics. Plenum Press , New York, 1990.

[29] G.P. Agrawal. *Nonlinear Fiber Optics.* Quantum Electronics – Principles and Applications. Academic Press, San Diego, 1989.

[30] J.P. Gordon. Theory of soliton self-frequency shift. *Opt. Lett.*, 11:pp.662–664, 1986.

[31] K.J. Blow and D. Wood. Theoretical description of transient stimulated Raman scattering in optical fibres. *IEEE J. Quantum Electron.*, 25:pp.2665–2673, 1989.

[32] F.M. Mitschke and L.F. Mollenauer. Discovery of the soliton self-frequency shift. *Opt. Lett.*, 11:pp.659–661, 1986.

[33] W. Hodel and H.P. Weber. Decay of femtosecond higher-order solitons in an optical fiber induced by raman self-pumping. *Opt. Lett.*, 12:pp.924–926, 1987.

[34] K. Tai, A. Hasegawa, and N. Bekki. Fission of optical solitons induced by stimulated Raman effect. *Opt. Lett.*, 13:392–394, 1988.

[35] G.I. Stegeman and R.H. Stolen. Waveguides and fibers for nonlinear optics. *J. Opt. Soc. of Am., B*, 6:pp.652–662, 1989.

[36] G.I. Stegeman. *Overview of nonlinear integrated optics*, volume 247 of *Series B: Physics*. NATO ASI series, 1990.

[37] C.N. Ironside. Ultra-fast all-optical switching. *Contemporary Physics*, 34:pp.1–18, 1993.

[38] S.M. Jensen. The nonlinear coherent coupler. *IEEE J. Quantum Electron.*, 18:pp.1580–1583, 1982.

[39] S.R. Friberg, A.M. Weiner, Y. Silberberg, B.G. Sfez, and P.S. Smith. Femtosecond switching in a dual-core-fiber nonlinear coupler. *Opt. Lett.*, 13:pp.904–906, 1988.

[40] S. Trillo, S. Wabnitz, E.M. Wright, and G.I. Stegeman. Soliton switching in fiber nonlinear directional couplers. *Opt. Lett.*, 13:pp.672–674, 1988.

[41] M.N. Islam, E.R. Sunderman, R.H. Stolen, W. Pleibel, and J.R. Simpson. Soliton switching in a fiber nonlinear loop mirror. *Opt. Lett.*, 14:pp.811–813, 1989.

[42] M.N. Islam. Ultrafast all-optical logic gates based on soliton trapping in fibers. *Opt. Lett.*, 14:pp.1257–1259, 1989.

[43] M.N. Islam. All-optical cascadable NOR gate with gain. *Opt. Lett.*, 15:pp.417–419, 1990.

[44] M.N. Islam, C.E. Soccolich, and D.A.B. Miller. Low-energy ultrafast fiber soliton logic gates. *Opt. Lett.*, 15:pp.909–911, 1990.

[45] C.E. Soccolich, M.W. Chbat, M.N. Islam, and P.R. Prucnal. Cascade of ultrafast soliton-dragging and trapping logic gates. *IEEE Photon. Technol. Lett.*, 4:pp.1043–1046, 1992.

[46] M.W. Chbat, B. Hong, M.N. Islam, C.E. Soccolich, and P.R. Prucnal. Ultrafast soliton-trapping AND gate. *IEEE J. Lightwave Technol.*, 10:pp.2011–2016, 1992.

[47] K.C. Byron. Kerr modulation of signals at 1.3μm and 1.5μm in polarisation-maintaining fibres pumped at 1.06μm. *Electron. Lett.*, 23:pp.1324–1326, 1987.

[48] T. Morioka, H. Takara, K. Mori, and M. Saruwatari. Ultrafast reflective optical Kerr demultiplexer using polarisation rotation mirror. *Electron. Lett.*, 28:pp.521–522, 1992.

[49] D.M. Patrick and A.D. Ellis. Demultiplexing using crossphase modulation-induced spectral shifts and Kerr polarisation rotation in optical fibres. *Electron. Lett.*, 29:pp.227–229, 1993.

[50] A.D. Ellis, W.A. Pender, T. Widdowson, D.J. Richardson, R.P. Chamberlain, and L. Dong. All-optical modulation of 40GHz beat frequency conversion soliton source. *Electron. Lett.*, 31:pp.1362–1364, 1995.

[51] H. Kawaguchi. Proposal for a new all-optical waveguide functional device. *Opt. Lett.*, 10:pp.411–413, 1985.

[52] I.H. White and R.V. Penty. Demonstration of the optical Kerr effect in an all-fibre Mach-Zehnder interferometer at laser diode powers. *Electron. Lett.*, 24:pp.340–341, 1988.

[53] K.I. Kang, I. Glesk, T.G. Chang, P.R. Prucnal, and R.K. Boncek. Demonstration of all-optical Mach-Zehnder demultiplexer. *Electron. Lett.*, 31:pp.749–750, 1995.

[54] K.J. Blow, N.J. Doran, and B.K. Nayar. Experimental demonstration of optical soliton switching in an all-fiber nonlinear Sagnac interferometer. *Opt. Lett.*, 14:pp.754–756, 1989.

[55] D.A. Pattison, W. Forysiak, P.N. Kean, I. Bennion, and N.J. Doran. Soliton switching using cascaded nonlinear-optical loop mirrors. *Opt. Lett.*, 20:pp.19–21, 1995.

[56] K. Ohkuma, Y.H. Ichikawa, and Y. Abe. Soliton propagation along optical fibres. *Opt. Lett.*, 12:pp.516–518, 1987.

[57] L.F. Mollenauer, R.H. Stolen, and J.P. Gordon. Experimental observation of picosecond pulse narrowing and solitons in optical fibres. *Phys. Rev. Lett.*, 45:pp.1095–1098, 1980.

[58] L.F. Mollenauer, R.H. Stolen, J.P. Gordon, and W.J. Tomlinson. Extreme picosecond pulse narrowing by means of soliton effect in single-mode optical fibres. *Opt. Lett.*, 8:pp.289–291, 1983.

[59] D.B. Mortimore. Fibre loop reflectors. *IEEE J. Lightwave Technol.*, 6:pp.1217–1224, 1988.

[60] K. Otsuka. Nonlinear antiresonsant ring interferometer. *Opt. Lett.*, 8, 471-473 1983.

[61] I.N. Duling III, C.J.Chen, P.K.A. Wai, and C.R. Menyuk. Operation of a nonlinear loop mirror in a laser cavity. *IEEE J. Quantum Electron.*, 30:pp.194–199, 1994.

[62] K.Smith, N.J. Doran, and P.G.J. Wigley. Pulse shaping, compression, and pedestal suppression employing a nonlinear-optical loop mirror. *Opt. Lett.*, 15:pp.1294–1296, 1990.

[63] B.K. Nayar, K.J. Blow, and N.J. Doran. All-optical switching in nonlinear fibre loop mirror devices. *Opt. Comp. and Proc*, 1:pp.81–89, 1991.

[64] M. Matsumoto, H. Ikeda, and A. Hasegawa. Suppression of noise accumulation in bandwidth-limited soliton transmission by means of nonlinear loop mirrors. *Opt. Lett.*, 19:pp.183–183, 1994.

[65] N.J. Smith and N.J. Doran. Picosecond soliton propagation using nonlinear optical loop mirrors as intensity filters. *Electron. Lett.*, 30:pp.1084–1085, 1994.

[66] M.J. Holmes, D.L. Williams, and R.J. Manning. Highly nonlinear optical fiber for all optical processing applications. *IEEE Photon. Technol. Lett.*, 7:pp.1045–1047, 1995.

[67] C. Desem and P.L. Chu. Effect of chirping on solution propagation in single-mode fibers. *Opt. Lett.*, 11:pp.248–250, 1986.

[68] M. Jinno and T. Matsumoto. Ultrafast all-optical logic operations in a nonlinear Sagnac interferometer with two control beams. *Opt. Lett.*, 16:pp.220–222, 1991.

[69] J.K. Lucek and K. Smith. All-optical signal regenerator. *Opt. Lett.*, 18:pp.1226–1228, 1993.

[70] J.K. Lucek and K. Smith. Remotely programmable routing device with optical clock division. *IEEE Photon. Technol. Lett.*, 7:pp.59–61, 1995.

[71] N.A. Whitaker Jr., M.C. Gabriel, H. Avramopoulos, and A. Huang. All-optical, all-fiber circulating shift register with an inverter. *Opt. Lett.*, 16:pp.1999–2001, 1991.

[72] B.K. Nayar, N. Finlayson, and N.J. Doran. Concatenated all-optical loop mirror switches. *J. Modern Opt.*, 40:pp.2327–2332, 1993.

[73] N.S. Bergano, C.R. Davidson, A.M. Vengsarkar, B.M. Nyman, S.G. Evangelides, J.M. Darcie, M. Ma, J.D. Evanlow, P.C. Corbett, M.A. Mills, G.A. Ferguson, J.R. Pedrazzani, J.A. Nagel, J.L. Zyskind, J.W. Sulhoff, and A.J. Lucero. 100Gb/s WDM transmission of twenty 5Gb/s NRZ data channels over trans-oceanic distances using gain flattened amplifier chain. *ECOC'95 Postdeadline Session*, paper Th.A.3.1:pp.967–970, 1995.

[74] H.A. Haus and Y. Lai. Narrow-band optical channel dropping filter. *IEEE J. Lightwave Technol.*, 10:pp.57–61, 1992.

[75] I. Bennion, J.A.R. Williams, L. Zhang, K. Sugden, and N.J. Doran. UV-written in-fibre Bragg gratings. *Opt. Quantum Electron.*, To be published, Feb. 1996.

[76] K.O. Hill. Fiber Bragg components in filtering and dispersion compensation applications. *OSA Topical Meeting on Photosensitivity and Quadratic Nonlinearity in Glass Waveguides, Technical Digest*, pages pp.6–8, 1995.

[77] G. Meltz, W.W. Morey, and W.H. Glenn. Formation of Bragg gratings in optical fibers by a transverse holographic method. *Opt. Lett.*, 14:pp.823–825, 1989.

[78] M.C. Farries, K. Sugden, D.C.J. Reid, I. Bennion, A. Molony, and M.J. Goodwin. Very broad reflection bandwidth (44nm) chirped fibre gratings and narrow bandpass filters by the use on an amplitude mask. *Electron. Lett.*, 30:pp.891–892, 1994.

[79] K. Sugden, L. Zhang, J.A.R. Williams, and I. Bennion. Dissimilar wavefront technique for linear and quadratic chirps. *OSA Topical Meeting on Photosensitivity and Quadratic Nonlinearity in Glass Waveguides, Technical Digest*, pages pp.136–139, 1995.

[80] K.O. Hill, B. Malo, F. Bilodeau, D.C. Johnson, and J. Albert. Bragg gratings fabricated in monomode photosensitive optical fiber by UV exposure through a phase mask. *Appl. Phys. Lett*, 62:pp.1035–1037, 1993.

[81] L.F. Mollenauer, J.P. Gordon, and S.G. Evangelides. The sliding-frequency guiding filter: an improved form of soliton jitter control. *Opt. Lett.*, 17:pp.1575–1577, 1992.

[82] L.F. Mollenauer, E. Lichtman, M.J. Neubelt, and G.T. Harvey. Demonstration, using sliding-frequency guiding filters of error-free soliton transmission over more that 20Mm at 10Gbit/s single channel, and over more than 13Mm at 20 Gbit/s in a two-channel WDM. *Electron. Lett.*, 29:pp.910–911, 1993.

[83] E. Kollveit, B. Biotteau, F. Pitel, I. Riant, O. Audouin, P. Brindel, E. Burn, P. Sansonetti, and J.P. Hamaide. Soliton frequency-guiding in a 2x5Gb/s WDM system using a UV-written fibre Fabry-Perot filter. *Proc. ECOC'95*, pages pp.43–46, 1995.

[84] D.C. Johnson, K.O. Hill, F. Bilodeau, and S. Faucher. New design concept for a narrowband wavelength-selective optical tap and combiner. *Electron. Lett.*, 23:pp.668–669, 1987.

[85] T.J. Cullen, H.N. Rourke, C.P. Chew, S.R. Baker, T. Bricheno, K.C. Byron, and A. Fielding. Compact all-fibre wavelength drop and add filter. *Electron. Lett.*, 30:pp.2160–2162, 1994.

[86] F. Bilodeau, D.C. Johnson, S. Thériault, B. Malo, and K.O. Hill. An all-fiber dense-wavelength-division multiplexer/demultiplexer using photoimprinted Bragg gratings. *IEEE Photon. Technol. Lett.*, 7:pp.88–90, 1995.

[87] F. Bilodeau, K.O. Hill, B. Malo, D.C. Johnson, and J. Albert. High-return-loss narrowband all-fiber bandpass Bragg transmission filter. *IEEE Photon. Technol. Lett.*, 6:pp.80–83, 194.

[88] M.J. Guy, S.V. Chernikov, J.R. Taylor, and R. Kashyap. Low-loss fibre Bragg grating transmission filter based on a fibre polarisation splitter. *Electron. Lett.*, 30:pp.1512–1513, 1994.

[89] J.A.R. Williams, I. Bennion, K. Sugden, and N.J. Doran. Fibre dispersion compensation using a chirped in-fibre Bragg grating. *Electron. Lett.*, 30:pp.985–987, 1994.

[90] R. Kashyap, S.V. Chernikov, P.F. McKee, and J.R. Taylor. 30ps chromatic dispersion compensation of 400fs pulses at 100Gbit/s in optical fibres using an all fibre photoinduced chirped reflection grating. *Electron. Lett.*, 30:pp.1078–1080, 1994.

[91] P.A. Krug, T. Stephens, G. Yoffe, F. Ouelette, P. Hill, and G. Dhosi. Dispersion compensation over 270km at 10Gbit/s using an offset-core chirped fibre Bragg grating. *Electron. Lett.*, 31:pp.1091–1093, 1995.

[92] K.A. Ahmed, B.J. Eggleton, H. Liu, P.A. Krug, and F. Ouelette. Simultaneous mode selection and pulse compression of gain-switched pulses from a Fabry-Perot laser using a 40-mm chirped optical fiber grating. *IEEE Photon. Technol. Lett.*, 7:pp.158–160, 1995.

[93] J.A.R. Williams, I. Bennion, and L. Zhang. The compression of optical pulses using self-phase-modulation and linearly chirped Bragg-gratings in fibers. *IEEE Photon. Technol. Lett.*, 7:pp.491–493, 1995.

[94] M.E. Fermann, F. Haberl, M. Hofer, and H. Hochreiter. Non-linear amplifying loop mirror. *Opt. Lett.*, 15:pp.752–754, 1990.

[95] D.J. Richardson, R.I. Laming, and D.N. Payne. Very low threshold Sagnac switch incorporating an erbium doped fibre amplifier. *Electron. Lett.*, 26:pp.1779–1781, 1990.

[96] A.W. O'Neill and R.P. Webb. All-optical loop mirror switch employing an asymmetric amplifier/attenuator combination. *Electron. Lett.*, 26:pp.2008–2009, 1990.

[97] K.J. Blow, N.J. Doran, B.K. Nayar, and B.P. Nelson. Two-wavelength operation of the nonlinear fiber loop mirror. *Opt. Lett.*, 15:pp.248–250, 1990.

[98] H. Avramopoulos, P.M.W. French, M.C. Gabriel, H.H. Houh , N.A. Whitaker Jr., and T. Morse. Complete switching in a three-terminal Sagnac switch. *IEEE Photon. Technol. Lett.*, 3:pp.235–237, 1991.

[99] K.J. Blow, N.J. Doran, and B.P. Nelson. Demonstration of the nonlinear fibre loop mirror as an ultrafast all-optical demultiplexer. *Electron. Lett.*, 26:pp.962–965, 1990.

[100] M. Jinno and T. Matsumoto. Nonlinear Sagnac interferometer switch and its applications. *IEEE J. Quantum Electron.*, 28:pp.875–882, 1992.

[101] K.J. Blow and K. Smith. Nonlinear loop mirror devices and applications. *BT Technol. J.*, 11:pp.99–107, 1993.

[102] K. Suzuki, K. Iwatsuki, S. Nishi, and M. Saruwatari. 160Gbit/s single polarisation subpicosecond transform limited pulse signal demultiplexing using ultrafast optical loop mirror including MQW travelling wave semiconductor laser amplifier. *Electron. Lett.*, 30:pp.660–661, 1994.

[103] K. Uchiyama, S. Kawanishi, H. Takara, T. Morioka, and M. Saruwatari. 100Gbit/s to 6.3Gbit/s demultiplexing experiment using polarisation-independent nonlinear optical loop mirror. *Electron. Lett.*, 30:pp.873–875, 1994.

[104] S. Kawanishi, H. Takara, T. Morioka, O. Kamatani, and M. Saruwatari. 200Gbit/s, 100km time-division-multiplexed optical transmission using supercontinuum pulses with prescaled PLL timing extraction and all-optical demultiplexing. *Electron. Lett.*, 31:pp.816–817, 1995.

[105] N. Finlayson, B.K. Nayar, and N.J. Doran. Switch inversion and polarization sensitivity of the nonlinear-optical loop mirror. *Opt. Lett.*, 17:pp.112–114, 1992.

[106] G.I. Stegeman, R. Zanoni, N. Finlayson, E.M. Wright, and C.T. Seaton. Review of third order nonlinear integrated optics. *IEEE J. Lightwave Technol.*, 6:pp.953–970, 1988.

[107] S. Larochelle, Y. Hibino, V. Mizrahi, and G.I. Stegeman. All-optical switching of grating transmission using cross-phase modulation in optical fibres. *Electron. Lett.*, 26:pp.1459–1460, 1990.

[108] J.A.R. Williams. *Personal Communication*, 1995.

[109] M. Jinno. Effects of group velocity dispersion on self/cross phase modulation in a nonlinear Sagnac interferometer switch. *IEEE J. Lightwave Technol.*, 10:pp.1167–1178, 1992.

[110] D.J. Blumenthal, R.J. Feuerstein, and J.R. Sauer. First demonstration of multihop all-optical packet switching. *IEEE Photon. Technol. Lett.*, 6:pp.457–460, 1994.

[111] H. Tsushima, M. Shabeer, P. Barnsley, and D. Pitcher. Demonstration of an optical packet add/drop with wavelength-coded header. *IEEE Photon. Technol. Lett.*, 7:pp.212–214, 1995.

[112] D. Cotter, J.K. Lucek, M. Shabeer, K. Smith, D.C. Rogers, D. Nesset, and P. Gunning. Self-routing of 100Gbit/s packets using 6 bit keyword address recognition. *Electron. Lett.*, 31:pp.1475–1476, 1995.

[113] M Nakazawa, E. Yoshida, E. Yamada, K. Suzuki, T. Kitoh, and M Kawachi. 80Gbit/s soliton data transmission over 500km with unequal amplitude solitons for timing clock extraction. *Electron. Lett.*, 30:pp.1777–1778, 1994.

[114] J.K. Lucek and K. Smith. All-optical clock multiplication and division using an optically mode-locked laser. *Proc. ECOC'95*, pages pp.941–944, 1995.

[115] D.J. Richardson. Fibre-based short pulse generation and shaping technology. *Proc. ECOC'95*, pages pp.147–149, 1995.

[116] I.N. Duling. All-fiber ring soliton laser mode locked with a nonlinear mirror. *Opt. Lett.*, 16:pp.539–541, 1991.

[117] D.J. Richardson, R.I. Laming, D.N. Payne, M.W. Phillips, and V.J. Matsas. 320fs soliton generation with passively mode-locked erbium fibre laser. *Electron. Lett.*, 27:pp.730–732, 1991.

[118] D.J. Richardson, R.I. Laming, D.N. Payne, V. Matsas, and M.W. Phillips. Selfstarting, passively modelocked erbium fibre ring laser based on the amplifying Sagnac switch. *Electron. Lett.*, 27:pp.542–544, 1991.

[119] E. Yoshida, Y. Kimura, and M. Nakazawa. Laser diode-pumped femtosecond erbium fiber laser with a sub-ring cavity for repetition rate control. *Appl. Phys. Lett*, 60:pp.932–934, 1992.

[120] K. Smith, E.J. Greer, R. Wyatt, P. Wheatley, and N.J. Doran. Totally integrated erbium fibre soliton laser pumped by laser diode. *Electron. Lett.*, 27:pp.244–246, 1991.

[121] M. Nakazawa, E. Yoshida, and Y. Kimura. Ultrastable harmonically and regeneratively modelocked polarisation-maintaining erbium fibre ring laser. *Electron. Lett.*, 30:pp.1603–1605, 1994.

[122] X. Shan, D. Cleland, and A. Ellis. Stabilising Er fibre soliton laser with pulse phase locking. *Electron. Lett.*, 28:pp.182–183, 1992.

[123] E.J. Greer and K. Smith. All-optical FM mode-locking of fibre laser. *Electron. Lett.*, pages pp.1741–1743, 1992.

[124] E.J. Greer, Y. Kimura, K. Suzuki, E. Yoshida, and M. Nakazawa. Generation of 1.2ps, 10GHz pulse train from all-optically modelocked , erbium fibre ring laser with active nonlinear polarisation rotation. *Electron. Lett.*, 30:pp.1764–1765, 1994.

[125] R.P. Davey, R.P.E. Fleming, K. Smith, R. Kashyap, and J.R. Armitage. Mode-locked erbium fibre laser with wavelength selection by means of fibre Bragg grating reflector. *Electron. Lett.*, 27:pp.2087–2088, 1991.

[126] B.P. Nelson, K. Smith, and K.J. Blow. Mode-locked erbium fibre laser using all-optical nonlinear loop mirror modulator. *Electron. Lett.*, 28:pp.656–658, 1992.

[127] D.A. Pattison, P.N. Kean, W. Forysiak, I. Bennion, and N.J. Doran. Band-pass switching in a nonlinear-optical loop mirror. *Opt. Lett.*, 20:pp.362–364, 1995.

[128] M. Jinno. Effect of timing jitter on an optically controlled picosecond optical switch. *Opt. Lett.*, 18:pp409–1411, 1993.

[129] M. Jinno. Effects of crosstalk and timing jitter on all-optical time-division demultiplexing using a nonlinear fiber Sagnac interferometer switch. *IEEE J. Quantum Electron.*, 30:pp.2842–2853, 1994.

[130] J.B. Schlager, S. Kawanishi, and M. Saruwatari. Dual wavelength pulse generation using mode-locked erbium-doped fibre ring laser. *Electron. Lett.*, 27:pp.2072–2073, 1991.

[131] H. Takara, S. Kawanishi, M. Saruwatari, and J.B. Schlager. Multi-wavelength birefringent-cavity mode-locked fibre laser. *Electron. Lett.*, 28:pp.2274–2275, 1992.

[132] D.U. Noske, M.J. Guy, K. Rottwitt, R. Kashyap, and J.R. Taylor. Dual-wavelength operation of a passively mode-locked figure-of-eight ytterbium-erbium fibre soliton laser. *Opt. Commun.*, 108:pp.297–301, 1994.

[133] P.N. Kean, J.W.D. Gray, I. Bennion, and N.J. Doran. Dispersion-modified actively modelocked erbium fibre laser using a chirped fibre grating. *Electron. Lett.*, 30:pp.2133–2135, 1994.

[134] V. Mizrahi and J.E. Sipe. Optical properties of photosensitive fiber phase gratings. *IEEE J. Lightwave Technol.*, 11:pp.1513–1517, 1993.

[135] S.J. Hewlett, J.D. Love, G. Meltz, T.J. Bailey, and W.W. Morey. Cladding-mode coupling characteristics of Bragg gratings in depressed-cladding fibre. *Electron. Lett.*, 31:pp.821–822, 1995.

[136] E. Desurvire. *Erbium-Doped Fibre Amplifiers - Principles and Applications.* Wiley-Interscience, New York, 1994.

[137] I.N. Duling, M.L. Dennis, and T.F. Carruthers. A high power 18GHz actively modelocked Er/Yb laser. *Proc. ECOC'94*, pages pp.357–360, 1994.

[138] A.B. Grudinin, D.J. Richardson, and D.N. Payne. Energy quantisation in figure eight fibre laser. *Electron. Lett.*, 28:pp.67–68, 1992.

[139] M.L. Dennis and I.N. Duling. Role of dispersion in limiting pulse width in fiber lasers. *Appl. Phys. Lett*, 62:pp.2911–2913, 1993.

[140] N.J. Smith, K.J. Blow, and I. Andonovic. Sideband generation through perturbations to the average soliton model. *IEEE J. Lightwave Technol.*, 10:pp.1329–1333, 1992.

[141] S.M.J. Kelly. Characteristic sideband instability of periodically amplified average soliton. *Electron. Lett.*, 28:pp.806–807, 1992.

[142] D.U. Noske, N. Pandit, and J.R. Taylor. Source of spectral and temporal instability in soliton fiber lasers. *Opt. Lett.*, 17:pp.1515–1517, 1992.

[143] M.L. Dennis and I.N. Duling. Intracavity dispersion measurement in modelocked fibre laser. *Electron. Lett.*, 29:pp.409–411, 1993.

[144] K.O. Hill. Aperiodic distributed-parameter waveguides for integrated optics. *Appl. Opt*, 13:pp.1853–1856, 1974.

[145] K.O. Hill, F. Bilodeau, B. Malo, T. Kitigawa, S. Thériault, D.C. Johnson, and J. Albert. Chirped fibre Bragg gratings for compensation of optical-fiber dispersion. *Opt. Lett.*, 19:pp.1314–1316, 1994.

[146] K.O. Hill, S. Thériault, B. Malo, F. Bilodeau, T. Kitigawa, D.C. Johnson, J. Albert, K. Takiguchi, T. Kataoka, and K. Hagimoto. Chirped in-fibre Bragg grating dispersion compensators: linearisation of dispersion characteristic and demonstration of dispersion compensation in 1000km, 10Gbit/s optical fibre link. *Electron. Lett.*, 30:pp.1755–1756, 1994.

[147] M.L. Dennis and I.N. Duling. Experimental study of sideband formation in femtosecond fiber lasers. *IEEE J. Quantum Electron.*, 30:pp.1469–1477, 1994.

[148] D. Henderson and A.G. Roddie. A comparison of spectral and temporal techniques for the measurement of timing jitter and their application in a modelocked argon ion and dye laser system. *Opt. Commun.*, 100:pp.456–460, 1993.

[149] D. von der Linde. Characterization of the noise in continuously mode-locked lasers. *Appl. Phys. B*, 39:pp.201–217, 1986.

[150] A. Finch, X. Zhu, P.N. Kean, and W. Sibbett. Noise characterization of mode-locked color-centre laser sources. *IEEE J. Quantum Electron.*, 26:pp.1115–1123, 1990.

[151] M.J.W. Rodwell, K.J. Weingarten, and D.M. Bloom. Reduction of timing fluctuations in a mode-locked Nd:YAG laser by electronic feedback. *Opt. Lett.*, 11:pp.638–640, 1986.

[152] M.J. Rodwell, D.M. Bloom, and K.J. Weingarten. Subpicosecond laser timing stabilization. *IEEE J. Quantum Electron.*, 25:pp.817–827, 1989.

[153] I.G. Fuss. An interpretation of the spectral measurement of optical pulse train noise. *IEEE J. Quantum Electron.*, 30:pp.2707–2710, 1994.

[154] R.P. Davey, K. Smith, and A. McGuire. High-speed, mode-locked, tunable, integrated erbium fibre laser. *Electron. Lett.*, 28:pp.482–484, 1992.

[155] D.R. Hjelme and A.R. Mickelson. Theory of timing jitter in actively mode-locked lasers. *IEEE J. Quantum Electron.*, 28:pp.1594–1605, 1993.

[156] M. Jinno. Correlated and uncorrelated timing jitter in gain-switched laser diodes. *IEEE Photon. Technol. Lett.*, 5:pp.1140–1143, 1993.

[157] S.V. Chernikov, J.R. Taylor, and R. Kashyap. Comblike dispersion-profiled fiber for soliton pulse train generation. *Opt. Lett.*, 19:pp.539–541, 1994.

[158] E.A. Swanson and S.R. Chinn. 23-GHz and 123-GHz soliton pulse generation using two CW lasers and standard single-mode fibre. *IEEE Photon. Technol. Lett.*, 6:pp.796–798, 1994.

[159] A.V. Shipulin, E.M. Dianov, D.J. Richardson, and D.N. Payne. 40GHz soliton train generation through multisoliton pulse propagation in a dispersion varying optical fiber circuit. *IEEE Photon. Technol. Lett.*, 6:pp.1380–1382, 1994.

[160] E.A. Swanson, S.R. Chinn, K. Hall, K.A. Rauschenbach, R.S. Bondurant, and J. W. Miller. 100-GHz soliton pulse train generation using soliton compression of two phase side bands from a single DFB laser. *IEEE Photon. Technol. Lett.*, 6:pp.1194–11–6, 1994.

[161] E.A. Swanson and S.R. Chinn. 40GHz pulse train generation using soliton compression of a Mach-Zehnder modulator output. *IEEE Photon. Technol. Lett.*, 7:114–116, 1995.

[162] D.J. Richardson, R.P. Chamberlain, L. Dong, D.N. Payne, A.D. Ellis, T. Widdowson, and D.M. Spirit. Demonstration of 205km transmission of 35GHz, 5ps pulses generated from a diode-driven, low-jitter, beat-signal to soliton train conversion source. *Electron. Lett.*, 31:pp.470–472, 1995.

[163] D.A. Pattison, P.N. Kean, J.W.D. Gray, I. Bennion, and N.J. Doran. Actively modelocked dual-wavelength fibre laser with ultra-low inter-pulse-stream timing jitter. *IEEE Photon. Technol. Lett.*, To be Published, December 1995.

[164] S. Gray, A.B. Grudinin, and D.N. Payne. Femtosecond harmonically mode-locked fiber laser with time jitter below 1ps. *Opt. Lett.*, 20:pp.189–191, 1995.

[165] K.K. Goel, P.R. Prucnal, Y. Shimazu, M. Milbrodt, E. Desurvire, and B. Tell. Demonstration of packet switching through an integrated-optic tree switch using photo-conductive logic gates. *Electron. Lett.*, 26:pp.287–289, 1990.

[166] M. Nakazawa, H. Kubota, E. Yamada, and K. Suzuki. Infinite-distance soliton transmission with soliton controls in time and frequency domains. *Electron. Lett.*, 28:pp.1099–1100, 1992.

[167] W. Pieper, M. Eiselt, G. Peiper, R. Langenhorst, A. Ehrhardt, and H.G. Weber. Investigation of crosstalk interference in a fibre loop optical buffer. *Electron. Lett.*, 30:pp.435–436, 1994.

[168] K.L. Hall, J.D. Moores, K.A. Rauschenbach, W.S. Wong, E.P. Ippen, and H.A. Haus. All-optical storage of a 1.25kb packet at 10Gb/s. *IEEE Photon. Technol. Lett.*, 7:pp.1093–1095, 1995.

[169] J.D. Moores, K.L. Hall, S.M. LePage, K.A. Rauschenbach, W.S. Wong, H.A. Haus, and E.P. Ippen. 20-GHz optical storage loop/laser using amplitude modulation, filtering and artificial fast saturable absorption. *IEEE Photon. Technol. Lett.*, 7:pp.1096–1098, 1995.

[170] H. Avramopoulos and N.A. Whitaker Jr. Addressable fiber-loop memory. *Opt. Lett.*, 18:pp.22–24, 1993.

[171] D.A. Pattison, P.N. Kean, J.W.D. Gray, I. Bennion, and N.J. Doran. Actively modelocked dual-wavelength fibre laser with ultra-low inter-pulse-stream timing jitter. *IEEE Photon. Technol. Lett.*, 12(7), 1995.

[172] J.P. Sokoloff, P.R. Prucnal, I. Glesk, and M. Kane. A terahertz optical asymmetric demultiplexer (TOAD). *IEEE Photon. Technol. Lett.*, 5:pp.787–790, 1993.

[173] A.D. Ellis and D.M Spirit. Compact 40Gbit/s optical demultiplexer using a GaInAsP optical amplifier. *Electron. Lett.*, 29:pp.2115–2116, 1993.

[174] I. Glesk, J.P. Sokoloff, and P.R. Prucnal. Demonstration of all-optical demultiplexing of TDM data at 250 GBit/s. *Electron. Lett.*, 30:pp.339–341, 1994.

[175] M. Eiselt, W. Peiper, and H.G. Weber. SLALOM: Semiconductor Laser Amplifier in a Loop Mirror. *IEEE J. Lightwave Technol.*, 13:pp.2099–2111, 1995.

[176] B.P. Nelson and N.J. Doran. Optical sampling oscilloscope using nonlinear fibre loop mirror. *Electron. Lett.*, 27:pp.204–205, 1991.

[177] S. Kawanishi, H. Takara, K. Uchiyama, T. Kitoh, and M. Saruwatari. 100Gbit/s, 50km, and nonrepeatered optical transmission employing all-optical multi/demultiplexing and PLL timing extraction. *Electron. Lett.*, 29:pp.1075–1077, 1993.

[178] A.D. Ellis, T. Widdowson, X. Shan, G.E. Wickens, and D.M. Spirit. Transmission of a true single polarisation 40Gbit/s soliton data signal over 205km using a stabilised erbium fibre ring laser and 40GHz electronic timing recovery. *Electron. Lett.*, 29:pp.990–992, 1993.

[179] H. Bulow. Optoelectronic synchronisation scheme for ultrahigh-speed optical demultiplexer. *Electron. Lett.*, 31:pp.1937–1938, 1995.

Appendix A

Publications

[1] D. A. Pattison, W. Forysiak, P. N. Kean, I. Bennion and N. J. Doran. Soliton switching using cascaded nonlinear-optical loop mirrors. *Opt. Lett.*, 20(1):19–21, 1995.

[2] D. A. Pattison, P. N. Kean, W. Forysiak, I. Bennion and N. J. Doran. Bandpass switching in a nonlinear-optical Loop mirror. *Opt. Lett.*, 20(4):362–364, 1995.

[3] D. A. Pattison, P. N. Kean, J. W. D. Gray, I. Bennion and N. J. Doran. Actively modelocked dual-wavelength fibre laser with ultra-low inter-pulse-stream timing jitter *IEEE Photon. Technol. Lett.*, To Be Published, December 1995.

[4] P. N. Kean, D. A. Pattison, W. Forysiak, I. Bennion and N. J. Doran. Bandpass switching based on a nonlinear optical loop mirror and an in-fibre grating reflector. *CLEO Europe Technical Digest*, paper CFG1:pg 403, 1994.

[5] D. A. Pattison, W. Forysiak, P. N. Kean, I. Bennion and N. J. Doran. Soliton switching using cascaded nonlinear optical loop mirrors. *CLEO Europe Technical Digest*, paper CFG3:404–405, 1994.

[6] D. A. Pattison, P. N. Kean, J. W. D. Gray, I. Bennion and N. J. Doran. Actively mode-locked dual-wavelength fibre laser using chirped in-fibre Bragg gratings and its application to all-optical memory. *Technical Digest, OSA Topical Meeting on Photosensitivity and Quadratic Nonlinearity in Glass Waveguides*, paper SuB13:140–143, 1995.

[7] D. A. Pattison, P. N. Kean, J. W. D. Gray, I. Bennion and N. J. Doran. Dual-wavelength mode-locked erbium fibre laser with low inter-pulse-stream timing jitter. *Proc. ECOC'95*, paper Mo.L.4.2:139–142, 1995.

[8] D. A. Pattison, P. N. Kean, J. W. D. Gray, I. Bennion and N. J. Doran. Actively mode-locked dual-wavelength laser with low inter-pulse-stream timing jitter, using chirped in-fibre gratings. *IOP half-day meeting on In-Fibre Bragg Gratings and Special Fibres*, May 1995.

[9] D. A. Pattison, P. N. Kean, W. Forysiak, I. Bennion and N. J. Doran. Bandpass switching based on a nonlinear optical loop mirror and an in-fibre grating reflector. *IOP half-day meeting on In-Fibre Bragg Gratings and Special Fibres*, May 1994.